

Technical report No. 538/2021

**MIGRATION OF CARBON AND
IODINE IN A CEMENTITIOUS
MATRIX**

FINAL REPORT

Authors:

Petr Večerník
Lukáš Brázda
Marta Hybášková
Vlastislav Kašpar
Kateřina Kolomá
Anna Pecková

ÚJV Řež, a. s.

Praha, March 2021

Project name:

Research of the Migration of Carbon and Iodine in a Cementitious Matrix

Report name:

Migration of Carbon and Iodine in a Cementitious Matrix – Final Report

Final report*Registration number of the client: SO2019-029**Registration number of the supplier: 19SMP086***Authors:****Petr Večerník,****Lukáš Brázda, Marta Hybášková, Vlastislav Kašpar, Kateřina Kolomá, Anna Pecková****Investigating institutions:****ÚJV Řež, a. s.**

Approved by				
Function	Institution	Name	Date	Signature
Person responsible for the technical solution - supplier	ÚJV Řež, a. s.	Petr Večerník		
Person responsible for the coordination of the project - supplier	ÚJV Řež, a. s.	Václava Havlová		
Person responsible for the technical solution - client	SÚRAO	Eva Popelová		
Person responsible for the coordination of the project – client	SÚRAO	Eva Popelová		





SÚRAO

 SÚRAO	Migration of Carbon and Iodine in Cementitious Matrix – Interim Report	Registration number:
		538/2021

Table of contents

1	Introduction	16
2	Time schedule	19
3	Material for the experiments	20
3.1	Site description.....	20
3.2	Collection of the material.....	21
3.3	Preparation of the samples for the experiments	22
3.3.1	Disc samples for the diffusion experiments and the measurement of porosity	22
3.3.2	Crushed samples for the sorption and leaching tests and XRD analysis	23
3.3.3	Cylinders for the determination of permeability.....	23
3.4	Experimental solution	23
4	Experiments and methods	24
4.1	Porosity.....	24
4.1.1	Saturation and gravimetric method.....	24
4.1.2	Hg porosimetry.....	25
4.2	Permeability	25
4.3	XRD analysis.....	26
4.4	TGA analysis.....	26
4.5	Predictive geochemical modelling	27
4.5.1	Modelling of the interaction of the cementitious material with water.....	27
4.5.2	Modelling of the chemical speciation of the tracers	27
4.6	Aerobic and anaerobic conditions.....	27
4.6.1	Aerobic conditions.....	27
4.6.2	Anaerobic conditions	28
4.7	Leaching and interaction experiments	28
4.7.1	Leaching experiments	28
4.7.2	Interaction experiments	30
4.8	Sorption experiments	31
4.8.1	Experimental procedure	31
4.8.2	Experimental solutions with the ¹⁴ C and ¹²⁵ I tracers.....	32
4.8.3	Evaluation of the sorption experiments.....	33
4.9	Diffusion experiments.....	33

 SÚRAO	Migration of Carbon and Iodine in Cementitious Matrix – Interim Report	Registration number:
		538/2021

4.9.1	Experimental solutions with the ³ H, ¹⁴ C and ¹²⁵ I tracers	34
4.9.2	Evaluation of the through diffusion experiments	35
5	Results	36
5.1	Porosity of the source material	36
5.2	Permeability of the source material	36
5.3	XRD analysis of the source material.....	37
5.4	Predictive geochemical modelling results	39
5.4.1	Models of the interaction of the CIM cement material with water	39
5.4.2	Models of the chemical speciation of the tracers	39
5.5	Leaching and interaction experiments - chemical analysis	42
5.5.1	Leaching experiments – chemical analysis of the liquid phases	42
5.5.1.1	Leaching of the powdered materials.....	42
5.5.1.2	Leaching of the coupons into deionised water	45
5.5.1.3	Leaching of the coupons into a saturated Ca(OH) ₂ solution	48
5.5.2	Column interaction experiments – chemical analysis of the liquid phases	51
5.6	Sorption experiment results.....	55
5.6.1	¹²⁵ I tracer sorption	55
5.6.2	¹⁴ C tracer sorption	56
5.7	Diffusion experiment results	62
5.8	Analysis of the solid phases following the leaching/interaction experiments	65
5.8.1	Solid phases following leaching.....	66
5.8.1.1	XRD and TGA of the crushed materials	66
5.8.1.2	XRD and TGA of the coupons	69
5.8.2	Solid phases following column interaction	74
6	Data comparison	78
7	Conclusions	79
8	References.....	81
	Appendix	82

List of Figures:

Fig. 1: Setup of the circulation system in the CIM experimental borehole (GTS webpage, 2021)	18
Fig. 2: Location of the CIM / HPF experiment at the Grimsel Test Site (Kontar et al. 2019) ..	20
Fig. 3: Schematic 3D view of the HPF and planned CIM borehole relative to the AU-126 shear zone and AU tunnel at the GTS (GTS webpage, 2021)	21
Fig. 4: The as-delivered CIM_2 core.....	21
Fig. 5: Core cutting scheme – samples for the hydraulic permeability (blue), diffusion (green) and sorption (brown) experiments and the XRD analysis (yellow)	22
Fig. 6: Apparatus for the determination of the filtration coefficient K_f at the ÚJV laboratory...26	
Fig. 7: Anaerobic glovebox with an inert argon atmosphere	28
Fig. 8: Coupon samples prepared for the leaching experiments under different experimental conditions	29
Fig. 9: Small column with the crushed cementitious material	30
Fig. 10: Experimental setup of the column interaction experiments	31
Fig. 11: Diffusion experiment performed in an inert atmosphere in the anaerobic glovebox..34	
Fig. 12: XRD pattern of the CIM_2_1 sample	38
Fig. 13: XRD quantitative phase analysis of the CIM materials.....	38
Fig. 14: Diagram of the iodine speciation for iodide tracer concentrations of 10^{-4} and 10^{-6} mol/l; without the suppression of the theoretical solid phases	40
Fig. 15: Diagram of the iodine speciation for iodide tracer concentrations of 10^{-4} and 10^{-6} mol/l; with the suppression of the theoretical solid phases	40
Fig. 16: Diagram of the organic carbon speciation for acetate tracer concentrations of 10^{-4} and 10^{-6} mol/l	41
Fig. 17: Diagram of the organic carbon speciation for formate tracer concentrations of 10^{-4} and 10^{-6} mol/l	41
Fig. 18: Evolution of the Na^+ , K^+ , Mg^{2+} , Sr^{2+} and $\text{Al}_{(\text{tot})}$ concentrations during the leaching of the CIM_1_1 powdered material into deionised water	43
Fig. 19: Evolution of the Ca^{2+} , Cl^- , SO_4^{2-} , SiO_3^{2-} and CO_3^{2-} concentrations during the leaching of the CIM_1_1 powdered material into deionised water	43
Fig. 20: Evolution of the Na^+ , K^+ , Mg^{2+} , Sr^{2+} and $\text{Al}_{(\text{tot})}$ concentrations during the leaching of the CIM_2_1 powdered material into deionised water	44
Fig. 21: Evolution of the Ca^{2+} , Cl^- , SO_4^{2-} , SiO_3^{2-} and CO_3^{2-} concentrations during the leaching of the CIM_2_1 powdered material into deionised water	44
Fig. 22: Evolution of the Na^+ , K^+ , Mg^{2+} , Sr^{2+} and $\text{Al}_{(\text{tot})}$ concentrations during the leaching of the CIM_2_6 powdered material into deionised water	45

 SÚRAO	Migration of Carbon and Iodine in Cementitious Matrix – Interim Report	Registration number:
		538/2021

Fig. 23: Evolution of the Ca^{2+} , Cl^- , SO_4^{2-} , SiO_3^{2-} and CO_3^{2-} concentrations during the leaching of the CIM_2_6 powdered material into deionised water	45
Fig. 24: Evolution of the liquid phase composition during the leaching of the CIM_1_1 coupons into deionised water under anaerobic conditions in the glovebox	46
Fig. 25: Evolution of the liquid phase composition during the leaching of the CIM_2_1 coupons into deionised water under anaerobic conditions in the glovebox	46
Fig. 26: Evolution of the liquid phase composition during the leaching of the CIM_2_6 coupons into deionised water under anaerobic conditions in the glovebox	47
Fig. 27: Evolution of the liquid phase composition during the leaching of the CIM_1_1 coupons into deionised water under aerobic laboratory conditions	47
Fig. 28: Evolution of the liquid phase composition during the leaching of the CIM_2_1 coupons into deionised water under aerobic laboratory conditions	47
Fig. 29: Evolution of the liquid phase composition during the leaching of the CIM_2_6 coupons into deionised water under aerobic laboratory conditions	48
Fig. 30: Evolution of the Mg^{2+} , Sr^{2+} , aluminium and SiO_3^{2-} concentrations during the leaching of the CIM_1_1 coupon into the saturated $\text{Ca}(\text{OH})_2$ solution	48
Fig. 31: Evolution of the Ca^{2+} and CO_3^{2-} concentrations during the leaching of the CIM_1_1 coupon into the saturated $\text{Ca}(\text{OH})_2$ solution	49
Fig. 32: Evolution of the Mg^{2+} , Sr^{2+} , aluminium and SiO_3^{2-} concentrations during the leaching of the CIM_2_1 coupon into the saturated $\text{Ca}(\text{OH})_2$ solution	49
Fig. 33: Evolution of the Ca^{2+} and CO_3^{2-} concentrations during the leaching of the CIM_2_1 coupon into the saturated $\text{Ca}(\text{OH})_2$ solution	50
Fig. 34: Chemical composition (Sr^{2+} , Ca^{2+} , aluminium concentrations) of the output aqueous phase from column K14A	51
Fig. 35: Chemical composition (SO_4^{2-} , CO_3^{2-} and SiO_3^{2-} concentrations) of the output aqueous phase from column K14A	52
Fig. 36: Chemical composition (Sr^{2+} , Ca^{2+} , aluminium concentrations) of the output aqueous phase from column K14B	52
Fig. 37: Chemical composition (SO_4^{2-} , CO_3^{2-} and SiO_3^{2-} concentrations) of the output aqueous phase from column K14B	53
Fig. 38: Chemical composition (Sr^{2+} , Ca^{2+} , aluminium concentrations) of the output aqueous phase from column K24A	53
Fig. 39: Chemical composition (SO_4^{2-} , CO_3^{2-} and SiO_3^{2-} concentrations) of the output aqueous phase from column K24A	54
Fig. 40: Chemical composition (Sr^{2+} , Ca^{2+} , aluminium concentrations) of the output aqueous phase from column K24B	54
Fig. 41: Chemical composition (SO_4^{2-} , CO_3^{2-} and SiO_3^{2-} concentrations) of the output aqueous phase from column K24B	55
Fig. 42: R_d distribution coefficients for ^{125}I	56

 SÚRAO	Migration of Carbon and Iodine in Cementitious Matrix – Interim Report	Registration number:
		538/2021

Fig. 43: R_d distribution coefficients for ^{14}C acetate	57
Fig. 44: Comparison of the effect of the sample particle size (^{14}C formate tracer, aerobic conditions, 56 days of experimentation)	57
Fig. 45: Comparison of the influence of the tracer selection (conditions: fraction 0.25–1.00 mm, anaerobic, after 56 days of the experiment).....	58
Fig. 46: Comparison of the effect of aerobic/anaerobic conditions (conditions: $\text{H}^{14}\text{COONa}$ tracer, fraction 0.25–1.00 mm (CIM) or 0.5–1.0 mm (CEM I), after 7 days of experimentation)	59
Fig. 47: Dependence of the R_d on time (conditions: $\text{H}^{14}\text{COONa}$ tracer, aerobic conditions, fraction 0.25–1.00 mm, after 56 days of experimentation)	60
Fig. 48: Dependence of the R_d on time (conditions: $\text{H}^{14}\text{COONa}$ tracer, anaerobic conditions, fraction 0.25–1.00 mm, after 56 days of experimentation)	60
Fig. 49: Dependence of the R_d on time (conditions: $\text{CH}_3^{14}\text{COONa}$ tracer, anaerobic conditions, fraction 0.25–1.00 mm, after 56 days of experimentation)	61
Fig. 50: Example of the breakthrough curves of the HTO, acetate and iodide tracers (CIM_2_1 material, aerobic conditions).....	63
Fig. 51: Comparison of the $t_{n=0}$ parameter for the HTO, acetate and iodide tracers and materials	63
<i>Fig. 52: Effective diffusion coefficient values of the studied tracers under aerobic conditions</i>	<i>64</i>
Fig. 53: Comparison of the effective diffusion coefficient values of the ^{14}C -formate tracer under aerobic and anaerobic conditions	65
Fig. 54: TGA analysis of the BC12A1 material.....	67
Fig. 55: XRD pattern of the BC12A1 material	67
Fig. 56: Comparison of the dominant crystalline phases (initial and leached materials) for the leaching experiments with the crushed materials.....	68
Fig. 57: TGA analysis of the 265B material.....	70
Fig. 58: XRD pattern of the 265B material	71
Fig. 59: Comparison of the dominant crystalline phases for the coupon leaching experiments; initial and leached CIM_1_1 materials	71
Fig. 60: Comparison of the dominant crystalline phases for the coupon leaching experiments; initial and leached CIM_2_1 materials	72
Fig. 61: Comparison of the dominant crystalline phases for the coupon leaching experiments; initial and leached CIM_2_6 materials	72
Fig. 62: TGA analysis of the CIM24B-A material.....	75
Fig. 63: XRD pattern of the CIM24B-A material	75
Fig. 64: Comparison of the dominant crystalline phases for the column interaction experiments; initial and leached CIM_1_1 materials	76

Fig. 65: Comparison of the dominant crystalline phases for the column interaction experiments; initial and leached CIM_2_6 materials	76
Fig. 66: XRD pattern of the CIM_1_1 material	83
Fig. 67: TGA analysis of the CIM_1_1 material	84
Fig. 68: XRD pattern of the CIM_2_1 material	85
Fig. 69: TGA analysis of the CIM_2_1 material	86
Fig. 70: XRD pattern of the CIM_2_6 material	87
Fig. 71: TGA analysis of the CIM_2_6 material	88
Fig. 72: TGA analysis of the BC12A1 material.....	89
Fig. 73: XRD pattern of the BC12A1 material	90
Fig. 74: TGA analysis of the BC12AN1 material	91
Fig. 75: XRD pattern of the BC12AN1 material.....	92
Fig. 76: TGA analysis of the BC22A2 material.....	93
Fig. 77: XRD pattern of the BC22A2 material	94
Fig. 78: TGA analysis of the BC22AN2 material	95
Fig. 79: XRD pattern of the BC22AN2 material.....	96
Fig. 80: TGA analysis of the 113B material.....	97
Fig. 81: XRD pattern of the 113B material	98
Fig. 82: TGA analysis of the 113L material	99
Fig. 83: XRD pattern of the 113L material.....	100
Fig. 84: TGA analysis of the 115C material	101
Fig. 85: XRD pattern of the 115C material.....	102
Fig. 86: TGA analysis of the 211C material	103
Fig. 87: XRD pattern of the 211C material.....	104
Fig. 88: TGA analysis of the 219B material.....	105
Fig. 89: XRD pattern of the 219B material	106
Fig. 90: TGA analysis of the 219L material.....	107
Fig. 91: XRD pattern of the 219L material.....	108
Fig. 92: TGA analysis of the 265B material.....	109
Fig. 93: XRD pattern of the 265B material	110
Fig. 94: TGA analysis of the 265L material	111
Fig. 95: XRD pattern of the 265L material.....	112
Fig. 96: TGA analysis of the 14A-A material.....	113

 SÚRAO	Migration of Carbon and Iodine in Cementitious Matrix – Interim Report	Registration number:
		538/2021

Fig. 97: XRD pattern of the 14A-A material.....	114
Fig. 98: TGA analysis of the 14A-C material.....	115
Fig. 99: XRD pattern of the 14A-C material	116
Fig. 100: TGA analysis of the 14B-A material	117
Fig. 101: XRD pattern of the 14B-A material.....	118
Fig. 102: TGA analysis of the 14B-C material.....	119
Fig. 103: XRD pattern of the 14B-C material	120
Fig. 104: TGA analysis of the 24A-A material	121
Fig. 105: XRD pattern of the 24A-A material.....	122
Fig. 106: TGA analysis of the 24A-C material.....	123
Fig. 107: XRD pattern of the 24A-C material	124
Fig. 108: TGA analysis of the 24B-A material.....	125
Fig. 109: XRD pattern of the 24A-A material.....	126
Fig. 110: TGA analysis of the 24B-C material.....	127
Fig. 111: XRD pattern of the 24B-C material	128

 SÚRAO	Migration of Carbon and Iodine in Cementitious Matrix – Interim Report	Registration number:
		538/2021

List of Tables:

Tab. 1: Tracers foreseen for the circulation in the CIM in-situ experiment (GTS webpage, 2021)	17
Tab. 2: Time schedule of the planned laboratory work	19
Tab. 3: Composition of the input Grimsel groundwater used in the predictive modelling.....	27
Tab. 4: Porosity values of the source material	36
Tab. 5: Permeability (filtration coefficient).....	37
Tab. 6: XRD quantitative phase analysis of the CIM materials.....	37
Tab. 7: Results of the predictive interactive modelling – composition of the equilibrated solutions	39
Tab. 8: R_d distribution coefficients for the ^{14}C tracers (aerobic and anaerobic conditions, mesh size fractions 0.25–1.00 mm (CIM) and 0.5–1.0 mm (CEM I))	61
Tab. 9: Sorption yields for the ^{14}C tracers (aerobic/anaerobic conditions, mesh size fractions 0.25–1.00 mm (CIM) and 0.5–1.0 mm (CEM I)).....	62
Tab. 10: Comparison of the effective diffusion coefficient values	64
Tab. 11: Dominant crystalline phase compositions of the leached crushed materials	68
Tab. 12: Comparison of the porosity values for the initial source and leached materials (coupon samples)	70
Tab. 13: Dominant crystalline phase compositions of the leached coupon materials	73
Tab. 14: Dominant crystalline phase compositions of the materials following the column interaction experiments	77
Tab. 15: Composition of the cement material from the deeper parts of the CIM drilled core	78
Tab. 16: Description of the analysed materials	82

List of abbreviations:

CIM	Carbon and Iodine Migration
DGR	Deep Geological Repository
DW	Distilled/Deionised Water
ECW	Evolved Cement (Pore)Water
GTS	Grimsel Test Site
HCP	Hardened Cement Paste
HPF	Hyperalkaline Plume in Fractured rock
HTO	Tritiated Water
LSC	Liquid scintillation counter/counting
LTD	Long Term Diffusion
NAGRA	Nationale Genossenschaft für Lagerung Radioaktiver Abfälle
NUMO	The Nuclear Waste Management Organization of Japan
PMMA	Polymethyl Methacrylate
RWM	Radioactive Waste Management Limited
SEM	Scanning Electron Microscope
SÚRAO	Správa úložišť radioaktivních odpadů (Czech Radioactive Waste Repository Authority)
TGA	Thermogravimetric analysis
ÚJV	ÚJV Řež, a. s.
XRD	X-Ray Diffraction
XRF	X-Ray Fluorescence

Diážděná 6 | 110 00 Praha 1 | ČR

tel.: +420 221 421 511 | fax: +420 221 421 544 | e-mail: info@suro.cz | www.suro.cz

IČ: 66000769 | Bankovní spojení: ČNB Praha 1, č. ú. 35-64726011/0710

Tato zpráva je výhradně majetkem SÚRAO a její šíření bez vědomí majitele je zakázáno.

Správa úložišť radioaktivních odpadů byla zřízena k 1. 6. 1997 Ministerstvem průmyslu a obchodu ČR jako státní organizace na základě atomového zákona (§ 26 zákona č. 18/1997 Sb. o mírovém využívání jaderné energie a ionizujícího záření). Od roku 2000 je SÚRAO ve smyslu § 51 zákona č. 219/2000 Sb. organizační složkou státu.

 SÚRAO	Migration of Carbon and Iodine in Cementitious Matrix – Final Report	Registration number:
		538/2021

Abstract

It is planned that cement and cementitious materials will be used in the future Czech deep geological repository for spent nuclear fuel and radioactive waste. Their role will vary widely, i.e. as the matrix for the fixing of radioactive waste, as a sealing material component, as a container construction material and as a repository construction material. When cementitious materials come into contact with water, a significant increase in the pH of the aqueous medium occurs due to the leaching of the cement. This may impact the properties of the bentonite engineered barrier, the transport properties (sorption, diffusion) of radionuclides released from the radioactive waste and the speciation of the released matter.

The CIM (Carbon and Iodine Migration) international project focuses primarily on the study of the migration and sorption of ^{14}C and ^{129}I through a cementitious material. Since these radionuclides represent two of the critical radionuclides that are present in high-level and low/intermediate-level waste, it was necessary to obtain the relevant migration and interaction data for the assessment calculations. The partners in the CIM project comprise NAGRA (Switzerland), NUMO (Japan), RWM (United Kingdom) and SÚRAO (Czech Republic).

The laboratory research performed by ÚJV Řež, a. s. in the first phase of the CIM project focused on the characterisation of the cementitious materials obtained from a drilled core (depth 0.5-1.5 m). The report provides information on the physical, chemical and transport properties of cementitious infill materials obtained via borehole experimentation at the Grimsel Test Site. It is planned that this borehole will be fitted with instrumentation for the conducting of an *in-situ* experiment on the transport of radionuclides through cement materials and the cement/rock interface.

The material subjected to study comprised a hardened cement paste (two 50 mm cores) taken from the upper part of the borehole. For experimental purposes the drilled cores were divided into smaller parts (discs for diffusion, cylinders for permeability, crushed/powdered material for sorption and mineralogical analysis). With respect to the performance assessment of the future Czech deep geological repository, both ^{14}C and ^{129}I are considered to be critical radionuclides. ^{14}C , as acetate and formate, and ^{125}I (this radionuclide was used for the purposes of experiments instead of ^{129}I), as iodide, tracers were used in the sorption and diffusion experiments; tritiated water (HTO) was also studied in the diffusion experiments as the reference non-sorbing tracer. The hardened cement paste samples were subjected to degradation/interaction processes once they came into contact with water. The degradation/interaction processes were applied in the batch and column configuration. During the degradation/interaction procedure, the liquid phases were characterised via chemical composition analysis and the solid phase materials were analysed via XDR, TGA and porosimetry following the conclusion of the experiment.

The results obtained indicate that the tested samples of hardened cement paste are relatively heterogenous in terms of many of the observed parameters, probably due to the sedimentation process that occurred during the filling of the borehole with the cement paste. For this reason, the material from the upper part of the borehole most probably exhibits different properties to the material present at a depth of 5 m at which the CIM experiment will be conducted.

Keywords

cement, carbon, acetate, formate, iodine, leaching, diffusion, sorption, infill, radioactive waste disposal

 SÚRAO	Migration of Carbon and Iodine in Cementitious Matrix – Final Report	Registration number:
		538/2021

Abstrakt

Cement a cementové materiály budou využívány v úložištích radioaktivních odpadů a vyhořelého jaderného paliva pro mnoho účelů: jako matrice pro fixaci určitých typů odpadů, jako materiál pro kontejnery, jako konstrukční materiály úložiště a jako komponenty těsnících zátek. Při kontaktu s vodou je z cementových materiálů uvolňován výluh s vysokým pH, což může významně ovlivnit vlastnosti a chování bentonitové bariéry (zejména chemismus, mineralogii, transportní vlastnosti – sorpce a difúzi, speciální kontaminantů).

Mezinárodní projekt CIM (Carbon and Iodine Migration) je zaměřen zejména na studium migrace a sorpce radionuklidů ^{14}C a ^{129}I přes cementový materiál. Tyto jsou členy skupiny kritických radionuklidů vyskytujících se ve vysoceaktivních i nízko a středněaktivních odpadech, proto je nutné získat údaje o migraci a interakci těchto radionuklidů pro výpočty hodnocení bezpečnosti úložišť. Partneři projektu CIM jsou NAGRA (Švýcarsko), NUMO (Japonsko), RWM (Velká Británie) a SÚRAO (Česká republika).

Laboratorní výzkum prováděný v ÚJV Řež, a. s. se v první fázi projektu CIM věnoval cementovému materiálu z vrtného jádra získaného z hloubky 0.5-1.5 m. Tato zpráva shrnuje zjištěné informace o fyzikálních, chemických a transportních vlastnostech cementového výplňového materiálu, který byl získán z vrtu v podzemní laboratoři Grimsel. Tento vrt bude v roce 2020 instrumentován a bude v něm probíhat *in-situ* migrační experiment zaměřený na transport radionuklidů přes cementový materiál a rozhraní cement/hostitelská hornina.

Studovaný materiál byla vytvrdlá cementová pasta ve formě vrtného jádra o průměru 50 mm. Studované vzorky byly ze třech hloubkových úrovní z části vrtu nad intervalem, ve kterém bude probíhat samotný *in-situ* experiment. Vrtné jádro bylo pro potřeby experimentů rozděleno na různé typy vzorků (disky – pro difúze, válečky – pro propustnost, drť/prášek – pro sorpce a mineralogické analýzy).

Radionuklidy ^{14}C a ^{129}I jsou kritickými radionuklidy pro bezpečnostní hodnocení hlubinného úložiště radioaktivních odpadů. Pro migrační testy byly použity radionuklidy ^{14}C ve formě octanu a mravenčanu a ^{125}I (z důvodů radiační ochrany použit místo ^{129}I) ve formě jodidu. Jako referenční nesorbující se radionuklid byl v difúzních experimentech použit ^3H ve formě HTO.

Cementový materiál byl také podroben degradaci/interakci při kontaktu s vodou. Pro studium těchto procesů bylo použito vsádkové a kolonové uspořádání experimentů. V průběhu degradace/interakce bylo v odebraných kapalných fázích analyzováno jejich chemické složení, po ukončení experimentů byly na pevných fázích provedeny stanovení porozity a složení pomocí XRD a TGA.

Z dosažených a vyhodnocených výsledků vyplývá, že testovaná vytvrdlá cementová pasta je v mnoha parametrech nehomogenní. Tato nehomogenita byla pravděpodobně způsobena sedimentací cementové směsi při zaplňování vrtu v podzemní laboratoři Grimsel. Vlastnosti cementového materiálu z hloubky cca 5 m, ve které bude probíhat *in-situ* test projektu CIM, budou, dle dosud zjištěných informací, s velmi vysokou pravděpodobností odlišné.

Klíčová slova

cement, uhlík, octan, mravenčan, jód, loužení, difúze, sorpce, výplň, radioaktivní odpady

1 Introduction

The CIM (Carbon and Iodine Migration) project underway at the Grimsel Test Site (GTS) focuses on the study of the *in-situ* migration and sorption of ^{14}C and ^{129}I through a cementitious material and the granitic host rock, including the transport mechanism at the interface between these two materials. Additional laboratory experiments were designed aimed at determining a better understanding of the chemical-physical, mechanical and structural properties, mineralogy and, primarily, radionuclide migration and transport through a cementitious material.

Radionuclides of carbon (^{14}C) and iodine (^{129}I) comprise the main radionuclides of interest in terms of this project since, when released from repositories for high-level and low/intermediate-level waste, these radionuclides typically contribute most to the dose rate over the long-term according to the results of the respective assessment calculations. This is primarily due to the combination of high solubility and low sorption properties of the chemical forms in which the two radionuclides are expected to occur.

In the case of ^{14}C , experimental work on the speciation of carbon during the corrosion of activated and non-activated steel under anoxic conditions similar to those of a disposal cell revealed the formation of oxygenated and reduced hydrocarbons, including carboxylic acids and CH_4 . Methane is not expected to react with cementitious materials or with the host rock. Uncertainties remain, however, concerning the retardation of carboxylic acids in clay and cementitious materials. In the case of formic acid, currently no retardation is expected in near-neutral environments; however, laboratory experiments have revealed evidence of the weak sorption of formic acid on cementitious material (GTS webpage, 2021).

The iodine ^{129}I radionuclide originates principally from reprocessed waste and is expected to occur mostly in the form of iodide. For the purposes of minimising the risk factor in the experimental work and enhancing overall radiation safety, the ^{125}I radionuclide is often used instead of ^{129}I .

Although it is planned that large amounts of cementitious material will be used in both high-level and low/intermediate-level waste repositories, a large number of uncertainties remain with respect both to the release and *in-situ* retardation of ^{129}I and ^{14}C species in cementitious materials, especially in naturally-aged cement materials.

The following aims (GTS webpage, 2021) of the CIM international project were determined according to the requirements of the current project partners (NUMO, RWM, SÚRAO and NAGRA):

- To simulate the transport of ^{14}C and ^{129}I through the aged cementitious backfill of a radioactive waste repository and into the saturated host rock.
- To provide confirmation of the effect of the cementitious material on the retardation of ^{14}C and ^{129}I .
- To further improve the understanding of the behaviour of ^{14}C and ^{129}I under real in-situ conditions.
- To develop a method for the extrapolation of the results obtained from extensive laboratory-based migration studies to the field/repository scale.

 SÚRAO	Migration of Carbon and Iodine in Cementitious Matrix – Final Report	Registration number:
		538/2021

The CIM project relies largely on experience acquired from previous projects that employed radionuclides at the GTS (LTD, CFM etc.) and will benefit from the lessons learned from these projects with respect to borehole and surface equipment and sampling. Four vertical or slightly inclined boreholes from the overcoring of the HPF experiment at the GTS were backfilled with OPC mortar in 2004. One of these boreholes is being used as a circulation borehole for the CIM experiment (Fig. 1). The borehole and the depth of the circulation interval were selected aimed at positioning the latter in a dense matrix area with no distinct water conducting features. The selection was based on geological logs available from the HPF project. A small diameter (\varnothing 56 mm) borehole was drilled in the centre of the mortar backfill in November 2019 and fitted with a multi-packer system for the circulation of the test cocktail. The cocktail will be based on cement water and be prepared with the tracers listed in Tab. 1. Three monitoring boreholes were also drilled at short distances (\sim 15 cm) from the source borehole. Based on the results of the monitoring of the experiment and discussions between the various partners, the *in-situ* experiment will be overcored so as to allow for the analysis of diffusion profiles in the mortar and/or in the rock (GTS webpage, 2021).

Tab. 1: Tracers foreseen for the circulation in the CIM *in-situ* experiment (GTS webpage, 2021)

Tracers	Species
^{14}C	Formate (HCOO^-)
^{129}I	Iodide (I^-)
^3H	HTO
^{36}Cl	Cl^-
^{134}Cs	Cs^+
^{133}Ba	Ba^{2+}

The *in-situ* experiment working programme comprises the following steps (GTS webpage, 2021):

- 1) Finalisation of the experimental design
- 2) Drilling of the required boreholes and installation of the initial condition monitoring system
- 3) Development and construction of the experimental equipment (packer system, surface equipment)
- 4) Emplacement of the circulation interval
- 5) Commencement of circulation and monitoring
- 6) Overcoring and post-mortem analysis

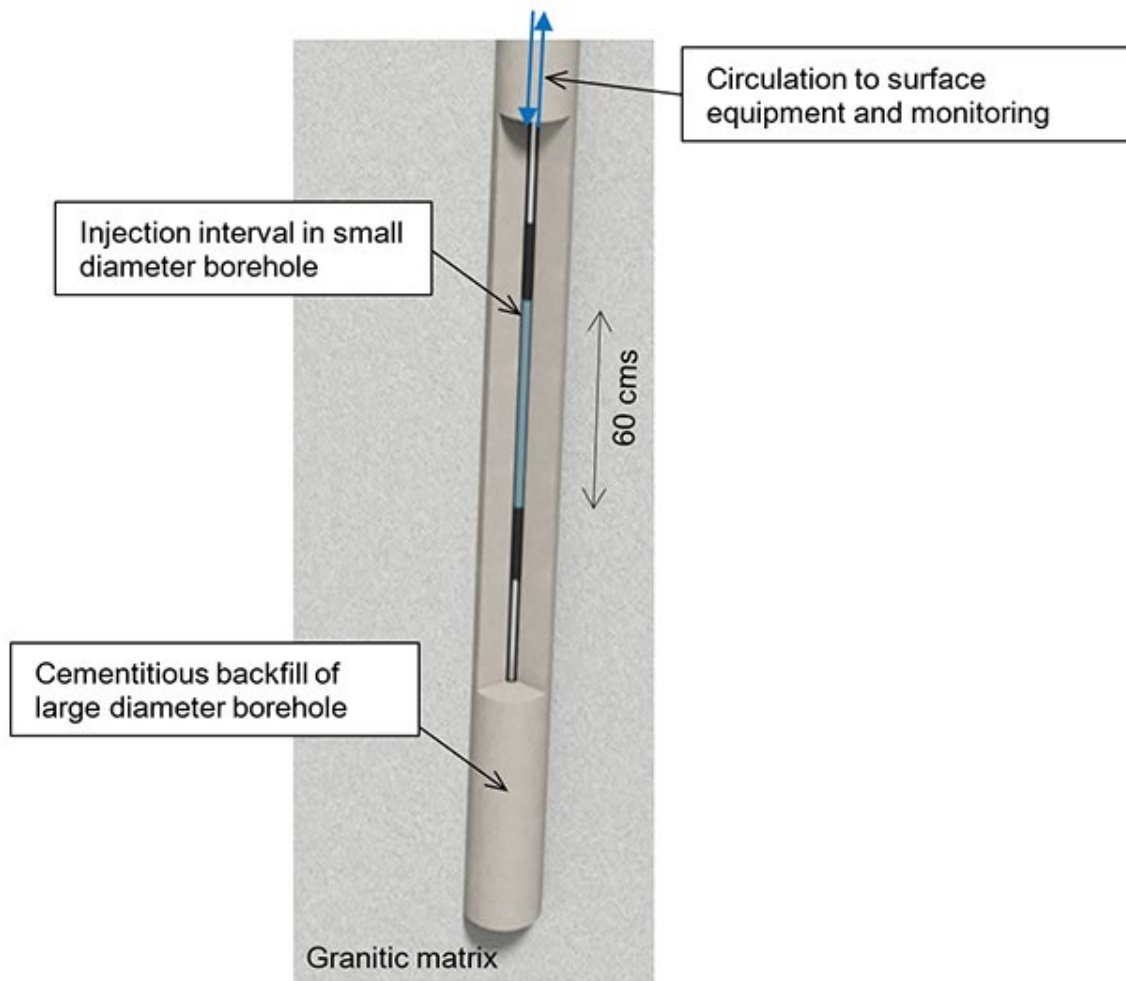


Fig. 1: Setup of the circulation system in the CIM experimental borehole (GTS webpage, 2021)

The CIM project concerns the study of a unique material, i.e. a cement-based mixture that has been exposed to long-term contact with the rock environment in an underground laboratory. The environment of the Grimsel laboratory has been well described and has been subjected to long-term monitoring.

The aim of the first phase of the CIM project was to characterise the cementitious materials of a borehole infill taken from three different depths from the interval 0.5-1.5 m. Samples were obtained via the initial drilling campaign. The parameters subjected to study included the sorption and diffusion of ^{125}I (iodide) and ^{14}C (acetate and formate) tracers, the chemical and physical properties of the cementitious material and the interaction with water and a $\text{Ca}(\text{OH})_2$ solution.

 SÚRAO	Migration of Carbon and Iodine in Cementitious Matrix – Final Report	Registration number:
		538/2021

2 Time schedule

The time schedule of the laboratory experiments is based on a contract concluded between SÚRAO and ÚJV in May 2019. Due to changes in the descriptions of the experimental phases and various deadlines, a supplement to the contract was agreed. The various planned experiments, accompanied by a short description of each experiment and the deadlines set, are summarised in Tab. 2.

Tab. 2: Time schedule of the planned laboratory work

Phase	Description	Deadline
1 – material	Collection of cementitious samples drilled by NAGRA at the GTS; preparation of different types of samples for the experiments	11/2019
2 – characterisation	Characterisation of the chemical and physical properties of the tested cementitious materials; definition of the experimental solutions	11/2019
3 – <i>in-situ</i> experiment	Cooperation on the planned <i>in-situ</i> migration experiment at the Grimsel Test Site underground laboratory	11/2019
4 – modelling	Predictive modelling of the interaction between the tested cementitious materials and the experimental solutions	11/2019
5 – leaching	Experiments on leaching and the interaction between the cementitious materials and the experimental solutions	11/2019
6 – sorption	Sorption batch experiments on crushed samples with ¹²⁵ I and organic ¹⁴ C tracers	11/2019
7 – diffusion	Through diffusion experiments on cylindrical samples with HTO, ¹²⁵ I and organic ¹⁴ C tracers	11/2019
Report 1	Interim Report	12/2019
8 – leaching II.	Continuation of the leaching/interaction experiments	01/2021
9 – sorption II.	Continuation of the sorption experiments	12/2020
10 – diffusion II.	Continuation of the diffusion experiments	12/2020
11 – analysis	Analysis of the cementitious material following the conclusion of the interaction experiments in order to monitor changes in the chemical and mineralogical composition	02/2021
12 – evaluation	Final evaluation of the experimental data and compilation of the final report	02/2021
Report 2	Final Report	03/2021

3 Material for the experiments

3.1 Site description

The *in-situ* part of the CIM experiment is located within the GTS radiation-controlled area at the site of the former Hyperalkaline Plume in Fractured Rock (HPF) experiment as illustrated in Fig. 2 and Fig. 3. An old borehole (HPF 98.005), that was backfilled with cement in 2004, was chosen for the experiment. A detailed description of the HPF experimental boreholes is provided in a report by Kontar et al. (2019).

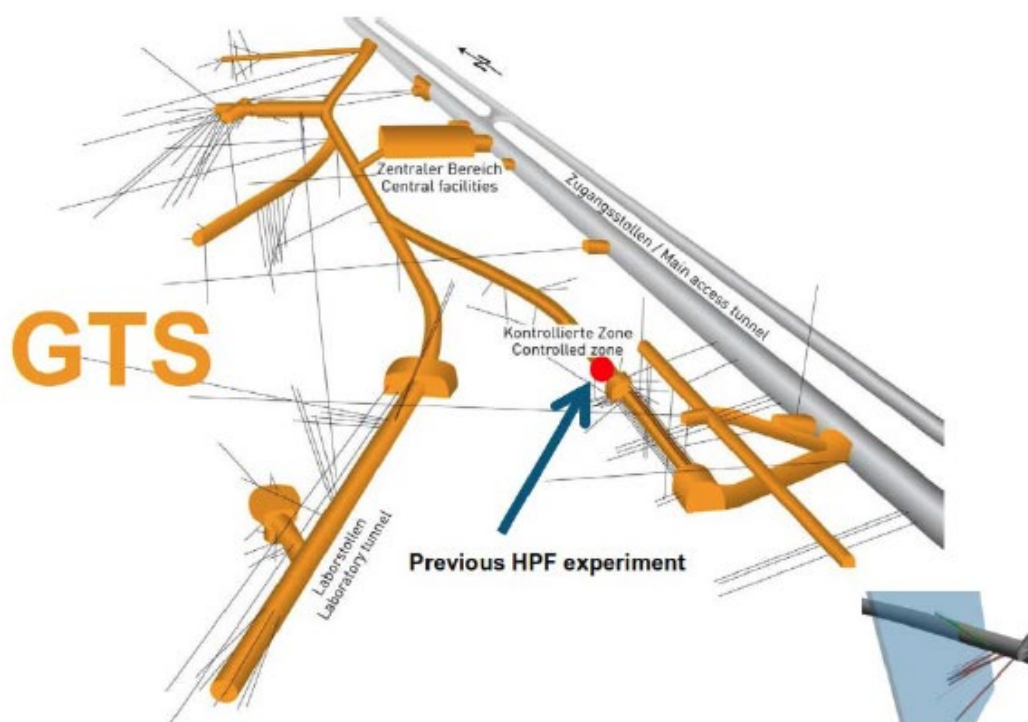


Fig. 2: Location of the CIM / HPF experiment at the Grimsel Test Site (Kontar et al. 2019)

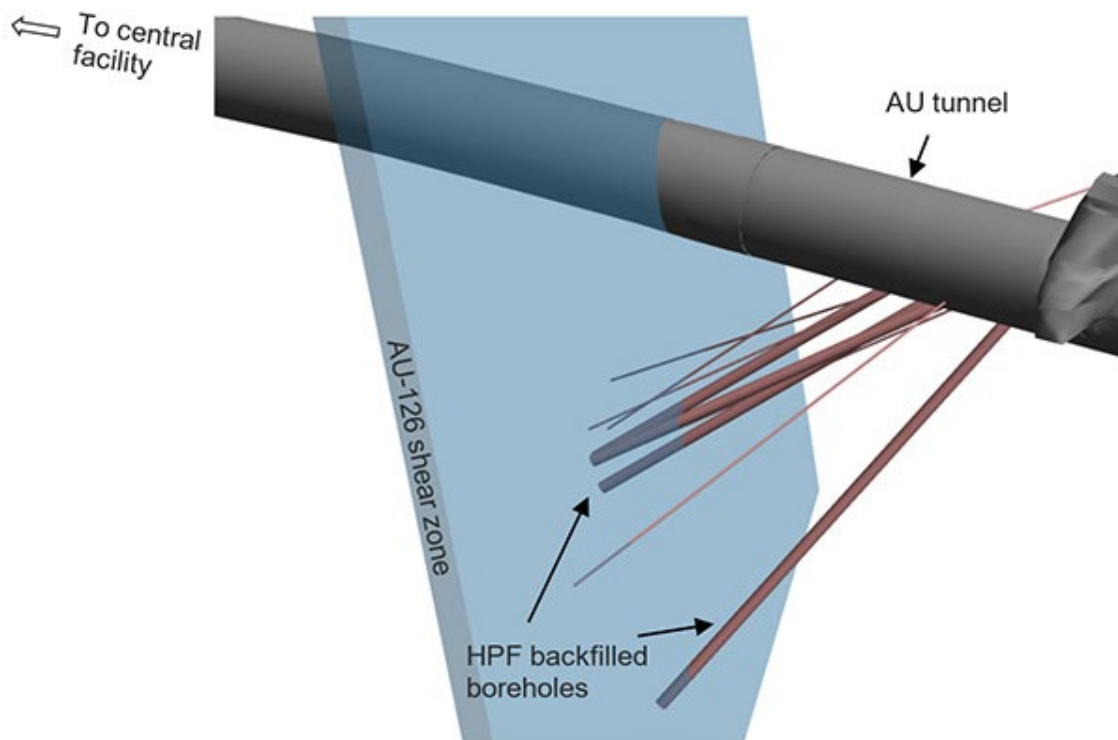


Fig. 3: Schematic 3D view of the HPF and planned CIM borehole relative to the AU-126 shear zone and AU tunnel at the GTS (GTS webpage, 2021)

3.2 Collection of the material

Two 50 mm cores of hardened cement paste (HCP) drilled from the cementitious infill of the upper part of the HPF 98.005 borehole were delivered to the ÚJV laboratory. The cementitious infill was based, according to the information available, on the CEM II/A-S 32.5 R cement mixture produced by the Sika Rock company. Following drilling and cutting, the two cores were packed in plastic foil under vacuum conditions in order to prevent reaction with the atmosphere (Fig. 4). Visually, the cementitious material appeared to be very heterogeneous.



Fig. 4: The as-delivered CIM₂ core

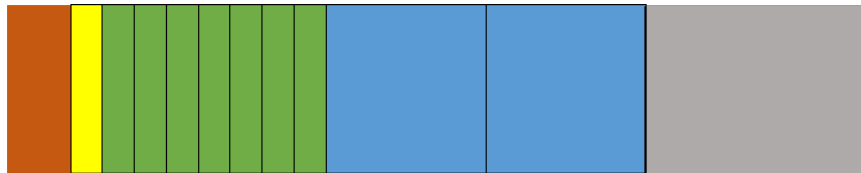
 SÚRAO	Migration of Carbon and Iodine in Cementitious Matrix – Final Report	Registration number:
		538/2021

The first core, labelled CIM_1, was approximately 28 cm long and was drilled from a depth of 59–87 cm beneath the invert atmosphere.

The second core, labelled CIM_2, was approximately 41 cm long and was drilled from a depth of 107 to 148 cm beneath the invert atmosphere.

3.3 Preparation of the samples for the experiments

As noted in the experimental plan, several types of experiments are underway, for each of which differently shaped samples were required. Thus, the HCP cores were cut and crushed according to the scheme shown in Fig. 5. so as to obtain samples for the hydraulic permeability (blue), diffusion (green) and sorption (brown) experiments and the XRD analysis (yellow). The cores were cut using a circular saw with a water-cooled diamond blade. All the resulting parts were stored under vacuum conditions in plastic foil.



CIM_1



CIM_2

Fig. 5: Core cutting scheme – samples for the hydraulic permeability (blue), diffusion (green) and sorption (brown) experiments and the XRD analysis (yellow)

3.3.1 Disc samples for the diffusion experiments and the measurement of porosity

Disc-shaped samples with thicknesses of 10 mm were cut from three different core regions (depths) for the purpose of the diffusion experiments, as shown in Fig. 5. Porosity measurements were taken from the same samples following the conclusion of the diffusion experiments.

 SÚRAO	Migration of Carbon and Iodine in Cementitious Matrix – Final Report	Registration number:
		538/2021

3.3.2 Crushed samples for the sorption and leaching tests and XRD analysis

Material from the top part of both cores was crushed and sieved. The size of the particles used in the sorption experiments was within a range of <0.25 mm and 0.25-1.0 mm, 0.5-1.0 mm and 1-2 mm. Particles of smaller than 0.25 mm were used in the leaching experiments, while material with mesh sizes of 0.25-1.0 mm was used in the sorption experiments. Crushed material with mesh sizes of 0.5-1.0 and 1-2 mm was used as the column infill for the column interaction experiments.

A small number of powdered samples were prepared via manual grinding in an agate mortar for the mineralogical analysis employing XRD. The powdered samples were stored under isopropanol so as to eliminate interaction with the atmosphere.

3.3.3 Cylinders for the determination of permeability

Cylindrical samples with thicknesses of 50 mm were cut from the middle part of each core as shown in Fig. 5.

3.4 Experimental solution

While many laboratory experiments commonly use distilled or demineralised water, demineralised water is a particularly aggressive solution that leads to the leaching/dissolution of cement. Therefore, a simple synthetic solution, so-called Evolved Cement Water (ECW), was used in the diffusion and sorption experiments.

The ECW was prepared as a saturated solution of portlandite in demineralised water with a calcium concentration of 2×10^{-2} M and pH = 12.5 at room temperature.

In contrast, demineralised water was used in the leaching tests.

 SÚRAO	Migration of Carbon and Iodine in Cementitious Matrix – Final Report	Registration number:
		538/2021

4 Experiments and methods

4.1 Porosity

The determination of porosity is important in terms of the evaluation of the transport properties of the tested materials. The literature describes several methods for the determination of the porosity of cementitious materials, e.g. the evaporable water content, re-saturation, solvent exchange, mercury porosity and nitrogen sorption methods (Day and Marsh 1988). However, all these methods have their advantages and disadvantages which are capable of affecting the pore structure of the cementitious material (Collier et al. 2016, Diamond 2000).

Porosity (in percent) is calculated as the ratio of the pore volume (V_P) and the total volume of the sample (V_S):

$$\varepsilon = \frac{V_P}{V_S} \cdot 100$$

4.1.1 Saturation and gravimetric method

The sample porosity values provided in this report were obtained via the gravimetric and saturation method as inspired by the determination of rock porosity published by Melnyk and Skeet (1986). The ÚJV laboratories have considerable experience of the use of this procedure on rock samples and other materials including concretes. The water-saturated, surface dry weight (W_S) was calculated from the drying curve. The weight of the submerged sample (W_A) was obtained via the weighing of the sample immersed in the ECW solution. A further required value consisted of the dry sample weight (W_D). In order to prevent the occurrence of phase changes and the evaporation of chemically-bonded water, the samples were dried carefully in a desiccator with CaCl_2 under vacuum conditions. The disadvantage of this process is that it is very time consuming.

The pore volume V_P and the total sample volume V_S were calculated from the determined values according to the following equations:

$$V_S = (W_S - W_A) / \rho$$

$$V_P = (W_S - W_D) / \rho$$

where ρ is the density of the solution used for the saturation of the sample. The sample porosity ε was then calculated as follows:

$$\varepsilon = \frac{V_P}{V_S} = \frac{(W_S - W_D)}{(W_S - W_A)}$$

 SÚRAO	Migration of Carbon and Iodine in Cementitious Matrix – Final Report	Registration number:
		538/2021

Note that the solution density was no longer required for the porosity calculations. Therefore, it was possible to use any appropriate liquid for the determination of the saturation and weight of the submerged sample.

With respect to the measurement of the porosity of the materials via the saturation and gravimetric method following the leaching/interaction experiment, isopropanol was used as the saturation medium so as to avoid the further interaction of the dried cementitious material following the leaching process.

4.1.2 Hg porosimetry

The mercury porosimetry technique is based on the penetration of mercury into the pores as a function of the applied pressure. Mercury does not wet most substances and will only penetrate pores when forced to do so under high pressure. The entry of mercury into the pores requires the application of pressure in inverse proportion to the pore size. In other words, large pores will fill first, with smaller pores filling at increasingly higher pressures. Mercury exhibits a high contact angle against most solids. Reported contact angles vary; they are $> 90^\circ$, with 130° being the most widely used value. Mercury thus penetrates into the pores only under the action of pressure. The volume of mercury injected into the porous system is generally interpreted as the total volume of the pores in the measured sample.

The measurement of the porosity of the samples via Hg porosimetry was performed by an external laboratory (Department of Inorganic Technology, University of Chemistry and Technology in Prague).

4.2 Permeability

The permeability of the cementitious samples was determined according to technical specification CEN ISO/TS 17892-11:2004, a method that employs a constant hydraulic head. Triaxial permeability testing equipment developed in-house with GDS ELDPC pumps was used for the measurements (Fig. 6). The hydraulic head was adjusted to 1 MPa and the background pressure in the device chamber was adjusted to 10 MPa.



Fig. 6: Apparatus for the determination of the filtration coefficient K_f at the ÚJV laboratory.

4.3 XRD analysis

The crystalline phases of the samples were identified by means of X-Ray Diffraction (XRD) analysis conducted at the Institute of Inorganic Chemistry, Czech Academy of Sciences.

Finely powdered materials were prepared for the XRD analysis and the powdered samples were tested using a PANalytical X'Pert PRO MPD diffractometer (Co $K\alpha$ radiation, 30mA, 40kV) within the range $8-100^\circ 2\theta$. The X-Ray Diffraction patterns obtained were evaluated using X'Pert HighScore Plus software in order to identify the phase composition.

4.4 TGA analysis

The thermogravimetric analysis (TGA) of the cement materials following leaching/interaction with water were studied and the analysis conducted at an external laboratory (Institute of Inorganic Chemistry, Czech Academy of Sciences).

The fine powdered materials were prepared for the TGA analysis in the same way as for the XRD analysis. The powdered samples were tested using a Setaram SetSys Evolution device.

The samples were heated in capped corundum crucibles in the temperature range $30-1000^\circ\text{C}$ with a heating rate of $10^\circ\text{C}/\text{min}$ in an inert atmosphere (argon). The specific gas flow was set at 60 ml/min.

4.5 Predictive geochemical modelling

4.5.1 Modelling of the interaction of the cementitious material with water

The predictive modelling of the interaction between the tested cementitious materials and the experimental solutions was performed using PHREEQC software.

Two types of interaction were modelled: the dissolution of the CIM cementitious material in demineralised water and the dissolution of the CIM material in Grimsel groundwater. The ratio of the solid to the liquid phase (S/L) was determined at a value of 1/10. The concentration of ions present in the Grimsel groundwater determined for modelling purposes is listed in Tab. 3; the distilled water contained no dissolved ions. The input parameters for the solid phases consisted of the results of the XRD quantitative phase analysis (see Tab. 6) of the cementitious material obtained from three different depth levels of the drilled core sample. The interaction process was modelled to attain equilibrium under laboratory conditions (i.e. 25°C and the presence of oxygen in the air).

Tab. 3: Composition of the input Grimsel groundwater used in the predictive modelling

c (mol/l)	Na ⁺	K ⁺	Ca ²⁺	Mg ²⁺	pH	
	3.61×10^{-4}	5.12×10^{-6}	1.87×10^{-4}	3.70×10^{-7}		9.2
	Cl ⁻	SO ₄ ²⁻	CO ₃ ²⁻	F ⁻		
	1.21×10^{-5}	5.87×10^{-5}	3.20×10^{-4}	2.05×10^{-4}		

4.5.2 Modelling of the chemical speciation of the tracers

The modelling of the chemical forms of the used tracers (iodide, acetate and formate) was performed using The Geochemist's Workbench. This software, which is used for geochemical modelling in aqueous systems, allows for the creation of Eh-pH diagrams, the calculation of speciation in equilibrium etc.

4.6 Aerobic and anaerobic conditions

A number of sorption, diffusion and leaching/interaction experiments were performed under anaerobic conditions so as to allow for the comparison of the behaviour of the carbon tracers and the interaction of the cementitious materials with water with and without the presence of air (i.e. oxygen and carbon dioxide) and in an inert argon atmosphere.

4.6.1 Aerobic conditions

The experiments conducted under aerobic conditions (the presence of oxygen and carbon dioxide) were performed in a standard laboratory environment at $23 \pm 1^\circ\text{C}$.

4.6.2 Anaerobic conditions

The experiments under anaerobic conditions were performed in a Jacomex anaerobic glovebox (Fig. 7) with an argon atmosphere (<1 ppm O_2 and 0.0% CO_2 on average) at $23 \pm 1^\circ C$.

It was necessary to dispose of the air from the materials, samples, solutions and equipment and to allow for equilibrium with the internal inert atmosphere prior to the commencement of experimentation. Before being placed in the glovebox, the cement samples and the auxiliary equipment were conditioned in a transition chamber. The addition of the tracer solution to the cement samples and the shaking and sampling of the liquid phase above the solution were performed in the glovebox, which rendered the work somewhat difficult and time-consuming. The centrifugation of the liquid phase and the preparation of the liquid sample for measurement were performed under aerobic conditions. Therefore, it was necessary to place all the materials (solid and liquid) in the glovebox at least 2 weeks prior to the start of the experiments.



Fig. 7: Anaerobic glovebox with an inert argon atmosphere

4.7 Leaching and interaction experiments

4.7.1 Leaching experiments

The leaching experiments were arranged in the form of batch reactors. Since the tested materials evinced a high level of moisture, the water content was determined in advance and the sample weight subsequently corrected to the dry mass. Demineralised water or a saturated solution of $Ca(OH)_2$ was used as the leaching solution. Three different types of solid state materials were used (powdered, crushed, coupons).

 SÚRAO	Migration of Carbon and Iodine in Cementitious Matrix – Final Report	Registration number:
		538/2021

The leaching experiments on the coupon samples were performed under standard laboratory conditions or in the inert atmosphere of the anaerobic glovebox (argon atmosphere). The coupons were prepared in the shape of half discs (1 cm thick) that were sawn from the drilled core from three different depths. Each of these coupons leached into 0.5 l of the liquid phase, which was changed periodically for fresh liquid. The chemical composition of the liquid phases was analysed after each of the leaching steps. Images of the coupons and a description of the experimental conditions are presented in Fig. 8. Following the end of the experiment, the solid phase was dried under anaerobic or laboratory conditions according to the experiment. Small pieces of dried coupons were chipped off for porosimetry measurement purposes and part of the material was crushed in an agate mortar for approximately 10 minutes under laboratory conditions. The mineralogical composition of these samples was determined via XRD analysis.

The second types of materials studied comprised crushed CIM_1 and CIM_2 cement pastes. These solid phase samples were prepared in the same way as for the sorption experiments. Defined amounts of the cement materials of these samples were placed in contact with the ECW for 56 days; the sample weight to the solution volume ratio ($m:V$) was adjusted to $0.1 \text{ g}\cdot\text{cm}^{-3}$. Following the end of the experiment, the solid phase was allowed to dry under anaerobic conditions and then crushed in an agate mortar for approximately 10 minutes under laboratory conditions. The mineralogical composition of these samples was determined via XRD analysis.

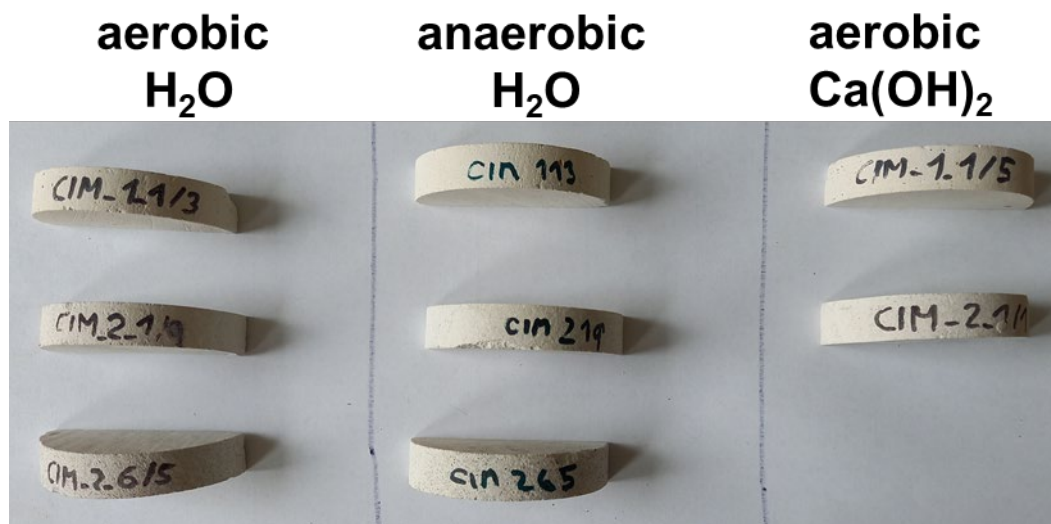


Fig. 8: Coupon samples prepared for the leaching experiments under different experimental conditions

The third type of material studied via the leaching test comprised powdered material from the drilled core taken from three different depths. The material was crushed in a mortar so as to form a very fine powder. This type of experiment involved the leaching of 0.5 g of powdered material into 0.5 l of deionised water under laboratory conditions. The experimental suspension was stirred using a magnetic stirrer so as to ensure the ideal contact of the solid/liquid phases. The liquid phase was changed periodically for fresh liquid. The chemical composition of the liquid phases was analysed after each leaching step.

 SÚRAO	Migration of Carbon and Iodine in Cementitious Matrix – Final Report	Registration number:
		538/2021

The leaching of the samples was followed by changes in the leaching solution. The parameters determined consisted of the pH, conductivity, cation concentration (Na^+ , K^+ , Ca^{2+} , Sr^{2+} , Mg^{2+} , $\text{Fe}^{2+/3+}$, Al^{3+}) and anion concentration (SO_4^{2-} , Cl^- , $\text{HCO}_3^-/\text{CO}_3^{2-}$, SiO_4^{4-}).

4.7.2 Interaction experiments

The interaction experiments were conducted in the form of column experiments employing crushed material with mesh sizes of 0.5–1.0 and 1–2 mm. The crushed material was poured into small laboratory-made columns (see Fig. 9).

The columns were connected via tubing to the input reservoir containing distilled water and the flow of the water through the columns was ensured via a peristaltic pump at a water flow velocity of 7-8 ml per hour. (Fig. 10). The column interaction experiments were performed under standard laboratory conditions.

The interaction of the cementitious material with the water was followed by the conducting of a chemical analysis. The parameters determined consisted of the pH, conductivity, cation concentration (Na^+ , K^+ , Ca^{2+} , Sr^{2+} , Mg^{2+} , $\text{Fe}_{(\text{tot})}$, $\text{Al}_{(\text{tot})}$) and anion concentration (SO_4^{2-} , Cl^- , $\text{HCO}_3^-/\text{CO}_3^{2-}$, SiO_3^{2-}).



Fig. 9: Small column with the crushed cementitious material

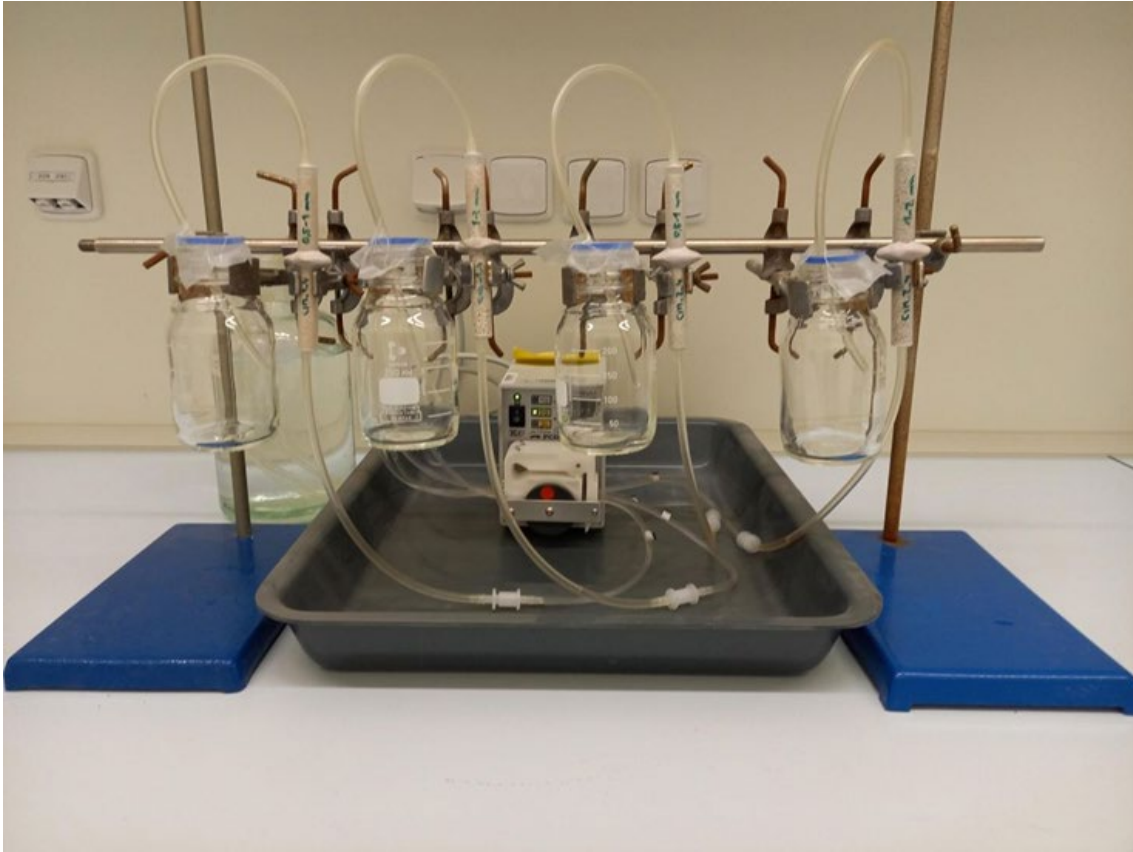


Fig. 10: Experimental setup of the column interaction experiments

4.8 Sorption experiments

The sorption experiments were arranged in the form of batch reactors and conducted on the CIM_1 and CIM_2 materials with particle sizes of <0.25 mm and 0.25–1.00 mm. Hardened CEM I and CEM II cement pastes were used for comparison purposes. Information on the origin and previous processing of the samples is available in Brázda et al. 2019.

Sorption experiments should be evaluated in the equilibrium state between the solid material and the surrounding solution. As was demonstrated in a previous project that focused on cementitious materials (Večerník et al. 2019b) with respect to CEM II/A-S 42.5 R hardened cement paste in a $\text{Ca}(\text{OH})_2$ saturated solution, equilibrium was not attained even after 84 days for the $^{125}\text{I}^-$ tracer. Based on this experience, therefore, a reference time of 56 days was selected for the comparison of the sorption results for the various materials. Once the experiment was terminated, the solid material and the solution were separated by means of centrifugation or filtration if required.

4.8.1 Experimental procedure

Since the tested materials evinced a high level of moisture, the water content was determined in advance and the sample weight was corrected to the dry mass. ECW (a saturated portlandite solution) was used as the experimental solution. The sorption experiments were arranged in the form of batch reactors. The sample weight to the solution volume ($m:V$) was adjusted to $0.1 \text{ g}\cdot\text{cm}^{-3}$. Samples of cement paste of a given particle size were weighed directly into plastic

 SÚRAO	Migration of Carbon and Iodine in Cementitious Matrix – Final Report	Registration number:
		538/2021

vials and the ECW with the tracer was then added to the vials. 3 samples were prepared for 3 parallel determinations for each material, sampling time interval, tracer and conditions (aerobic/anaerobic). In addition, 2 vials containing the reference solution of the tracer without the solid-phase samples were prepared for each set of samples. These solutions were further processed in the same manner as the cement samples so as to eliminate bias in the results due to the sorption of the tracer on the walls of the vials and other factors. Vials with the cementitious material and solution were placed on a horizontal shaker and shaken at a frequency of 120 rpm. Two differing initial concentrations of iodine and carbon species were applied using non-active carriers: $10^{-4} \text{ mol}\cdot\text{l}^{-1}$ and $10^{-6} \text{ mol}\cdot\text{l}^{-1}$. Finally, appropriate carrier solutions were labelled using the ^{125}I or ^{14}C tracers. The containers with the material and solution suspensions were placed on a rotating mixer or horizontal shaker.

Samples of the liquid phases of the suspension were taken at defined time intervals during the experiment for the CIM_1 and CIM_2 materials; the vials were removed from the shaker and the solid material and the solution were separated by means of centrifugation.

Following the sorption experiments performed in the anaerobic glovebox, the vials were removed from the shaker, left for 1 hour in a rack to settle, and 1.5 ml of the solution above the solid phase was then transferred to a plastic Eppendorf tube. The samples of the experimental solutions were then removed from the glovebox for further processing under laboratory conditions. The solid material and the liquid phase were separated by means of centrifugation (Centrifuge 5415 D, 10 000 rpm, 10 min).

4.8.2 Experimental solutions with the ^{14}C and ^{125}I tracers

All the sorption experiments were performed using a saturated portlandite solution (see Chapter 3.4) with ^{125}I and ^{14}C tracers together with a non-active carrier that had been added to the reactors.

- 1) ^{125}I ($T_{1/2} = 59.4 \text{ d}$) as Na^{125}I with an initial volume activity of $0.8 \text{ kBq}\cdot\text{ml}^{-1}$ and concentrations of the non-active carrier CaI_2 $c(\text{I}^-) = 10^{-4} \text{ mol l}^{-1}$ and $10^{-6} \text{ mol}\cdot\text{l}^{-1}$. A solution of $\text{Na}_2\text{S}_2\text{O}_3$ was also added to the experimental solution so as to eliminate the oxidation of I^- .

The gamma activity of the ^{125}I tracer was detected by means of a 2480 WIZARD2 gamma counter (Wallac Oy) equipped with an NaI(Tl) detector.

- 2) ^{14}C ($T_{1/2} = 5.730 \text{ y}$) as sodium formate ($\text{H}^{14}\text{COONa}$) and sodium acetate ($\text{CH}_3^{14}\text{COONa}$) with an initial volume activity of $0.7 \text{ kBq}\cdot\text{ml}^{-1}$ and concentrations of the non-active carrier CH_3COONa of $10^{-4} \text{ mol}\cdot\text{l}^{-1}$ and $10^{-6} \text{ mol}\cdot\text{l}^{-1}$. Based on the results of previously published experiments (Brázda et al. 2019, Večerník et al. 2017, Večerník et al. 2019a, b, c), a carrier-free arrangement was chosen for the experiments with the ^{14}C formate tracer. The initial volume activity of these solutions was set at $370 \text{ Bq}\cdot\text{ml}^{-1}$.

The β^- radiation was detected by means of a Hidex 300 SL Liquid Scintillation Counter (LSC) (Hidex Oy); all the liquid phase samples containing the ^{14}C tracers were mixed with a scintillation cocktail (Rotiszint® eco plus, ROTH) for the measurement of the activity.

 SÚRAO	Migration of Carbon and Iodine in Cementitious Matrix – Final Report	Registration number:
		538/2021

4.8.3 Evaluation of the sorption experiments

Sorption is described via the distribution coefficient R_d ($\text{ml}\cdot\text{g}^{-1}$) and the sorption yield η (%):

$$R_d = \frac{(c_0 - c) \cdot V}{c \cdot m},$$

$$\eta_{\text{sorpce}} = \frac{(c_0 - c)}{c_0} \cdot 100,$$

where c_0 indicates the initial concentration of the sorbing specie ($\text{mol}\cdot\text{l}^{-1}$), c is the concentration of the sorbing specie in the solution at the end of the experiment ($\text{mol}\cdot\text{l}^{-1}$), V is the volume of the experimental solution (ml) and m is the dry weight of the solid material (g).

The values used for the quantification of sorption were obtained from three parallel determinations (only two parallel determinations were performed in the case of the CIM_1 samples with a particle size of <0.25 mm due to a lack of material), concerning which each sample was measured three times. The resulting values comprised the medians of these values. The stated uncertainties were calculated as the combined expanded ($k = 2$) uncertainty of the determination.

4.9 Diffusion experiments

Fick's laws are used to describe the diffusion transport of tracers (contaminants) through the pore structures of materials. The diffusion coefficients of non-sorbing and weakly-sorbing tracers in the equilibrium state are usually determined by means of through diffusion experiments.

The through diffusion experiment apparatus is shown in the Interim report (Brázda et al., 2019); the geometry of the setup was modified from Skagius and Neretnieks (1986). The diffusion cell is made of PMMA. The samples (sealed in silicon) were placed between two reservoirs; the inlet reservoir contained the experimental solution with the tracer while the outlet reservoir contained only the experimental solution. The volume activity of the tracer in the inlet reservoir was not kept constant. In order to be able to apply a simplified analytical solution for the determination of the effective diffusion coefficient, the volume activity of the tracer should not decrease to beneath 95% of the initial value. The increase in the activity of the tracer volume in the outlet reservoir was observed during the conducting of the through diffusion experiments.

Diffusion experiments performed in 2020 compared the behaviour of the diffusion process of a ^{14}C tracer in the chemical form of formate under aerobic (standard laboratory) and anaerobic (glovebox with an inert argon atmosphere) conditions (Fig. 11).



Fig. 11: Diffusion experiment performed in an inert atmosphere in the anaerobic glovebox

4.9.1 Experimental solutions with the ^3H , ^{14}C and ^{125}I tracers

All the diffusion experiments were performed with a saturated solution of portlandite (see Chapter 3.4), to which three different tracers were added to the inlet reservoirs:

- 1) HTO ($T_{1/2} = 12.32$ y) solution with an initial volume activity of $4.5 \text{ kBq}\cdot\text{ml}^{-1}$. The β^- radiation was detected by means of a Hidex 300 SL Liquid Scintillation Counter (LSC) (Hidex Oy); all the samples of the liquid phase containing the ^3H tracer were mixed with a scintillation cocktail (Rotiszint® eco plus, ROTH) for the measurement of the activity.
- 2) ^{14}C ($T_{1/2} = 5.730$ y) as sodium formate ($\text{H}^{14}\text{COONa}$) and sodium acetate ($\text{CH}_3^{14}\text{COONa}$) with an initial volume activity of $1.3 \text{ kBq}\cdot\text{ml}^{-1}$ and non-active carrier concentration of $10^{-4} \text{ mol}\cdot\text{l}^{-1}$. The β^- radiation was detected by means of a Hidex 300 SL Liquid Scintillation Counter (LSC) (Hidex Oy); all the samples of the liquid phase containing the ^{14}C tracers were mixed with a scintillation cocktail (Rotiszint® eco plus, ROTH) for the measurement of the activity.
- 3) ^{125}I ($T_{1/2} = 59.4$ d) as Na^{125}I with an initial volume activity of $1.5 \text{ kBq}\cdot\text{ml}^{-1}$ and non-active carrier concentration of $\text{CaI}_2 \text{ c(I}^-) = 10^{-4} \text{ mol}\cdot\text{l}^{-1}$; $\text{Na}_2\text{S}_2\text{O}_3$ was also added to the experimental solution so as to eliminate the oxidation of I^- . The gamma radiation was detected by means of a 2480 WIZARD2 gamma counter (Wallac Oy) equipped with an NaI(Tl) detector.

4.9.2 Evaluation of the through diffusion experiments

The experimental data was evaluated via the fitting of the activity (molar amount) increase in the outlet reservoir over time t (s) using the analytical solution of Fick's 2nd law:

$$\frac{\partial C}{\partial t} = \frac{D_e}{\alpha} \left(\frac{\partial^2 C}{\partial x^2} \right),$$

where C ($\text{mol}\cdot\text{m}^{-3}$ or $\text{Bq}\cdot\text{m}^{-3}$) is the concentration or volume activity in the pore water and D_e ($\text{m}^2\cdot\text{s}^{-1}$) indicates the effective diffusion coefficient. The capacity factor α is defined as:

$$\alpha = \varepsilon + \rho_d \cdot K_d,$$

with porosity ε (–), bulk density ρ_d ($\text{kg}\cdot\text{m}^{-3}$) and the distribution coefficient K_d ($\text{m}^3\cdot\text{kg}^{-1}$).

The effective diffusion coefficient D_e and the porosity ε are calculated by means of the following analytical solution (Crank 1975, Jakob et al. 2004):

$$Q(t) = S \cdot L \cdot C_0 \cdot \left[\frac{D_e \cdot t}{L^2} - \frac{\alpha}{6} - \frac{2\alpha}{\pi^2} \sum_{n=1}^{\infty} \frac{(-1)^n}{n^2} \cdot \exp\left(-\frac{D_e \cdot n^2 \cdot \pi^2 \cdot t}{L^2 \cdot \alpha}\right) \right],$$

where $Q(t)$ (mol or Bq) indicates the total transferred molar amount or activity at time t (s) through a sample with a thickness L (m) and area S (m^2). The inlet tracer concentration/activity C_0 ($\text{mol}\cdot\text{m}^{-3}$ or $\text{Bq}\cdot\text{m}^{-3}$) is considered to be constant.

When the diffusion flux turns to the steady state ($t \rightarrow \infty$), the solution can be simplified as:

$$\frac{Q(t)}{S \cdot C_0} = \frac{D_e \cdot t}{L} - \frac{\alpha \cdot L}{6}.$$

The effective diffusion coefficient D_e can be determined as the slope of $Q(t)/(S \cdot C_0)$ depending on the time t . This form of evaluation is known as the time-lag method. A more detailed description of the evaluation of through diffusion experiments can be found in Van Loon et al. (2003) or Večerník et al. (2019c).

The optimal values for D_e and α were determined by fitting the experimental data to the analytical solution equation by means of the least squares method. A knowledge of the reference tracer diffusion coefficients in water at infinite dilution ($\text{m}^2\cdot\text{s}^{-1}$) also allowed for the calculation of parameters such as the geometric factor G (–) and the formation factor F_f (–):

$$D_e = \varepsilon \cdot D_p = \varepsilon \cdot D_w \cdot G = F_f \cdot D_w$$

5 Results

5.1 Porosity of the source material

The porosity of cementitious materials can be evaluated with quite a high level of accuracy by means of the saturation and gravimetric method (see Tab. 4). Clearly, a strong correlation exists between the porosity of the sample and the sampling depth.

It was confirmed that the saturation and gravimetric method for the determination of porosity produced results that compared to those of the mercury porosimetry method, which required special equipment and was limited by the maximum volume/dimensions of the samples. While this is not a problem issue in the case of cement pastes, with respect to other types of cement-based materials, such as mortars and concretes, samples with small dimensions are unable to fully represent the composition of the material (due to the presence of sand, gravel and other coarse particles) and, thus, cannot be accurately evaluated via the Hg porosimetry method.

Tab. 4: Porosity values of the source material

	<i>avg. depth (m)</i>	<i>saturation and gravimetric ε (%)</i>	<i>Hg porosimetry ε (%)</i>
CIM_1_1	0.65	~ 51	49.96
CIM_2_1	1.15	~ 43	42.71
CIM_2_6	1.44	~ 35	32.15

For the purpose of comparison, another project on cementitious materials (Večerník et al. 2019c) that considered samples of CEM II/A-S 42.5 R cement determined porosity values of $33 \pm 3\%$ and $39 \pm 2\%$ for a hardened cement paste with water to cement ratios of $w/c = 0.5$ and $w/c = 0.6$ respectively.

5.2 Permeability of the source material

Two cylindrical specimens (diameter 50 mm, height 50 mm) were tested from each core, i.e. from two different depths of the drilled core (approx. 70 and 120 cm). Prior to the permeability test, the cylindrical specimens were fully (re)saturated with water so as to eliminate the effects of the potential drying out of the drilled core sample during transport and storage prior to the experiments.

For the purpose of comparison, the determined filtration coefficients k_T (for the temperature T of the measurement) were recalculated (see Tab. 5) to a temperature of $T = 10^\circ\text{C}$ (the reference temperature of soil as set out in the CEN ISO/TS technical specification).

Tab. 5: Permeability (filtration coefficient)

	k_{10} (m·s ⁻¹)
CIM_1	$(4.9 \pm 0.2) \times 10^{-10}$
CIM_2	$(2.3 \pm 0.6) \times 10^{-11}$

The determined k_{10} filtration coefficients for the material from the upper part (depth approx. 70 cm) of the drilled core evinced almost one order of magnitude higher values than the material taken from a depth of approx. 120cm. This corresponds to the porosity values, which also decrease with depth. The changes in both parameters confirmed the heterogeneity of the CIM cement paste material taken from the upper parts of the drilled core.

5.3 XRD analysis of the source material

An example of the XRD pattern of the initial source material is shown in Fig. 12. The results of the quantitative phase determination are summarised in Tab. 6 and Fig. 13.

Increased amounts of dolomite and quartz were determined for the materials sampled from the deeper parts of the drilled core. The amounts in the initial materials allowed for the determination of the ratio of the amorphous phases present in the materials.

All the XRD patterns and TGA analysis plots of the initial source materials (CIM_1_1, CIM_2_1 and CIM_2_6) are presented in Fig. 66 – Fig. 71 in the Appendix.

Tab. 6: XRD quantitative phase analysis of the CIM materials

wt. %		CIM_1_2	CIM_2_1	CIM_2_6
amorphous	–	38.6	42.8	37.9
calcite	CaCO ₃	28.4	23.1	22.9
portlandite	Ca(OH) ₂	5.9	6.0	3.6
dolomite	CaMg(CO ₃) ₂	6.1	10.0	22.3
CSH phases	$x\text{CaO} \cdot y\text{SiO}_2 \cdot z\text{H}_2\text{O}$	6.0	5.6	3.7
ettringite	Ca ₆ Al ₂ (SO ₄) ₃ (OH) ₁₂ ·26H ₂ O	5.1	3.1	2.5
hydrocalumite	Ca ₂ Al(OH) _{6,5} Cl _{0,5} ·3H ₂ O	4.7	3.7	2.7
monocarbonate	3CaO·Al ₂ O ₃ ·CaCO ₃ ·11H ₂ O	3.3	3.7	1.4
quartz	SiO ₂	0.7	1.1	2.5
katoite	Ca ₃ Al ₂ (SiO ₄) _{3-x} (OH) _{4x}	1.2	1.0	0.5

UV Brazda, Cement C213, as received
 05-0586 (*) - Calcite, syn - CaCO3
 44-1481 (*) - Portlandite, syn - Ca(OH)2
 36-0426 (*) - Dolomite - CaMg(CO3)2

46-1045 (*) - Quartz, syn - SiO2
 72-0646 (C) - Ettringite - Ca6(Al(OH)6)2(SO4)3(H2O)25.7
 31-0345 (I) - Hydrocalumite, syn - beta-Ca4Al2O6Cl2.10H2O
 41-0219 (*) - Calcium Aluminum Oxide Carbonate Hydrate - Ca4Al2O6CO3.11H2O/3C

24-0217 (*) - Katoite, syn - Ca3Al2(OH)12

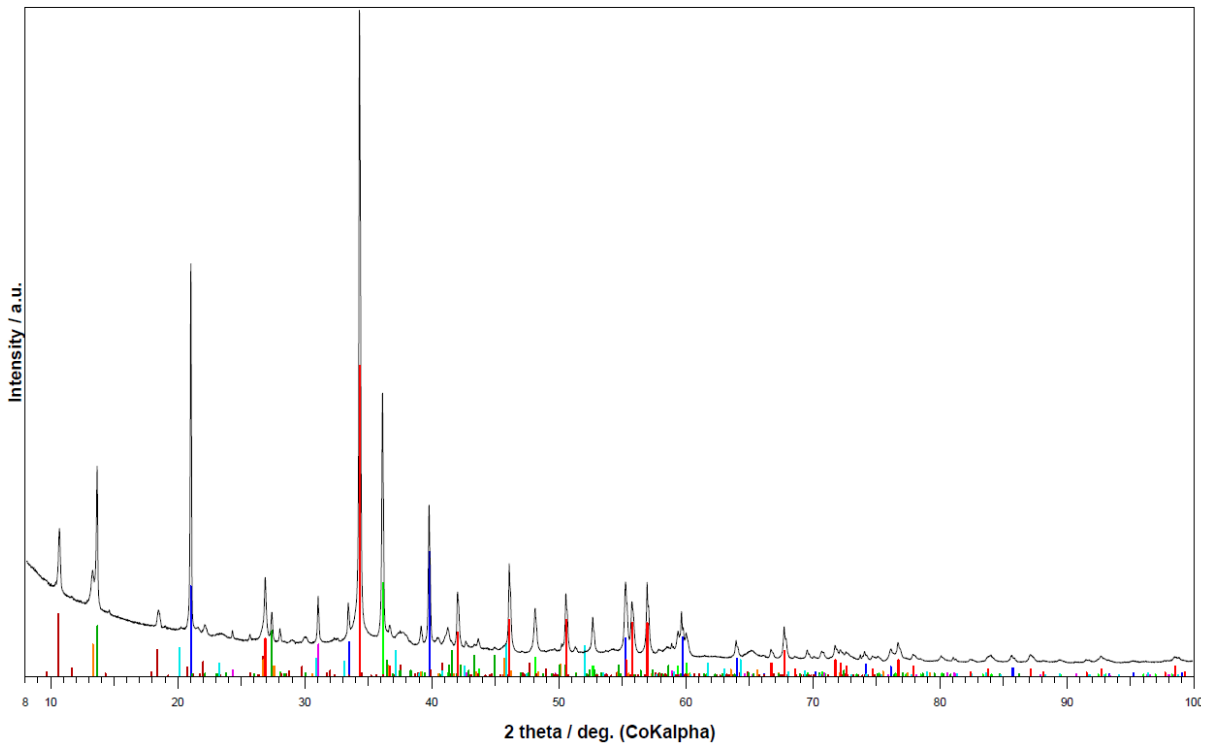


Fig. 12: XRD pattern of the CIM_2_1 sample

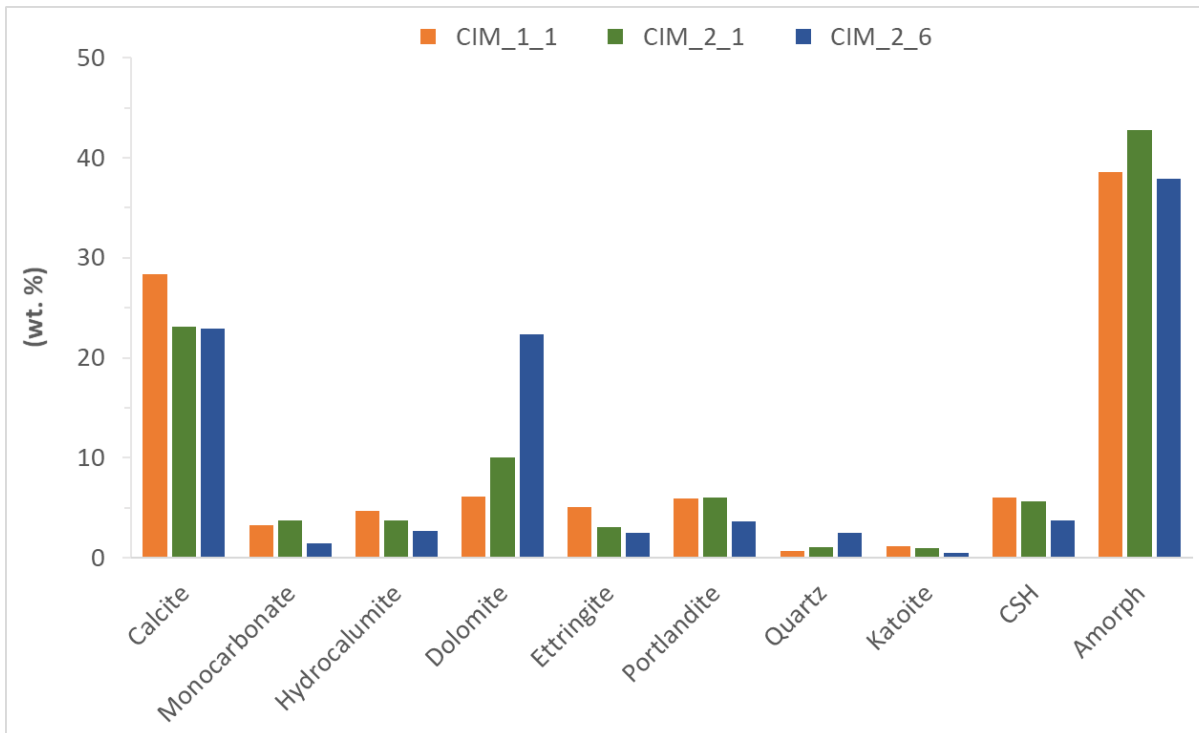


Fig. 13: XRD quantitative phase analysis of the CIM materials

5.4 Predictive geochemical modelling results

5.4.1 Models of the interaction of the CIM cement material with water

The results of the predictive modelling of the interaction between the cementitious materials and the demineralised water and Grimsel groundwater are shown in Tab. 7 in the form of the concentration of dissolved ions.

The modelled results principally revealed enhanced calcium, magnesium and sulphate ion concentrations and decreased concentrations of carbonate ions in the equilibrated solutions following interaction.

It will be possible to compare the data obtained from the modelling procedure (the concentrations of ions in the solution) to the results of the interaction of groundwater with the cement material as determined by the *in-situ* test.

Tab. 7: Results of the predictive interactive modelling – composition of the equilibrated solutions

c (mol/l)	CIM 1-2		CIM 2-1		CIM 2-6	
	Grimsel w.	DW	Grimsel w.	DW	Grimsel w.	DW
Na ⁺	3.61 × 10 ⁻⁴	-	3.61 × 10 ⁻⁴	-	3.61 × 10 ⁻⁴	-
K ⁺	5.11 × 10 ⁻⁶	-	5.11 × 10 ⁻⁶	-	5.12 × 10 ⁻⁶	-
Ca ²⁺	1.54 × 10 ⁻²	1.62 × 10 ⁻²	1.38 × 10 ⁻²	1.56 × 10 ⁻²	1.49 × 10 ⁻²	1.54 × 10 ⁻²
Mg ²⁺	3.00 × 10 ⁻²	2.24 × 10 ⁻²	3.25 × 10 ⁻²	1.95 × 10 ⁻²	6.26 × 10 ⁻³	5.40 × 10 ⁻³
Cl ⁻	1.60 × 10 ⁻²	1.60 × 10 ⁻²	1.20 × 10 ⁻²	1.20 × 10 ⁻²	1.00 × 10 ⁻²	1.00 × 10 ⁻²
SO ₄ ²⁻	3.58 × 10 ⁻³	2.40 × 10 ⁻³	4.01 × 10 ⁻³	2.36 × 10 ⁻³	2.50 × 10 ⁻³	1.86 × 10 ⁻³
CO ₃ ²⁻	8.87 × 10 ⁻⁶	8.61 × 10 ⁻⁶	9.17 × 10 ⁻⁶	8.59 × 10 ⁻⁶	8.20 × 10 ⁻⁶	8.19 × 10 ⁻⁶
F ⁻	2.05 × 10 ⁻⁴	-	2.05 × 10 ⁻⁴	-	2.05 × 10 ⁻⁴	-
Al (tot)	2.01 × 10 ⁻⁵	3.64 × 10 ⁻⁵	2.15 × 10 ⁻⁵	3.64 × 10 ⁻⁵	3.81 × 10 ⁻⁵	5.82 × 10 ⁻⁵
Si (tot)	4.48 × 10 ⁻⁶	4.66 × 10 ⁻⁶	4.96 × 10 ⁻⁶	4.63 × 10 ⁻⁶	4.84 × 10 ⁻⁶	5.06 × 10 ⁻⁶
pH	12.51	12.41	12.54	12.41	12.29	12.25

5.4.2 Models of the chemical speciation of the tracers

The modelling of the chemical forms of the tracers applied (iodide, acetate, formate) focused on the determination of the tracer speciation under the conditions of the interaction of Grimsel groundwater with the cement material. The composition of the interacting water, a temperature of 25°C and aerobic conditions were used as the input data for the speciation models.

Although The Geochemist's Workbench modelling software employs its own geochemical databases for calculation purposes, it is necessary to revise the output, theoretical chemical form and phase data. For example, in the case of the modelling of the iodine speciation in the region of very low pH and high Eh values, elementary iodine in the solid form could occur as the result of the theoretical calculation. An example is illustrated in Fig. 14. This is neither realistic nor relevant with respect to cementitious environments. The formation and presence of solid phases can be suppressed in the model so as to attain more realistic results (see Fig.

15). The speciation of the organic carbon tracers (acetate and formate) at initial concentrations of 10^{-4} and 10^{-6} mol/l are shown in Fig. 16 and Fig. 17.

The modelling proved that the tracers maintained their chemical forms (iodide, acetate, formate ions) and that no changes can be expected to occur under the conditions that pertain following the interaction of Grimsel groundwater and the CIM cementitious material; this also applies to laboratory experimentation conditions.

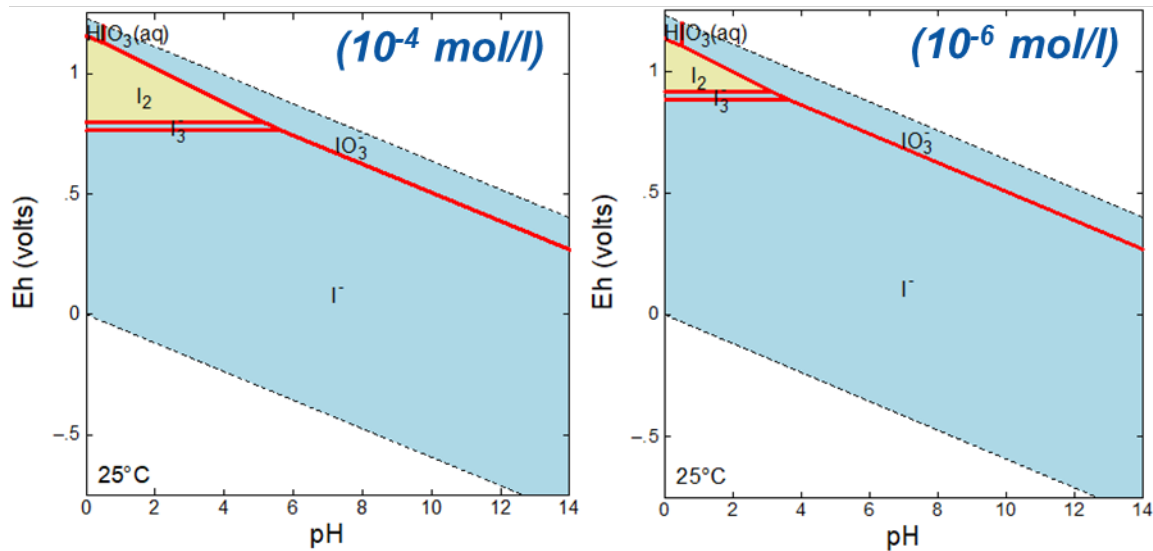


Fig. 14: Diagram of the iodine speciation for iodide tracer concentrations of 10^{-4} and 10^{-6} mol/l; without the suppression of the theoretical solid phases

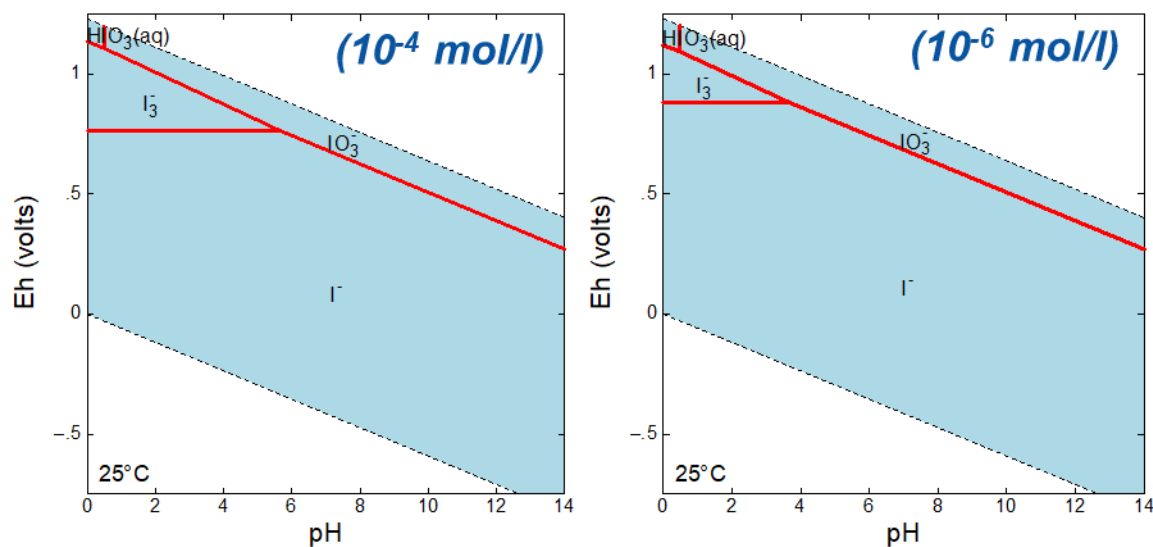


Fig. 15: Diagram of the iodine speciation for iodide tracer concentrations of 10^{-4} and 10^{-6} mol/l; with the suppression of the theoretical solid phases

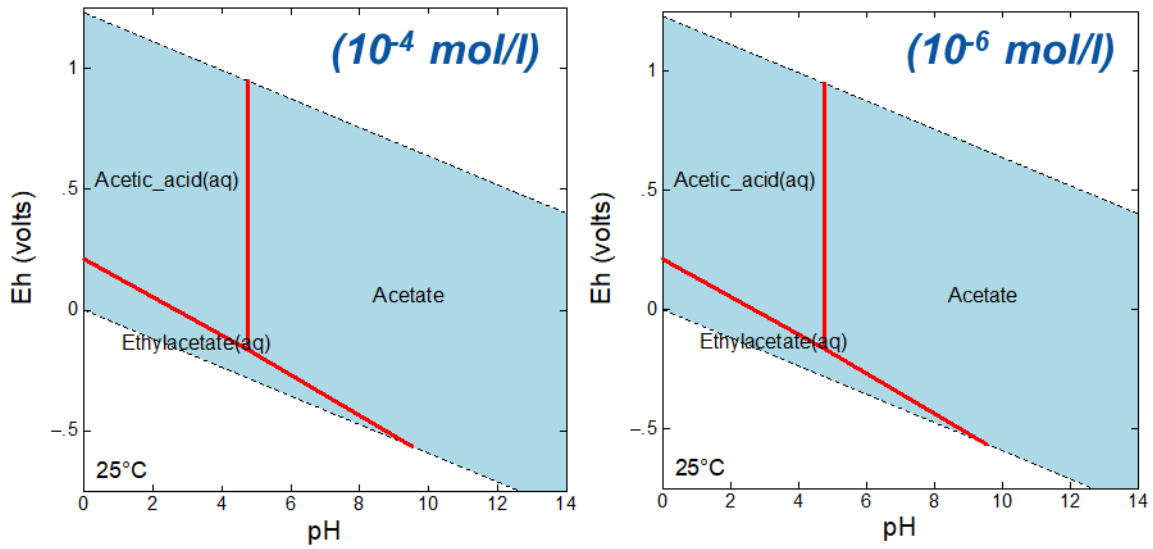


Fig. 16: Diagram of the organic carbon speciation for acetate tracer concentrations of 10^{-4} and 10^{-6} mol/l

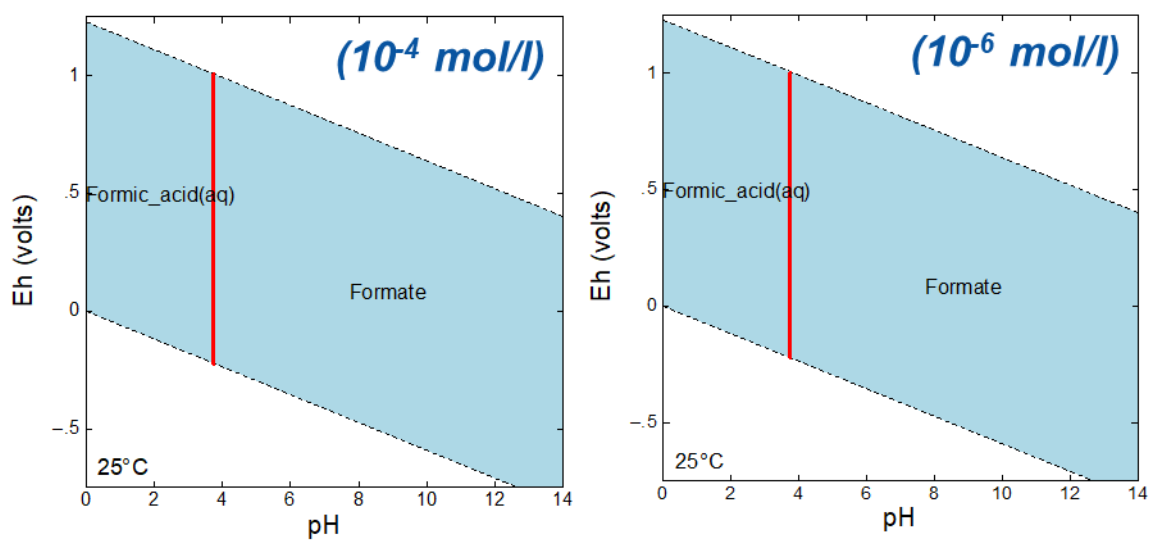


Fig. 17: Diagram of the organic carbon speciation for formate tracer concentrations of 10^{-4} and 10^{-6} mol/l

 SÚRAO	Migration of Carbon and Iodine in Cementitious Matrix – Final Report	Registration number:
		538/2021

5.5 Leaching and interaction experiments - chemical analysis

5.5.1 Leaching experiments – chemical analysis of the liquid phases

The leaching of the samples into deionised water and the calcium hydroxide solution was performed as described in chapter 4.7.1. The chemical analysis focused on the determination of the major cation (Na^+ , K^+ , Ca^{2+} , Sr^{2+} , Mg^{2+} , $\text{Fe}^{2+/3+}$, Al^{3+}) and anion (SO_4^{2-} , Cl^- , $\text{HCO}_3^-/\text{CO}_3^{2-}$, SiO_4^{4-}) concentrations.

5.5.1.1 Leaching of the powdered materials

The evolution of the chemical compositions of the leachates following the interaction of the fine powdered CIM_1, CIM_2_1 and CIM_2_6 materials was studied by means of batch sorption experiments designated P11, P21 and P26 respectively.

Fig. 18, Fig. 20 and Fig. 22 clearly show that sodium and potassium ions were detected only during the initial leaching step and that their concentrations in the subsequent leachates were below or close to the detection limit, thus indicating that all the soluble minerals or pore water residuals containing Na^+ and K^+ ions were dissolved during the first leaching step. The same results were observed for the SO_4^{2-} ions (see Fig. 19, Fig. 21 and Fig. 23). Cl^- ions were detected only in the initial leaching step of the P11 experiment; no chloride ions were detected in any of the other leachates. No iron presence was observed in the leachates at the beginning of the leaching process; however, increased iron concentrations were observed in the second half of the leaching tests. The slowest release of iron was observed in the P26 experiment (during the 7th and 8th leaching steps) compared to the P11 and P21 experiments, concerning which Fe leaching commenced during step 4. The concentrations of aluminium, SiO_3^{2-} and CO_3^{2-} were observed to be slightly decreased during the leaching test, a sharper decrease in calcium ions was observed in leaching steps 1 and 2, and further decreases were less pronounced with concern to all the materials studied (see Fig. 18, Fig. 19, Fig. 20, Fig. 21, Fig. 22 and Fig. 23). In general, lower concentrations of Ca^{2+} ions were detected in the leachates of the P26 experiment, whereas the opposite trend was observed concerning the Mg^{2+} ions, i.e. increased concentrations with respect to all three materials during leaching testing (see Fig. 18, Fig. 20 and Fig. 22). No NO_3^- ions were detected in the leachates.

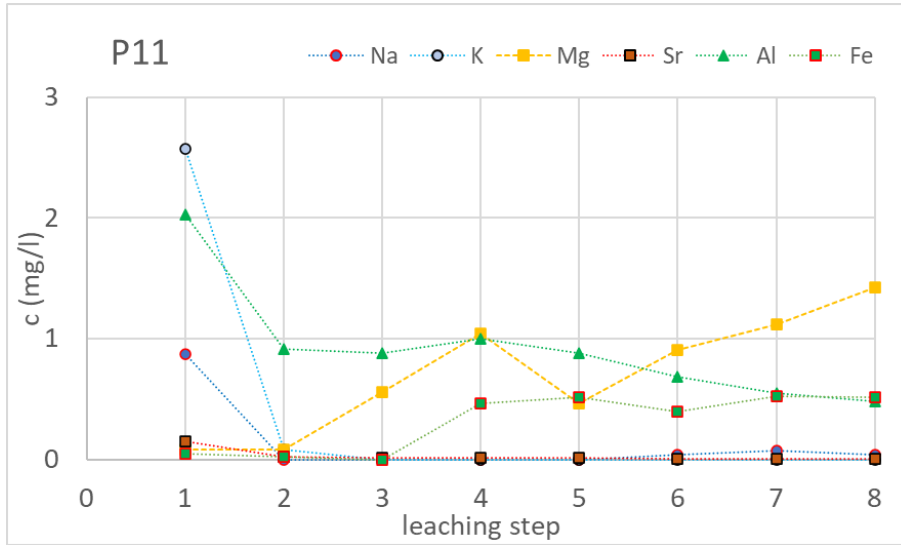


Fig. 18: Evolution of the Na⁺, K⁺, Mg²⁺, Sr²⁺ and Al_(tot) concentrations during the leaching of the CIM_1_1 powdered material into deionised water

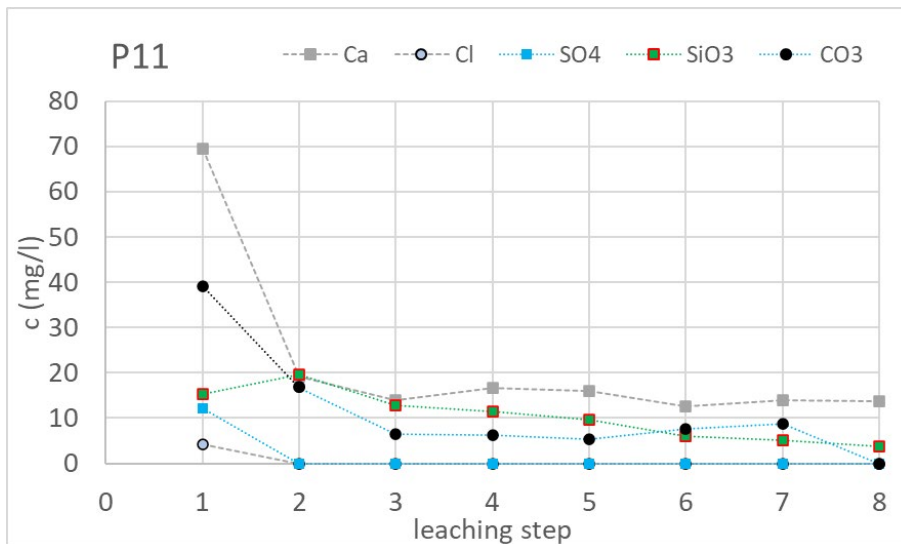


Fig. 19: Evolution of the Ca²⁺, Cl⁻, SO₄²⁻, SiO₃²⁻ and CO₃²⁻ concentrations during the leaching of the CIM_1_1 powdered material into deionised water

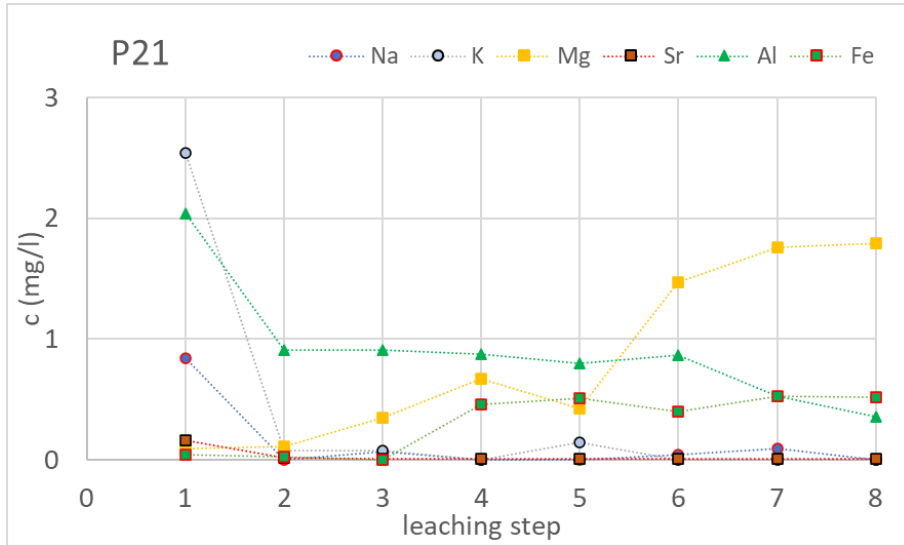


Fig. 20: Evolution of the Na⁺, K⁺, Mg²⁺, Sr²⁺ and Al_(tot) concentrations during the leaching of the CIM_2_1 powdered material into deionised water

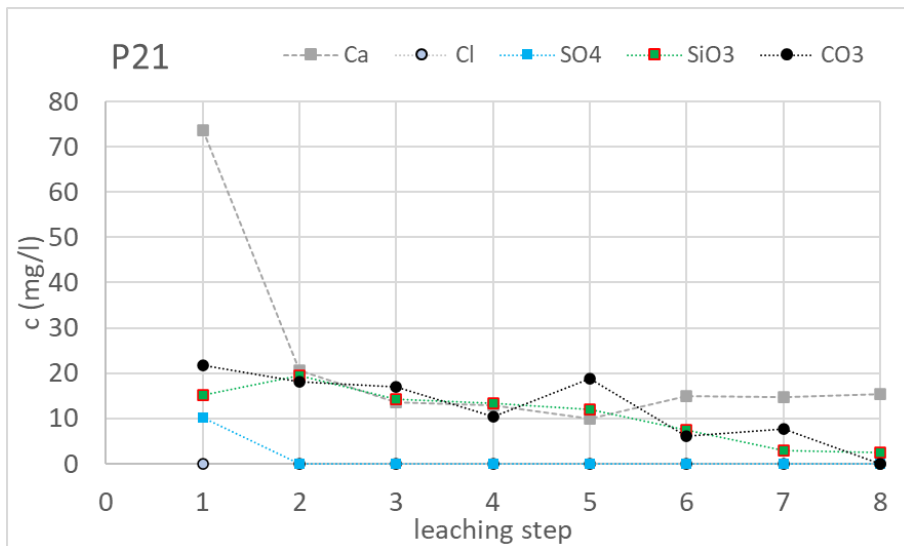


Fig. 21: Evolution of the Ca²⁺, Cl⁻, SO₄²⁻, SiO₃²⁻ and CO₃²⁻ concentrations during the leaching of the CIM_2_1 powdered material into deionised water

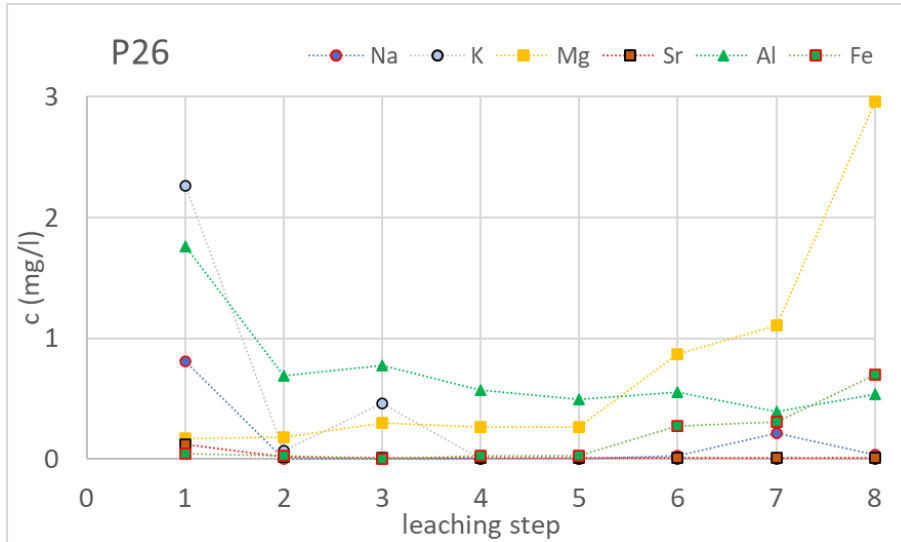


Fig. 22: Evolution of the Na^+ , K^+ , Mg^{2+} , Sr^{2+} and $\text{Al}_{(\text{tot})}$ concentrations during the leaching of the CIM_2_6 powdered material into deionised water

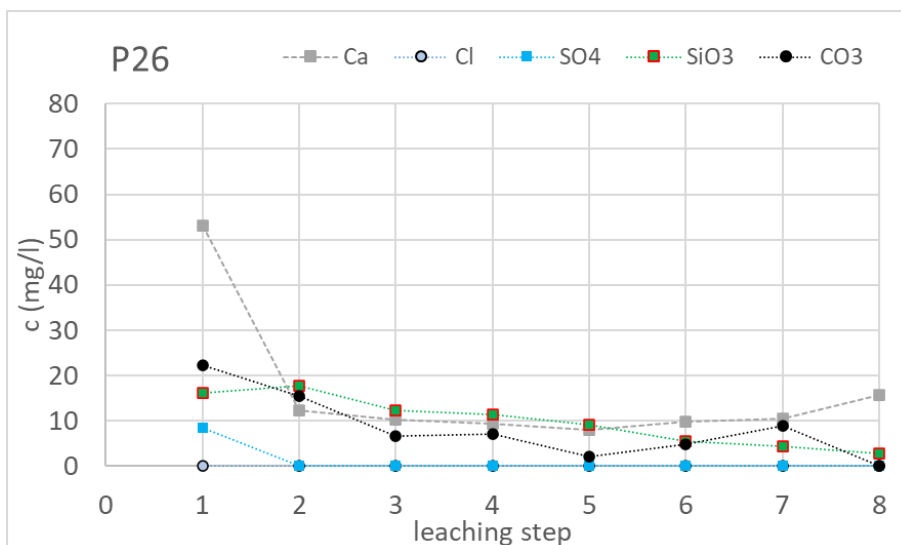


Fig. 23: Evolution of the Ca^{2+} , Cl^- , SO_4^{2-} , SiO_3^{2-} and CO_3^{2-} concentrations during the leaching of the CIM_2_6 powdered material into deionised water

5.5.1.2 Leaching of the coupons into deionised water

The evolution of the chemical composition of the leachates following the interaction of the CIM_1, CIM_2_1 and CIM_2_6 fine powdered materials was studied in batch sorption experiments designated 113B, 219B and 265B under anaerobic conditions in the glovebox and 113L, 219L and 265L under standard (aerobic) laboratory conditions, respectively.

Higher concentrations of Na^+ and K^+ ions were detected only in the initial and second leaching steps with respect to all the cases of the leaching of the coupon samples under aerobic and anaerobic conditions, and the concentrations in the subsequent leachates decreased to detection limit values as shown in Fig. 24, Fig. 25, Fig. 26, Fig. 27, Fig. 28 and Fig. 29. This indicated that all the soluble minerals and pore water residuals containing sodium and potassium ions were dissolved rapidly during the initial and second leaching steps. No Cl^- ,

NO_3^- and SO_4^{2-} ions were detected in the leachates. The concentrations of aluminium and Sr^{2+} detected in all the experiments during the leaching steps varied slightly in the value ranges of 0.7-1.0 and 0.1-0.3 for aluminium and strontium, respectively. Stable or slightly increasing SiO_3^{2-} ion concentration values were observed in the leachates under anaerobic conditions. The average SiO_3^{2-} concentration values for the 113B, 219B and 265B experiments varied in the ranges 4-7, 6-9 and 7-11 mg/l, respectively (see Fig. 24, Fig. 25 and Fig. 26), thus indicating that lower amounts of silicates were released/leached from the lower depth CIM_1 material. However, in the case of the laboratory experiments, decreasing trends in the values of the SiO_3^{2-} concentrations were observed (Fig. 27, Fig. 28 and Fig. 29). Although the Ca^{2+} and CO_3^{2-} concentrations decreased in all the leaching tests, the results differed for the anaerobic and aerobic conditions. Under the former conditions, the carbonate concentrations decreased slightly from 50 to 20 mg/l over the whole of the testing period compared to sharp decreases during leaching steps 1-4 to zero concentrations under the aerobic conditions (see Fig. 24, Fig. 25, Fig. 26, Fig. 27, Fig. 28 and Fig. 29). A similar trend was observed concerning the calcium ion concentration; in total, higher amounts of calcium were leached under the anaerobic conditions in the glovebox. This was probably due to the absence of carbon dioxide in the inert argon atmosphere in the glovebox and the differing equilibration processes of the inorganic carbon species in the solution under anaerobic and aerobic conditions.

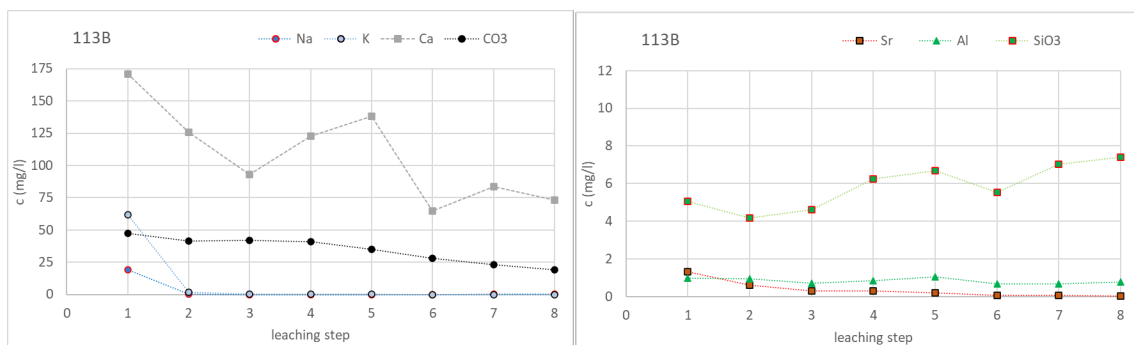


Fig. 24: Evolution of the liquid phase composition during the leaching of the CIM_1_1 coupons into deionised water under anaerobic conditions in the glovebox

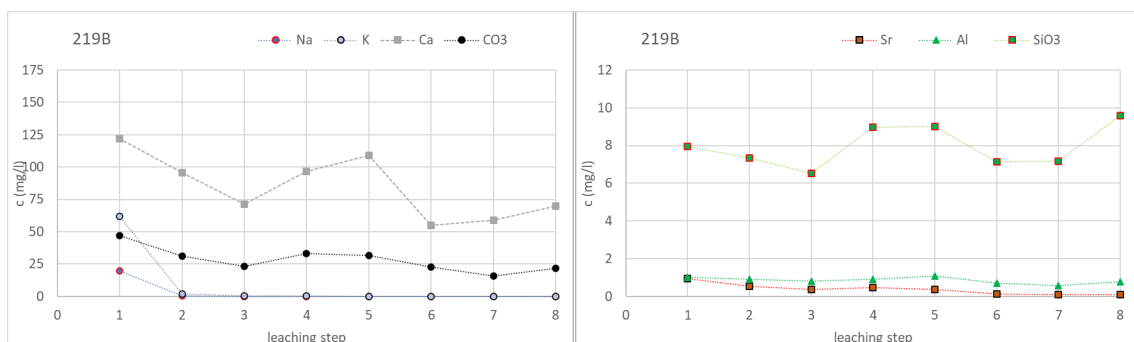


Fig. 25: Evolution of the liquid phase composition during the leaching of the CIM_2_1 coupons into deionised water under anaerobic conditions in the glovebox

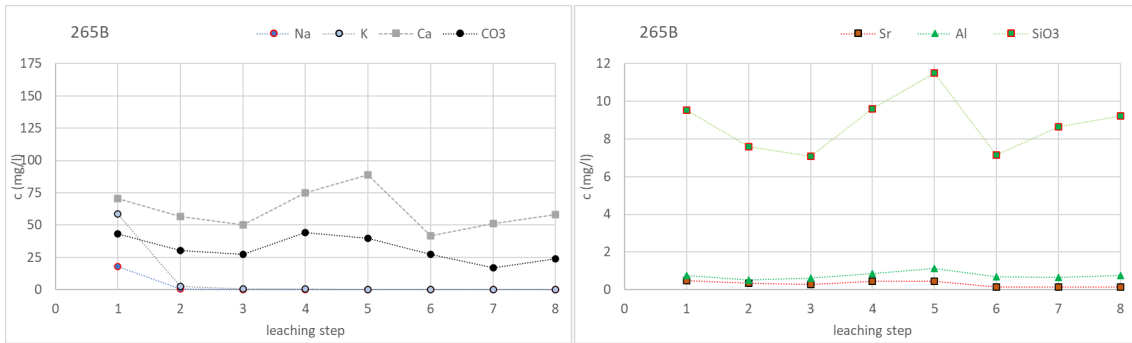


Fig. 26: Evolution of the liquid phase composition during the leaching of the CIM_2_6 coupons into deionised water under anaerobic conditions in the glovebox

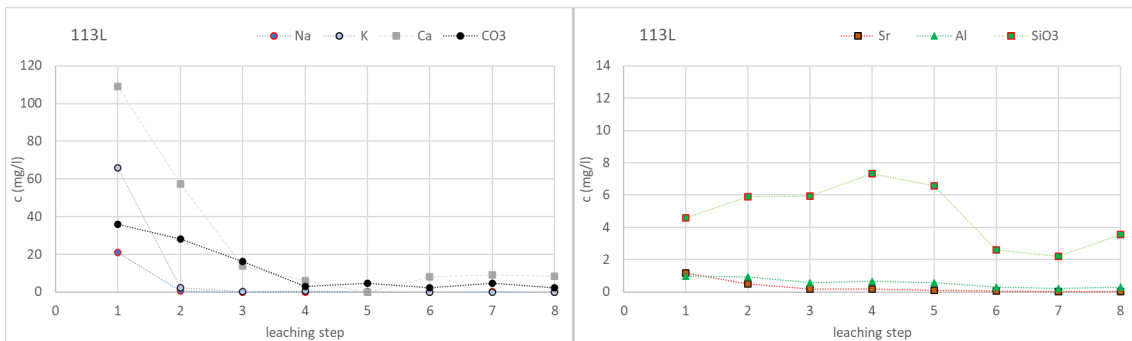


Fig. 27: Evolution of the liquid phase composition during the leaching of the CIM_1_1 coupons into deionised water under aerobic laboratory conditions

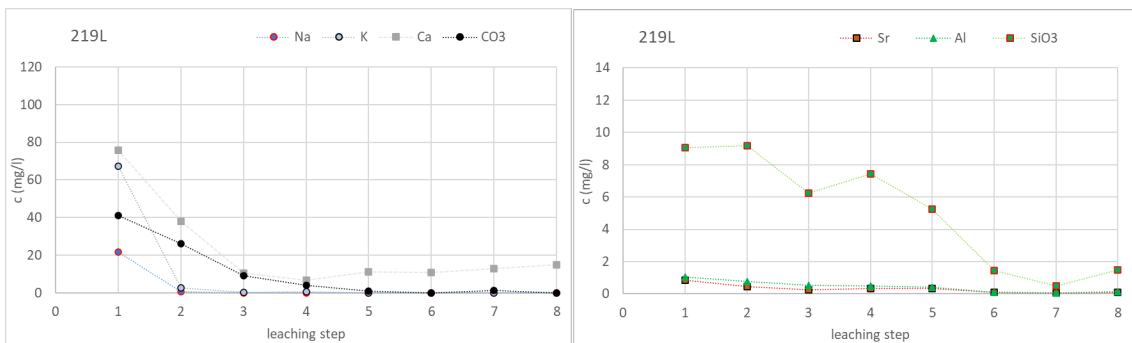


Fig. 28: Evolution of the liquid phase composition during the leaching of the CIM_2_1 coupons into deionised water under aerobic laboratory conditions

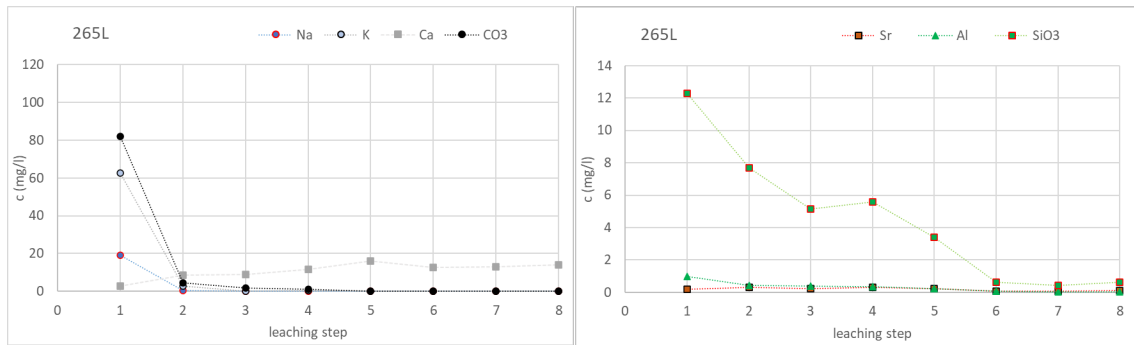


Fig. 29: Evolution of the liquid phase composition during the leaching of the CIM_2_6 coupons into deionised water under aerobic laboratory conditions

5.5.1.3 Leaching of the coupons into a saturated Ca(OH)₂ solution

The evolution of the chemical composition of the leachates following the interaction of the CIM_1_1 and CIM_2_1 fine powdered materials was studied in batch sorption experiments designated 115C and 211C. The leaching tests were performed under standard laboratory conditions.

The leaching test confirmed that the concentrations of Ca²⁺ ions were stable and varied only slightly due to interactions of the solution with air; the concentrations of the carbonates increased from leaching step 4 (see Fig. 31 and Fig. 33). The concentrations of Mg²⁺, Sr²⁺ and aluminium followed similar slightly decreasing trends with respect to both the materials. Varying behaviour was observed for the SiO₃²⁻ ion concentration; slightly decreasing values were observed in the CIM_1_1 material leachates, whereas a slight increase was observed in the case of the CIM_2_1 material (see Fig. 30 and Fig. 32).

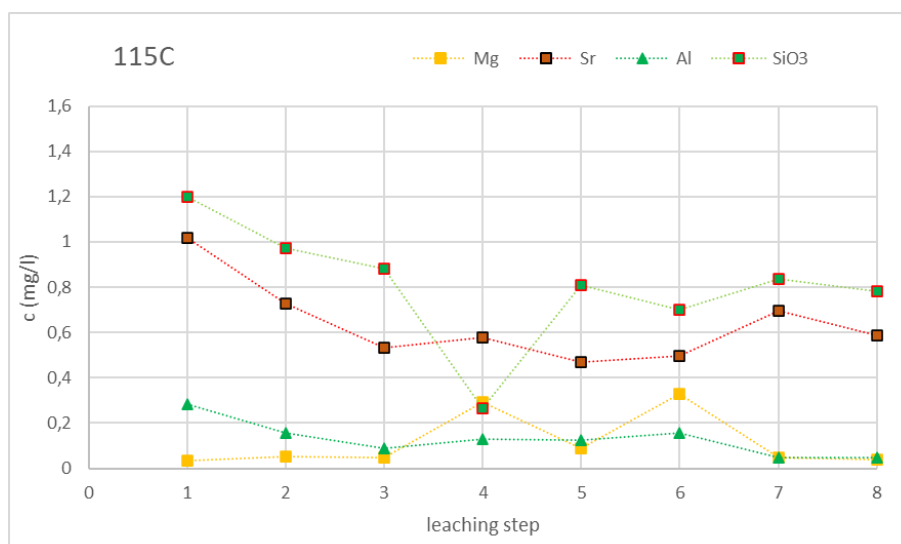


Fig. 30: Evolution of the Mg²⁺, Sr²⁺, aluminium and SiO₃²⁻ concentrations during the leaching of the CIM_1_1 coupon into the saturated Ca(OH)₂ solution

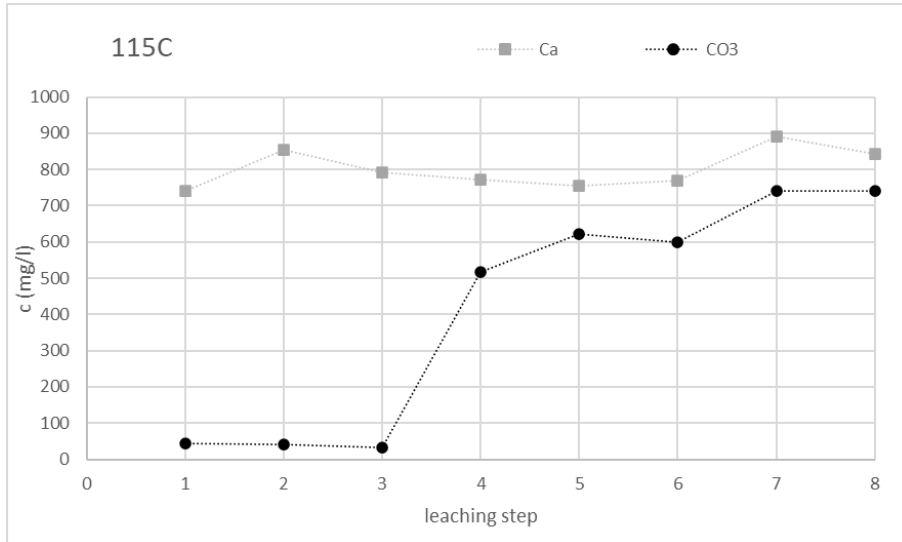


Fig. 31: Evolution of the Ca²⁺ and CO₃²⁻ concentrations during the leaching of the CIM_1_1 coupon into the saturated Ca(OH)₂ solution

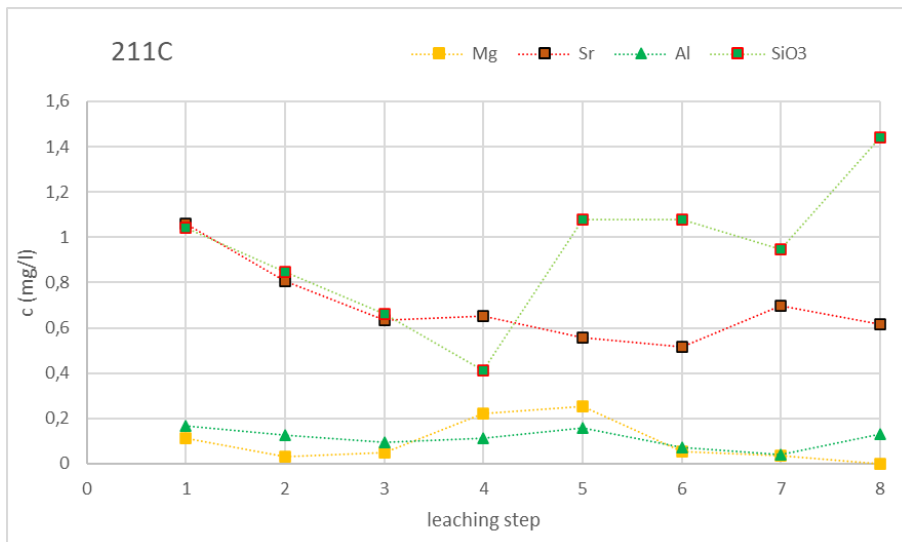


Fig. 32: Evolution of the Mg²⁺, Sr²⁺, aluminium and SiO₃²⁻ concentrations during the leaching of the CIM_2_1 coupon into the saturated Ca(OH)₂ solution

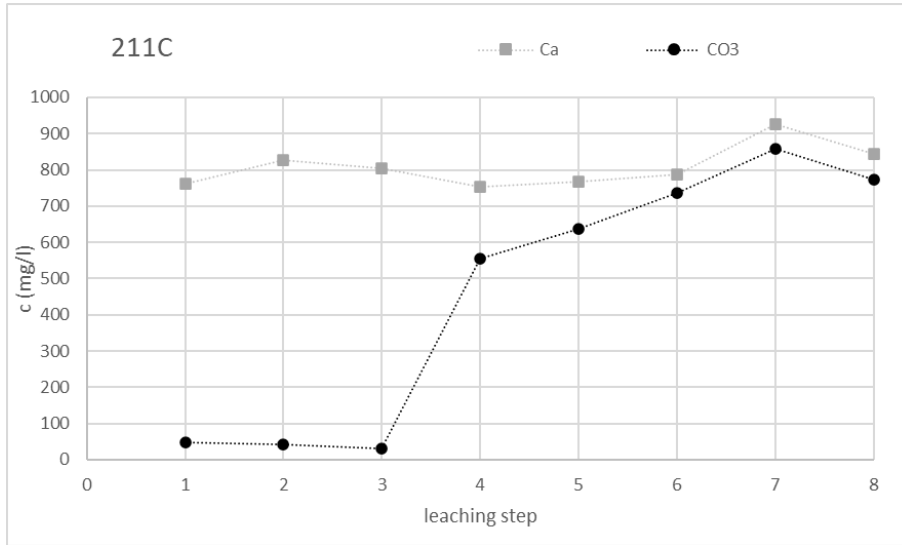


Fig. 33: Evolution of the Ca²⁺ and CO₃²⁻ concentrations during the leaching of the CIM_2_1 coupon into the saturated Ca(OH)₂ solution

5.5.2 Column interaction experiments – chemical analysis of the liquid phases

The chemical composition of the eluates following the interaction of the crushed CIM_1 and CIM_2 materials was subjected to analysis. The column interaction experiments were designated as follows:

K14A – column filled with crushed CIM_1 material, mesh size 0.5–1.0 mm,

K14B – column filled with crushed CIM_1 material, mesh size 1–2 mm,

K24A – column filled with crushed CIM_2 material, mesh size 0.5–1.0 mm,

K24B – column filled with crushed CIM_2 material, mesh size 1–2 mm.

The dominant changes in the concentrations of the analysed compounds were as follows: The same trends in the evolution of the concentration values were observed with concern to all four of the column experiment leachates. In the case of the calcium ions, the concentration values decreased sharply (from hundreds of mg/l to ~ 10 mg/l) with the passage of approximately 2 litres of water through the columns (see Fig. 34, Fig. 36 and Fig. 38). The dissolution of the portlandite comprised the first degradation process that occurred in the cementitious materials during this phase. Subsequently, the dissolution of ettringite was confirmed by the increased concentrations of SO_4^{2-} ions (see the peaks in the graphs shown in Fig. 35, Fig. 37 and Fig. 39). The concentrations of strontium ions, as a chemical analogue, followed the calcium ion trends. The dissolution of the portlandite was followed by the dissolution of the aluminates; a major proportion of the aluminates dissolved during the passage of approx. 4 litres of distilled water through the columns (see Fig. 34, Fig. 36 and Fig. 38). The final phase of interaction comprised the dissolution of silicates into the water; the dissolution process attained a stable ratio and a concentration of 30-35 mg/l in the eluate (see Fig. 35, Fig. 37 and Fig. 39).

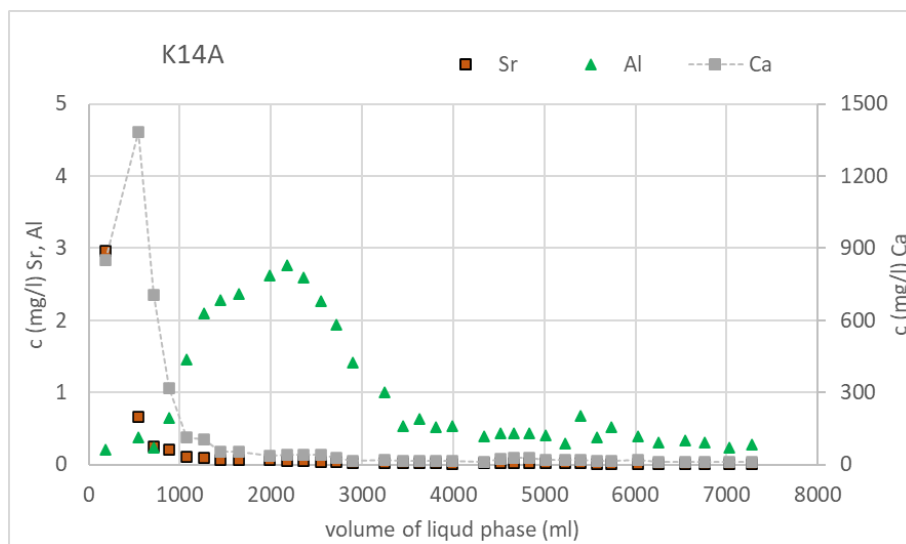


Fig. 34: Chemical composition (Sr^{2+} , Ca^{2+} , aluminium concentrations) of the output aqueous phase from column K14A

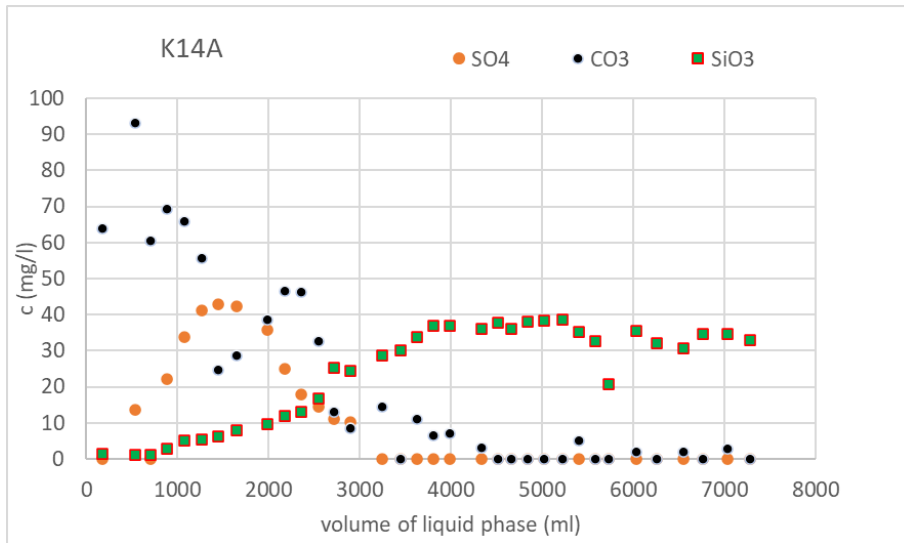


Fig. 35: Chemical composition (SO_4^{2-} , CO_3^{2-} and SiO_3^{2-} concentrations) of the output aqueous phase from column K14A

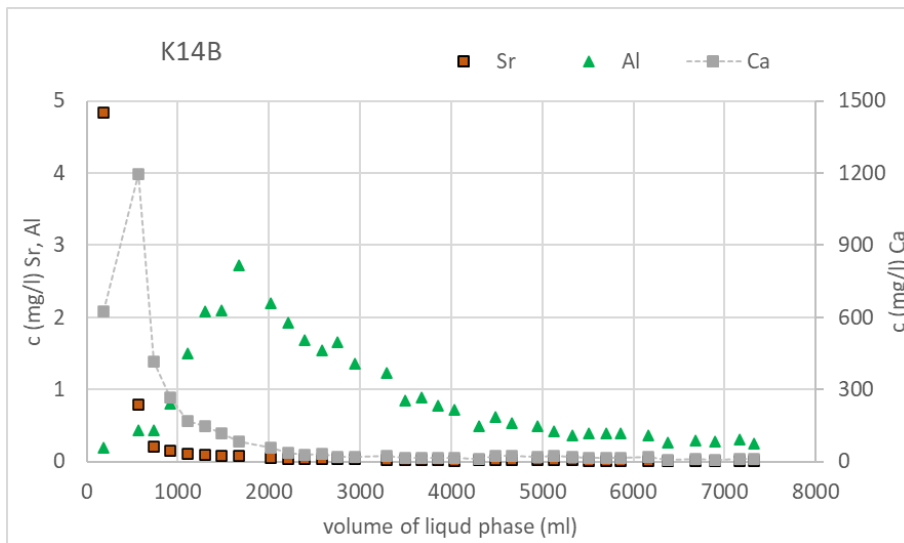


Fig. 36: Chemical composition (Sr^{2+} , Ca^{2+} , aluminium concentrations) of the output aqueous phase from column K14B

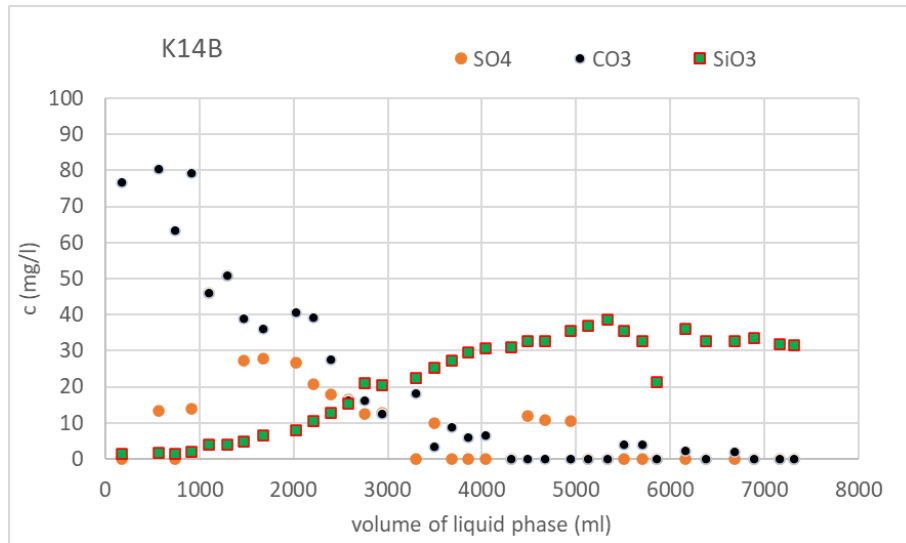


Fig. 37: Chemical composition (SO_4^{2-} , CO_3^{2-} and SiO_3^{2-} concentrations) of the output aqueous phase from column K14B

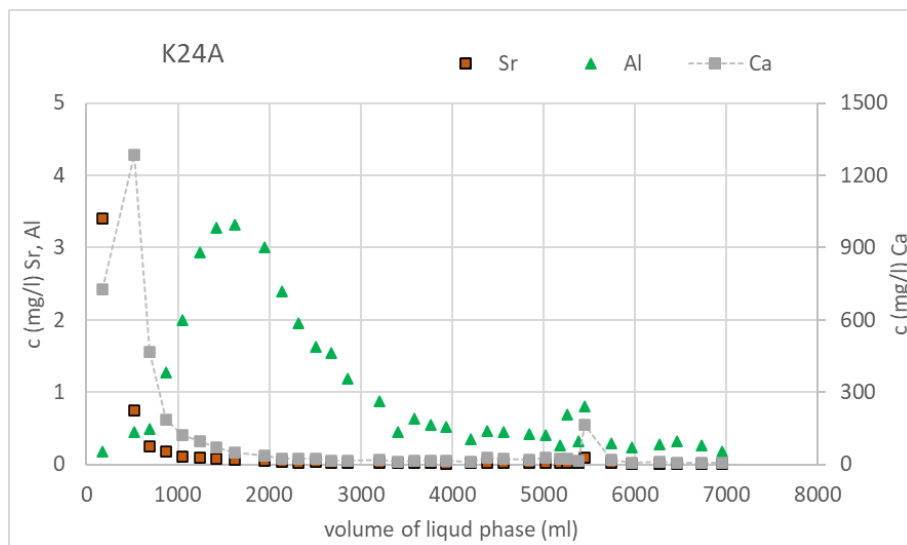


Fig. 38: Chemical composition (Sr^{2+} , Ca^{2+} , aluminium concentrations) of the output aqueous phase from column K24A

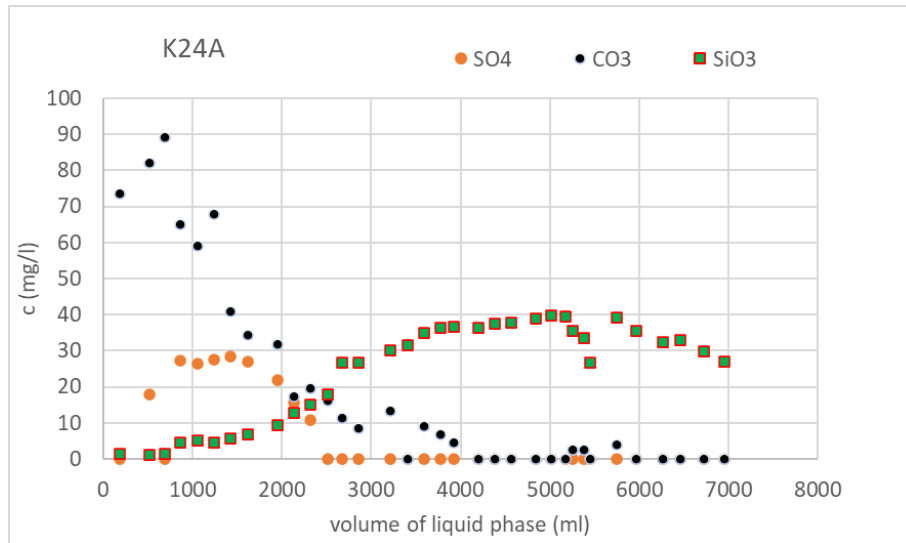


Fig. 39: Chemical composition (SO_4^{2-} , CO_3^{2-} and SiO_3^{2-} concentrations) of the output aqueous phase from column K24A

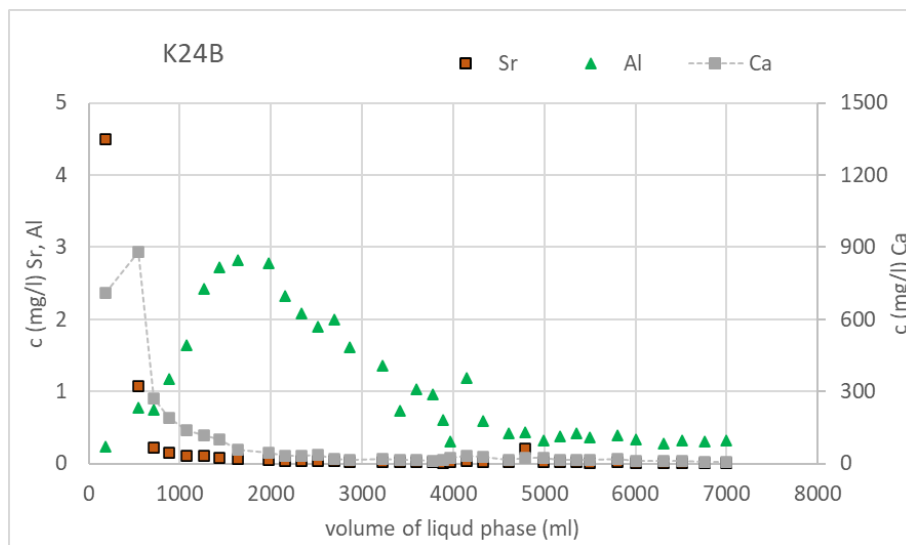


Fig. 40: Chemical composition (Sr^{2+} , Ca^{2+} , aluminium concentrations) of the output aqueous phase from column K24B

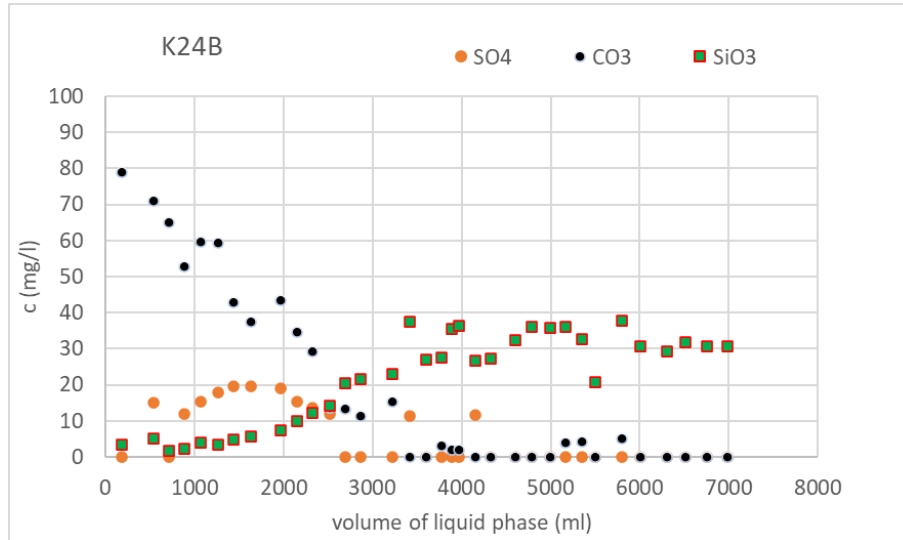


Fig. 41: Chemical composition (SO_4^{2-} , CO_3^{2-} and SiO_3^{2-} concentrations) of the output aqueous phase from column K24B

5.6 Sorption experiment results

5.6.1 ^{125}I tracer sorption

The sorption experiments with the $^{125}\text{I}^-$ tracer with two initial carrier concentrations were performed under standard laboratory conditions on the CIM_1 and CIM_2 materials. The graphs in Fig. 42 provide a comparison of the two CIM materials and the results obtained previously for the CEM II/A-S 42.5 R hardened cement paste as published in Večerník et al. (2019b) for the $^{125}\text{I}^-$ tracer and two initial carrier concentrations. Although the CIM_1 and CIM_2 materials evinced similar R_d values, the value was slightly higher with respect to the material taken from the deeper borehole core (CIM_2) for the experiment with the lower carrier concentration. However, compared to the CEM II/A-S 42.5 R material, the distribution coefficients of the CIM samples were significantly lower, which was probably due to the long duration of the contact between the CIM materials and the groundwater at the Grimsel Test Site and which, in turn, resulted in the potential dissolution of the reactive components.

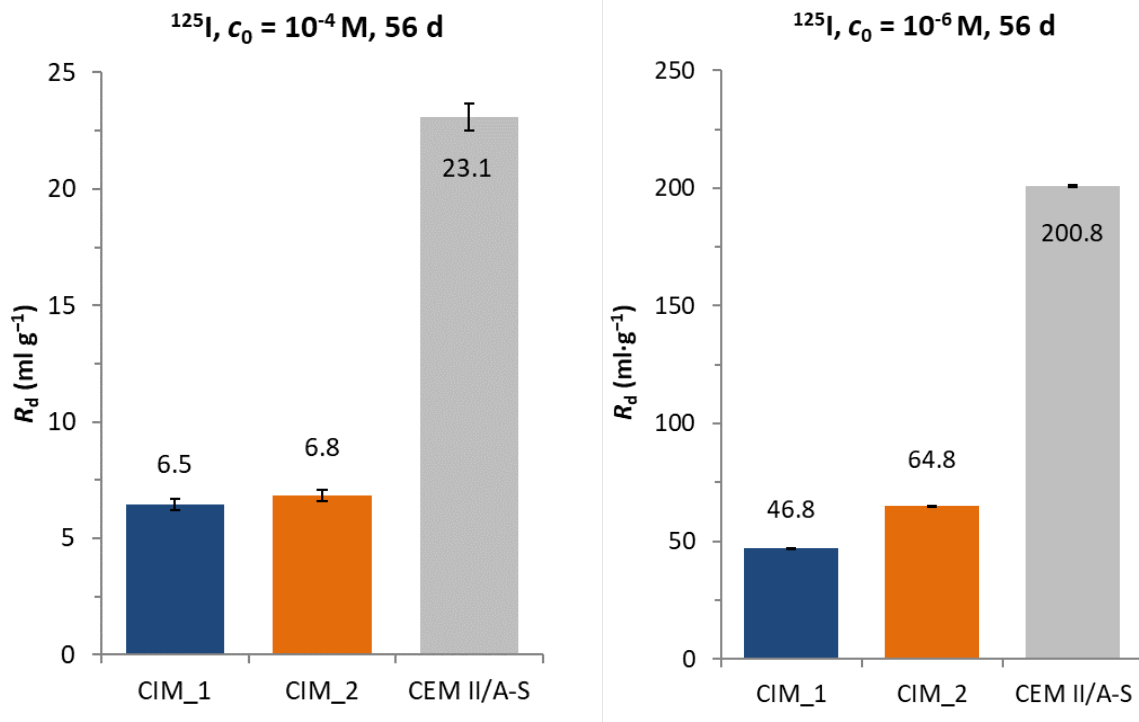


Fig. 42: R_d distribution coefficients for ^{125}I

5.6.2 ^{14}C tracer sorption

The ^{14}C tracer in the form of acetate was employed in the first set of diffusion experiments. The graph in Fig. 43 illustrates the results of the sorption experiments with ^{14}C acetate under standard laboratory conditions on the CIM_1 and CIM_2 materials. It is clear that only very small amounts of acetate were sorbed on the two CIM materials, practically independently of the type of material and the initial carrier concentration. These results corresponded well with those of previous experiments on CEM II/A-S 42.5 R hardened cement paste published in Večerník et al. (2019a).

The second set of experiments studied the influences of the organic carbon speciation ($\text{H}^{14}\text{COONa}$, $\text{CH}_3^{14}\text{COONa}$), the material (CIM_1, CIM_2, CEM I) and the particle size (2-3 fractions from <0.25 to 2.0 mm) on sorption under aerobic/anaerobic conditions. The experiments were performed over a period of 56 days.

Since the effect of particle size did not prove to be statistically significant for the mesh size fractions used in the experiments (see Fig. 44), the results obtained for particle sizes of 0.25 – 1.00 mm (CIM materials) and 0.5 – 1.0 mm (CEM I) were selected for further comparison.

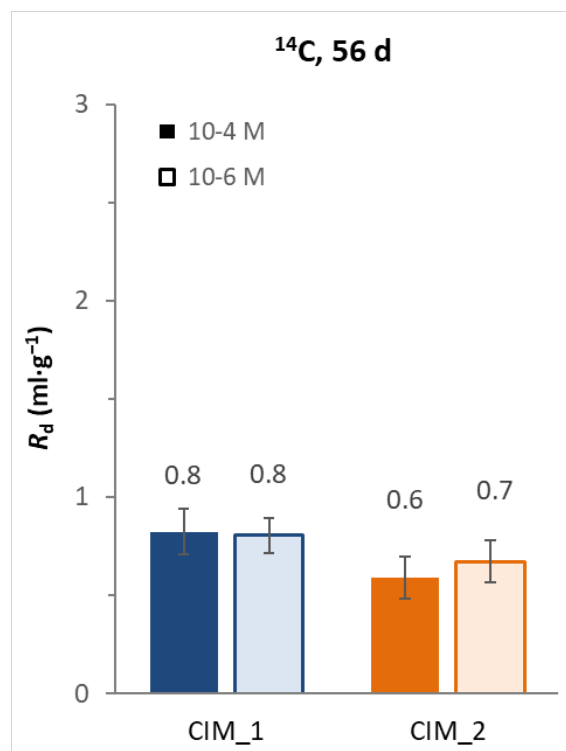


Fig. 43: R_d distribution coefficients for ^{14}C acetate

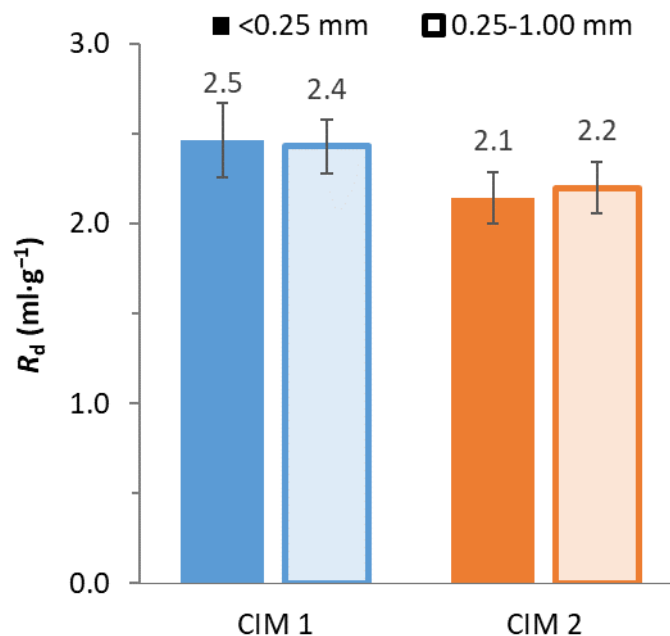


Fig. 44: Comparison of the effect of the sample particle size (^{14}C formate tracer, aerobic conditions, 56 days of experimentation)

As previously described in other publications (Matsumoto et al., 1994) and demonstrated via previous experiments (Brázda et al. 2019; Večerník et al. 2017; Večerník et al. 2019), organic forms of carbon sorb on cement in a given environment only in small amounts, the extent of which depends on the size, chemical structure and polarity of the organic molecules.

The resulting values of R_d in the studied systems using formate ($pK_a = 3.74$, $\log P = -0.54$; Sangster 1989) as the tracer were approximately four times higher than the R_d values determined for acetate ($pK_a = 4.76$, $\log P = -0.17$; Sangster 1989) as shown in Fig. 45. However, even after 56 days, the R_d value did not exceed $2.5 \text{ ml}\cdot\text{g}^{-1}$. In comparison, the distribution coefficient presented in a study of the acetate sorption on CEM II with a particle size of 0.1-0.5 mm (carrier concentration of $0.1 \text{ mol}\cdot\text{l}^{-1}$, phase ratio 1:10) attained a value of approximately $3 \text{ ml}\cdot\text{g}^{-1}$ after 7 days. However, other experiments determined significantly lower values after 7 days ($< 0.4 \text{ ml}\cdot\text{g}^{-1}$, Večerník et al. 2019a).

Furthermore, it has been shown that while the CIM_1 and CIM_2 materials evince very similar sorption properties, all the conditions of the CIM_1 material (drill core from a lesser depth) R_d appear to be slightly higher, probably due to the higher content of components that interact with the tracers. The results of previous experiments suggest a similar conclusion (Brázda et al. 2019).

The influence of the atmosphere (especially the presence of CO_2 and O_2) on the results of the experiments was not very significant; however, it seems that the R_d is lower under anaerobic conditions. As can be seen from Fig. 46, the difference is evident in the case of the CEM I material; in the case of the CIM_1 and CIM_2 materials, however, the difference is statistically insignificant.

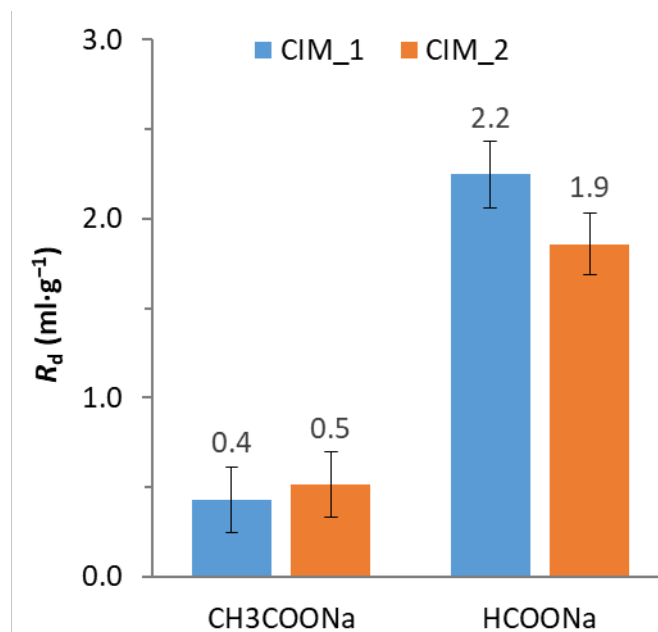


Fig. 45: Comparison of the influence of the tracer selection (conditions: fraction 0.25–1.00 mm, anaerobic, after 56 days of the experiment)

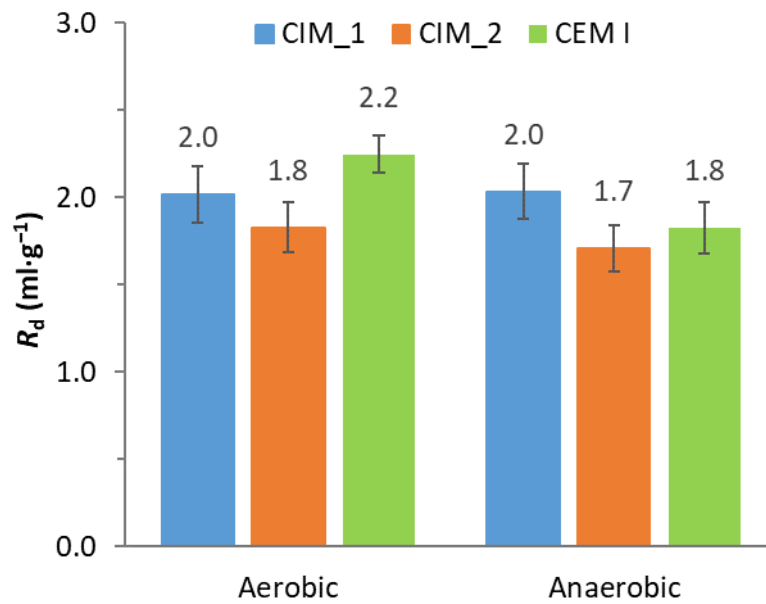


Fig. 46: Comparison of the effect of aerobic/anaerobic conditions (conditions: $H^{14}COONa$ tracer, fraction 0.25–1.00 mm (CIM) or 0.5–1.0 mm (CEM I), after 7 days of experimentation)

It can be seen from the visual representation of the dependence of the R_d on time (Fig. 47, Fig. 48) that after 28–56 days the systems with the formate tracer approached equilibrium. As shown in Fig. 49, the results for the systems that employed acetate are subject to a relatively high degree of uncertainty due to the very low R_d values. These values are slightly lower than the distribution coefficients presented in a study on acetate sorption on the same CIM materials (particle size 0.25–1.00 mm, carrier concentration $10^{-6} \text{ mol}\cdot\text{l}^{-1}$, phase ratio $m:V$ 1:10), where the values reached $0.8 \pm 0.1 \text{ ml}\cdot\text{g}^{-1}$ for the CIM_1 and $0.7 \pm 0.1 \text{ ml}\cdot\text{g}^{-1}$ for the CIM_2 materials after 56 days (Brázda et al. 2019).

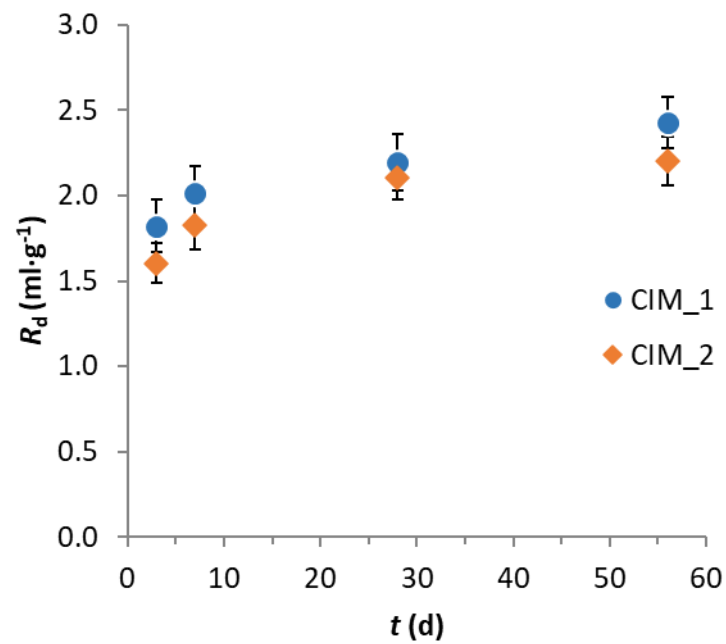


Fig. 47: Dependence of the R_d on time (conditions: $H^{14}COONa$ tracer, aerobic conditions, fraction 0.25–1.00 mm, after 56 days of experimentation)

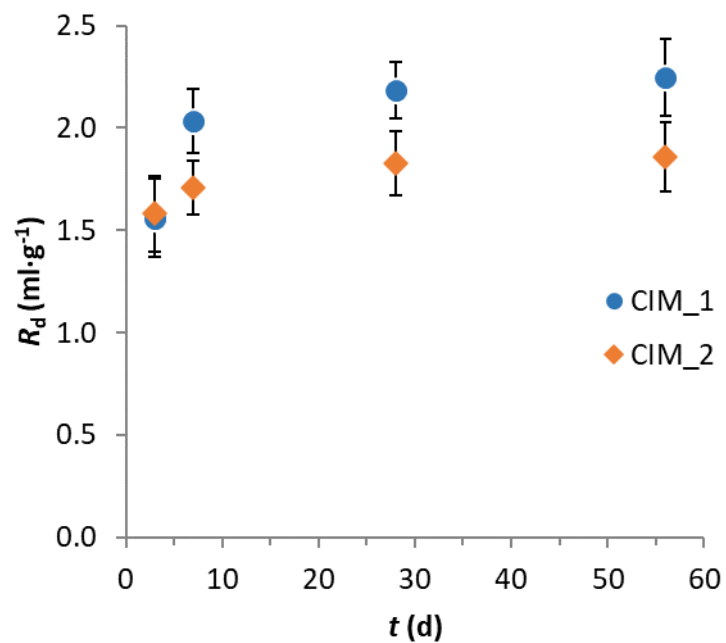


Fig. 48: Dependence of the R_d on time (conditions: $H^{14}COONa$ tracer, anaerobic conditions, fraction 0.25–1.00 mm, after 56 days of experimentation)

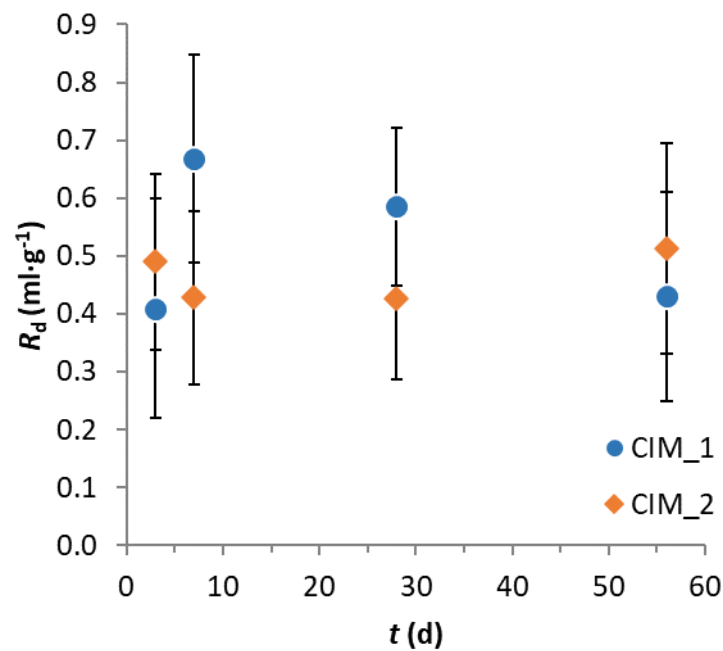


Fig. 49: Dependence of the R_d on time (conditions: $\text{CH}_3^{14}\text{COONa}$ tracer, anaerobic conditions, fraction 0.25–1.00 mm, after 56 days of experimentation)

The overall measurement results, including the distribution coefficients and the sorption yields for fractions 0.25–1.00 mm (the CIM materials) and 0.5–1.0 mm (the CEM I paste) are summarised in Tab. 8 and Tab. 9.

Tab. 8: R_d distribution coefficients for the ^{14}C tracers (aerobic and anaerobic conditions, mesh size fractions 0.25–1.00 mm (CIM) and 0.5–1.0 mm (CEM I))

t (day)	Conditions	$R_d \pm U(y)$ (ml·g ⁻¹)		
		CIM_1	CIM_2	CEM I
3	$\text{H}^{14}\text{COONa}$, aerobic	1.8 ± 0.2	1.6 ± 0.1	
	$\text{H}^{14}\text{COONa}$, anaerobic	1.6 ± 0.2	1.6 ± 0.2	
	$\text{CH}_3^{14}\text{COONa}$, anaerobic	0.4 ± 0.2	0.5 ± 0.2	
7	$\text{H}^{14}\text{COONa}$, aerobic	2.0 ± 0.2	1.8 ± 0.1	2.2 ± 0.1
	$\text{H}^{14}\text{COONa}$, anaerobic	2.0 ± 0.2	1.7 ± 0.1	1.8 ± 0.1
	$\text{CH}_3^{14}\text{COONa}$, anaerobic	0.7 ± 0.2	0.4 ± 0.1	0.4 ± 0.1
28	$\text{H}^{14}\text{COONa}$, aerobic	2.2 ± 0.2	2.1 ± 0.1	
	$\text{H}^{14}\text{COONa}$, anaerobic	2.2 ± 0.1	1.8 ± 0.2	
	$\text{CH}_3^{14}\text{COONa}$, anaerobic	0.6 ± 0.1	0.4 ± 0.1	
56	$\text{H}^{14}\text{COONa}$, aerobic	2.4 ± 0.1	2.2 ± 0.1	
	$\text{H}^{14}\text{COONa}$, anaerobic	2.2 ± 0.2	1.9 ± 0.2	
	$\text{CH}_3^{14}\text{COONa}$, anaerobic	0.4 ± 0.2	0.5 ± 0.2	

 SÚRAO	Migration of Carbon and Iodine in Cementitious Matrix – Final Report	Registration number:
		538/2021

Tab. 9: Sorption yields for the ^{14}C tracers (aerobic/anaerobic conditions, mesh size fractions 0.25–1.00 mm (CIM) and 0.5–1.0 mm (CEM I))

t (day)	Conditions	$\eta \pm U(y)$ (%)		
		CIM_1	CIM_2	CEM I
3	$\text{H}^{14}\text{COONa}$, aerobic	12.2 ± 0.9	11.6 ± 0.8	
	$\text{H}^{14}\text{COONa}$, anaerobic	10.7 ± 1.2	11.5 ± 1.2	
	$\text{CH}_3^{14}\text{COONa}$, anaerobic	3.0 ± 1.4	3.9 ± 1.2	
7	$\text{H}^{14}\text{COONa}$, aerobic	13.4 ± 0.9	13.0 ± 0.9	18.4 ± 0.7
	$\text{H}^{14}\text{COONa}$, anaerobic	13.5 ± 0.9	12.3 ± 0.8	15.4 ± 1.0
	$\text{CH}_3^{14}\text{COONa}$, anaerobic	4.9 ± 1.2	3.4 ± 1.1	4.0 ± 0.8
28	$\text{H}^{14}\text{COONa}$, aerobic	14.4 ± 0.9	14.7 ± 0.8	
	$\text{H}^{14}\text{COONa}$, anaerobic	14.3 ± 0.8	13.1 ± 1.0	
	$\text{CH}_3^{14}\text{COONa}$, anaerobic	4.3 ± 1.0	3.4 ± 1.1	
56	$\text{H}^{14}\text{COONa}$, aerobic	15.7 ± 0.8	15.3 ± 0.8	
	$\text{H}^{14}\text{COONa}$, anaerobic	14.7 ± 1.0	13.2 ± 1.1	
	$\text{CH}_3^{14}\text{COONa}$, anaerobic	3.2 ± 1.3	4.0 ± 1.4	

5.7 Diffusion experiment results

The effective diffusion coefficient (D_e) values for the HTO and ^{14}C tracers were obtained by fitting the experimental data to the analytical solution equation. The ^{125}I tracer was evaluated via the time-lag method due to the long time period between the beginning of the experiment and the detection of the tracer in the outlet reservoir (see Fig. 50), which resulted in difficulties in terms of fitting the experimental data to the analytical solution equation.

It was confirmed that the highest diffusion velocity was evinced by the ^3H tracer (in the form of HTO) as a conservative tracer. The ^{125}I tracer (in the form of iodide) interacted with the cementitious material, which caused retardation and a delay in the breakthrough curve (shifting of the linear part of the curve). The migration behaviour of the studied organic carbon tracers (acetate, formate) can be considered practically the same if the heterogeneity of the cement material samples is taken into account.

The first set of diffusion experiments employing HTO, ^{14}C acetate and ^{125}I iodide tracers was performed under standard laboratory conditions on materials extracted from three different depths. The second set of diffusion tests was performed using a ^{14}C formate tracer under both standard laboratory conditions and under the anaerobic conditions of the glovebox.

As can be seen from Fig. 50, the various tracers migrated through the samples at different velocities, and the time required to detect the tracer in the outlet reservoir varied substantially. Once the diffusion flux turned constant, the experimental points could be fitted to the linear regression. The $t_{n=0}$ parameter is obtained by extrapolating this dependence to $A/A_0 = 0$ (i.e.

the intersection with the x axis). The higher the value, the longer the time required for the tracer to diffuse through the sample. The $t_{n=0}$ values obtained are shown in graph form in Fig. 51.

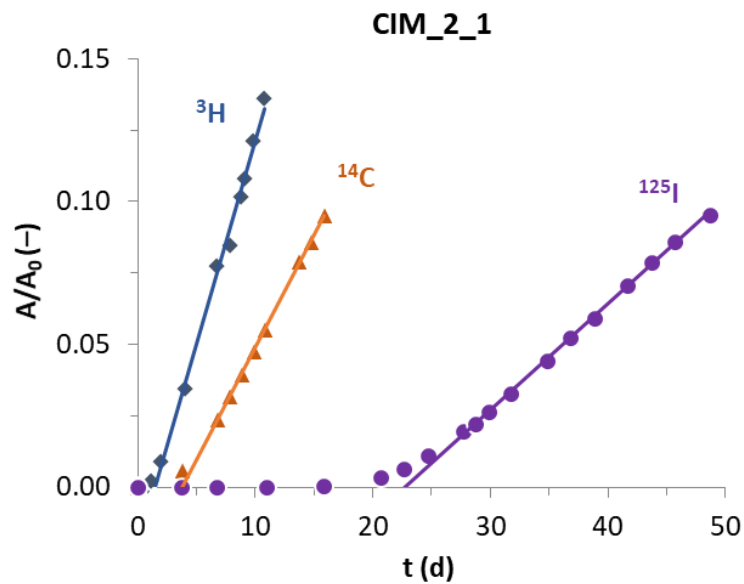


Fig. 50: Example of the breakthrough curves of the HTO, acetate and iodide tracers (CIM_2_1 material, aerobic conditions)

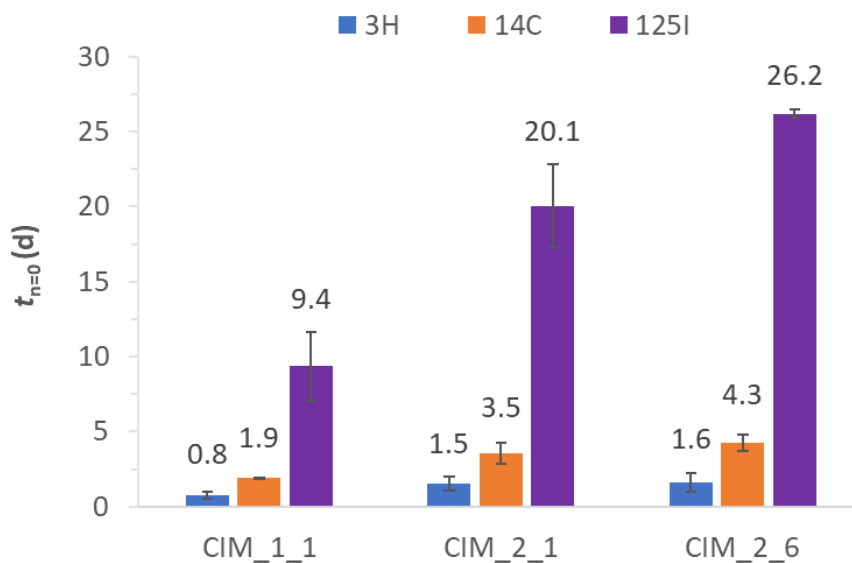


Fig. 51: Comparison of the $t_{n=0}$ parameter for the HTO, acetate and iodide tracers and materials

The results obtained from the diffusion experiments using the ^{14}C formate tracer and performed under both aerobic and anaerobic conditions were compared to the results of previous diffusion experiments (Brázda et al., 2019) performed under aerobic conditions; the results are summarised in Tab. 10.

A comparison of the D_e values determined from the experiments performed under aerobic conditions is presented in Fig. 52. A clear correlation is evident between the D_e values of the

three tracers and the average depth at which the HCP core was drilled. The highest values were observed with respect to the non-sorbing HTO tracer, whereas around two times lower values were determined for the ^{14}C tracer and even lower D_e values were recorded in the case of the ^{125}I tracer. The differences in the diffusion behaviour of the tracers were probably due to the sorption and/or anion exclusion of the ^{14}C and ^{125}I anions.

No significant differences were evident between the behaviour of the ^{14}C acetate and ^{14}C formate tracers under laboratory conditions (see Fig. 52). The same applied to the effective diffusion coefficient values of the ^{14}C formate tracer determined from the experiments performed under the laboratory aerobic and glovebox anaerobic conditions (see Fig. 53).

Tab. 10: Comparison of the effective diffusion coefficient values

$D_e \text{ (m}^2/\text{s)} \times 10^{-11}$	CIM_1_1	CIM_2_1	CIM_2_6
^3H (LAB)	(11.3 ± 2.1)	(5.8 ± 1.6)	(3.6 ± 0.2)
^{14}C -acetate (LAB)	(6.3 ± 0.9)	(3.2 ± 1.1)	(2.1 ± 0.1)
^{125}I (LAB)	(3.5 ± 1.3)	(1.5 ± 0.6)	(1.3 ± 0.6)
^{14}C -formate (LAB)	(6.5 ± 0.15)	(3.76 ± 0.48)	(2.54 ± 0.25)
^{14}C -formate (BOX)	(7.52 ± 2.1)	(3.98 ± 0.72)	(2.67 ± 0.7)

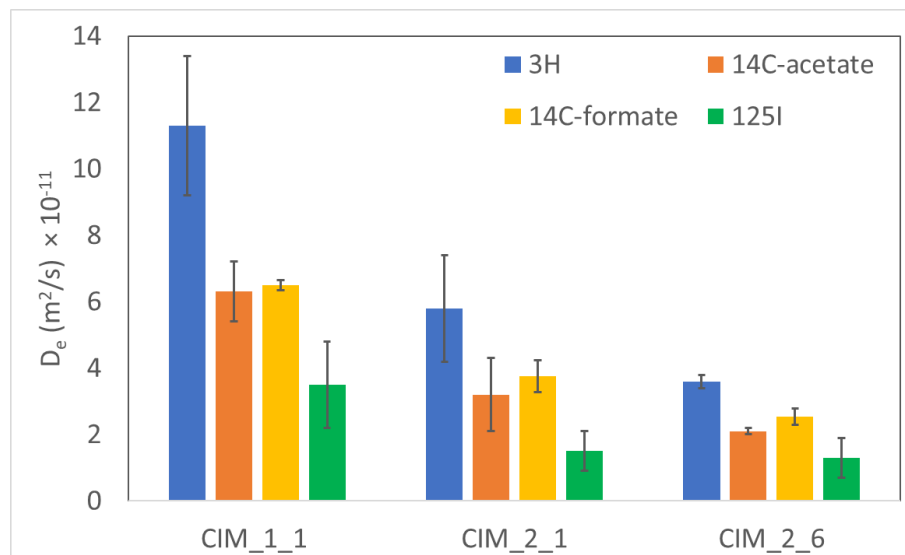


Fig. 52: Effective diffusion coefficient values of the studied tracers under aerobic conditions

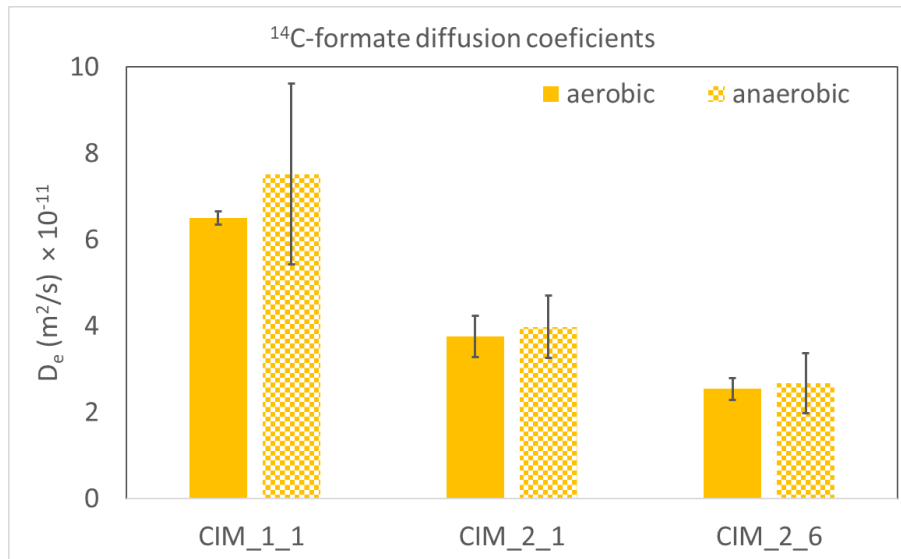


Fig. 53: Comparison of the effective diffusion coefficient values of the ¹⁴C-formate tracer under aerobic and anaerobic conditions

5.8 Analysis of the solid phases following the leaching/interaction experiments

The thermogravimetry measurements described the following processes: At temperatures of up to 200°C, water is released from ettringite and hydrated calcium silicates. At temperatures of up to around 400°C, other thermally less stable components (especially H₂O and CO₂) are released. The decomposition of hydrotalcite and hemicarboaluminate occurs at a maximum temperature of around 400°C, while portlandite (if present in the samples) decomposes at temperatures of around 480°C. Up to temperatures of around 700°C, CO₂ and SO₂ are released from carbonates and sulphates. Above a temperature of 700°C, dolomite begins to decompose, followed by the decomposition of calcite at 820°C. The ratio of dolomite and calcite, which decompose in this complex process, cannot be accurately determined. The final event at 900°C concerns the evolution of SO₂.

The thermal decomposition of dolomite takes place in two stages. Firstly CO₂ is released from the dolomite within a temperature range centred at around 700°C according to the reaction $CaMg(CO_3)_2 \rightarrow MgO + CO_2 + CaCO_3$ (maximum temperature of around 750°C). The second stage in the decomposition of dolomite ($CaCO_3 \rightarrow CaO + CO_2$) coincides with the decomposition of calcite. According to the literature, the maximum temperature at which this process occurs is around 820-830°C. Therefore, it is not always easy to estimate the mass fractions of the two crystalline phases. However, it is generally sufficient to express this process as the weight loss of CO₂.

No estimation of the amorphous phases that may accompany the crystalline phases in these types of sample was performed via XDR analysis due to the limited numbers of samples.

 SÚRAO	Migration of Carbon and Iodine in Cementitious Matrix – Final Report	Registration number:
		538/2021

5.8.1 Solid phases following leaching

5.8.1.1 XRD and TGA of the crushed materials

Examples of the TGA graph and XRD pattern of the CIM BC12A1 crushed material are shown in Fig. 54 and Fig. 55. The decomposition of the mineral phases is clearly illustrated by the TGA graph. The composition of the dominant crystalline mineral phases is presented in Tab. 11 and a comparison of the initial and leached materials is presented in Fig. 56. All the XRD patterns and TGA graphs of the leached crushed materials are presented in the Appendix (Fig. 72 - Fig. 79) .

The results show that in the case of the CIM_1 material (experiments BC12A1 and BC12AN1), the calcite and ettringite weight ratios increased, the ratios of dolomite and quartz remained approx. stable and the ratios of the portlandite and CSH phases decreased (these phases dissolved) in the leached materials compared to the initial materials under both aerobic and anaerobic conditions.

In the case of the CIM_2 material (experiments BC22A2 and BC22AN2), the dolomite and quartz weight ratios increased while the ratios of the calcite, ettringite, portlandite, katoite and CSH phases decreased (these phases dissolved) in the leached materials compared to the initial materials under both aerobic and anaerobic conditions.

These results confirmed the differing behaviour of the crushed CIM materials extracted from the various depths during the process of leaching into a calcium hydroxide solution due to the varying degrees of heterogeneity of the studied cementitious materials.

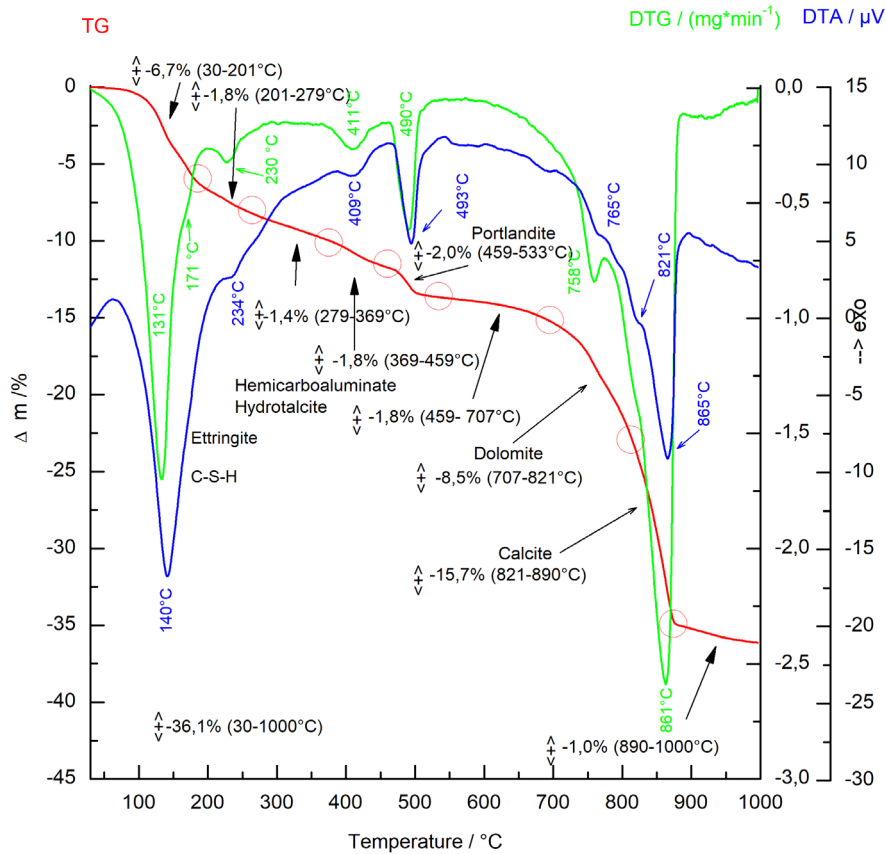


Fig. 54: TGA analysis of the BC12A1 material

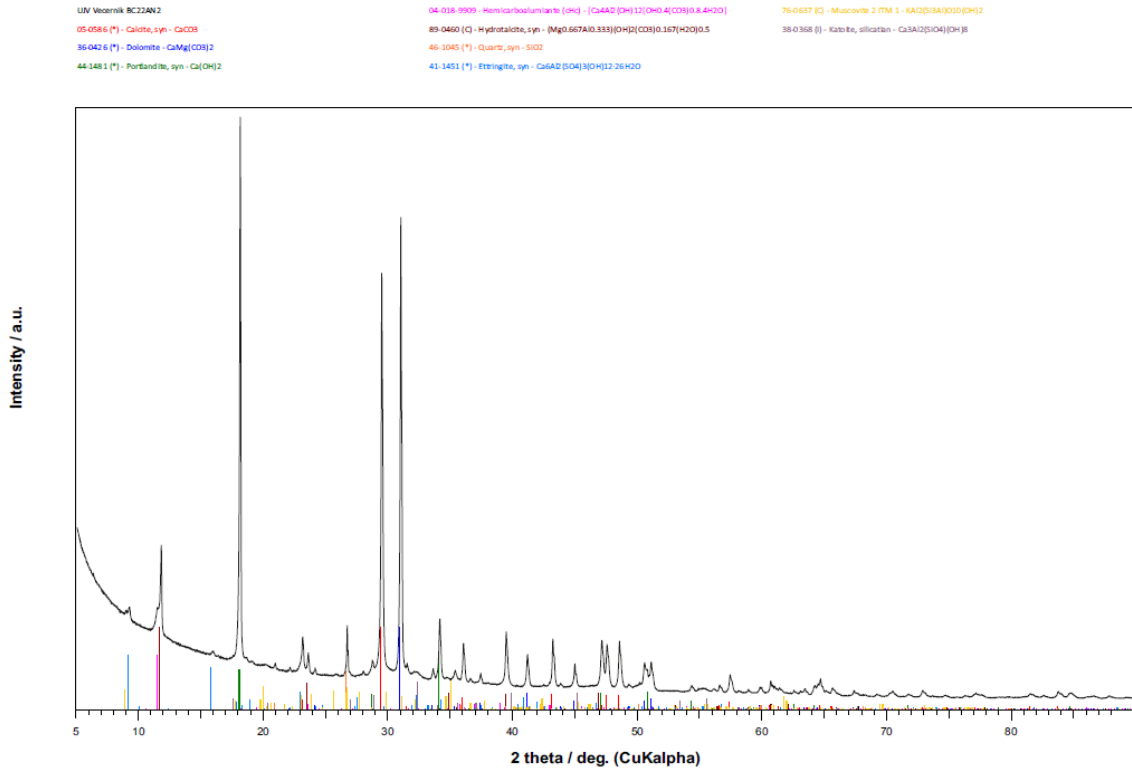


Fig. 55: XRD pattern of the BC12A1 material

Tab. 11: Dominant crystalline phase compositions of the leached crushed materials

Sample	Calcite	Dolomite	Ettringite	Portlandite	Quartz	Hemicarboaluminate	Katoite	Hydroxalcalite	C-S-H	Muscovite
BC12A1	47.4 ± 0.2	9.8 ± 0.1	10.5 ± 0.2	8.3 ± 0.1	1.4 ± 0.1	6.5 ± 0.1	2.3 ± 0.1	3.5 ± 0.1	9.4 ± 0.3	1.1 ± 0.1
BC12AN1	49.0 ± 0.2	10.1 ± 0.1	9.2 ± 0.2	7.9 ± 0.1	1.3 ± 0.1	6.0 ± 0.1	2.4 ± 0.1	3.7 ± 0.1	8.5 ± 0.3	1.9 ± 0.1
BC22A2	38.6 ± 0.2	22.2 ± 0.2	5.9 ± 0.2	8.8 ± 0.1	2.5 ± 0.1	6.0 ± 0.1	0.9 ± 0.1	5.2 ± 0.1	8.3 ± 0.3	1.7 ± 0.2
BC22AN2	37.1 ± 0.2	22.7 ± 0.2	4.4 ± 0.2	9.3 ± 0.1	2.4 ± 0.1	5.7 ± 0.1	0.7 ± 0.1	5.3 ± 0.1	8.4 ± 0.3	4.1 ± 0.4

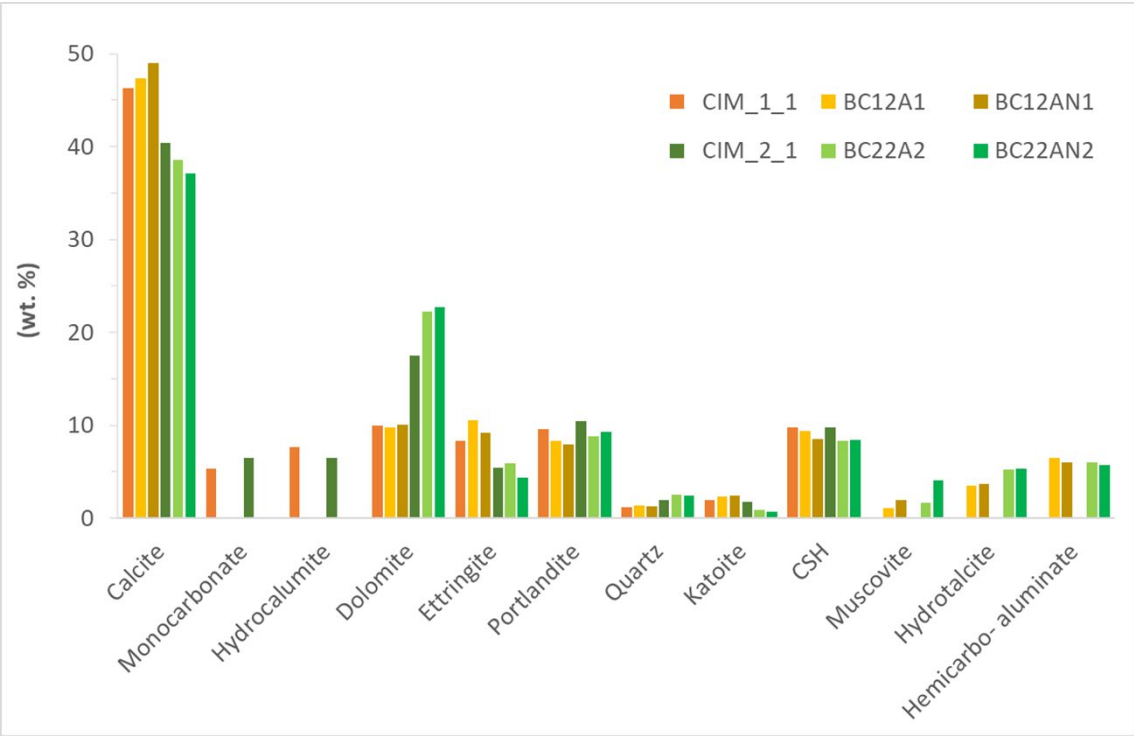


Fig. 56: Comparison of the dominant crystalline phases (initial and leached materials) for the leaching experiments with the crushed materials

 SÚRAO	Migration of Carbon and Iodine in Cementitious Matrix – Final Report	Registration number:
		538/2021

5.8.1.2 XRD and TGA of the coupons

Examples of the TGA graph and XRD pattern of the CIM 265B coupon material are shown in Fig. 57 and Fig. 58. The decomposition of the mineral phases is clearly illustrated by the TGA graph. The composition of the dominant crystalline mineral phases is presented in Tab. 12 and comparisons of the initial and leached materials are presented in Fig. 59, Fig. 60 and Fig. 61. All the TGA graphs and XRD patterns of the leached coupon materials are presented in the Appendix (Fig. 80 - Fig. 95).

The results show that the calcite weight ratios increased, the ratios of quartz, katoite and, in general, dolomite remained approx. stable and the ratios of the ettringite, portlandite and CSH phases decreased (these phases dissolved) in the leached coupons compared to the initial material. All these trends were observed with concern to the leaching of the coupons into deionised water under both aerobic and anaerobic conditions, as well as for the leaching of the coupons into a calcium hydroxide solution under laboratory conditions. The decrease in the weight ratios of the minerals indicated that these phases had dissolved.

As shown in Tab. 12, the leaching process affected the structural properties of the studied materials; the leaching and dissolution of the mineral phases led to increases in the porosity of the samples in all cases, with the exception of the 219L material. This deviation from the dominant trend was unexpected and could not be explained. The results obtained confirmed that the saturation and gravimetric method is suitable for application to cementitious materials and the results are comparable to those obtained via the Hg porosimetry method.

In addition, the results confirmed the differing behaviour of CIM materials extracted from the various depths due to the degree of the heterogeneity of the respective cementitious material. This can be clearly observed particularly concerning the calcite and dolomite ratios (Tab. 13).

Tab. 12: Comparison of the porosity values for the initial source and leached materials (coupon samples)

Sample	Process	porosity (%)	Hg porosimetry (%)
CIM 115	Initial material	~ 51,5	49,96
CIM 113L	Demi. w. leaching (LAB)	~ 55,6	56,88
CIM 113B	Demi. w. leaching (BOX)	~ 56,6	58,05
CIM 115C	Ca(OH) ₂ leaching (LAB)	~ 50,3	50,17
CIM 211	Initial material	~ 43,7	42,71
CIM 219L	Demi. w. leaching (LAB)	~ 39,6	39,64
CIM 219B	Demi. w. leaching (BOX)	~ 44,4	44,66
CIM 211C	Ca(OH) ₂ leaching (LAB)	~ 41,8	44,02
CIM 265	Initial material	-	32,15
CIM 265L	Demi. w. leaching (LAB)	~ 35,7	38,74
CIM 265B	Demi. w. leaching (BOX)	~ 38,0	40,30

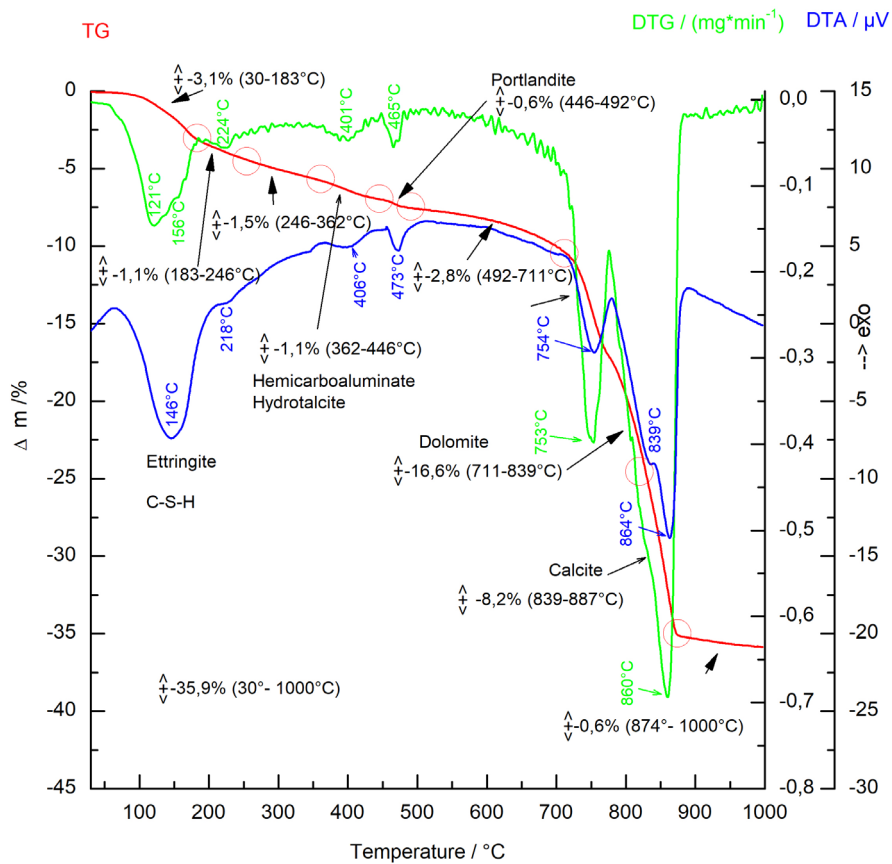


Fig. 57: TGA analysis of the 265B material

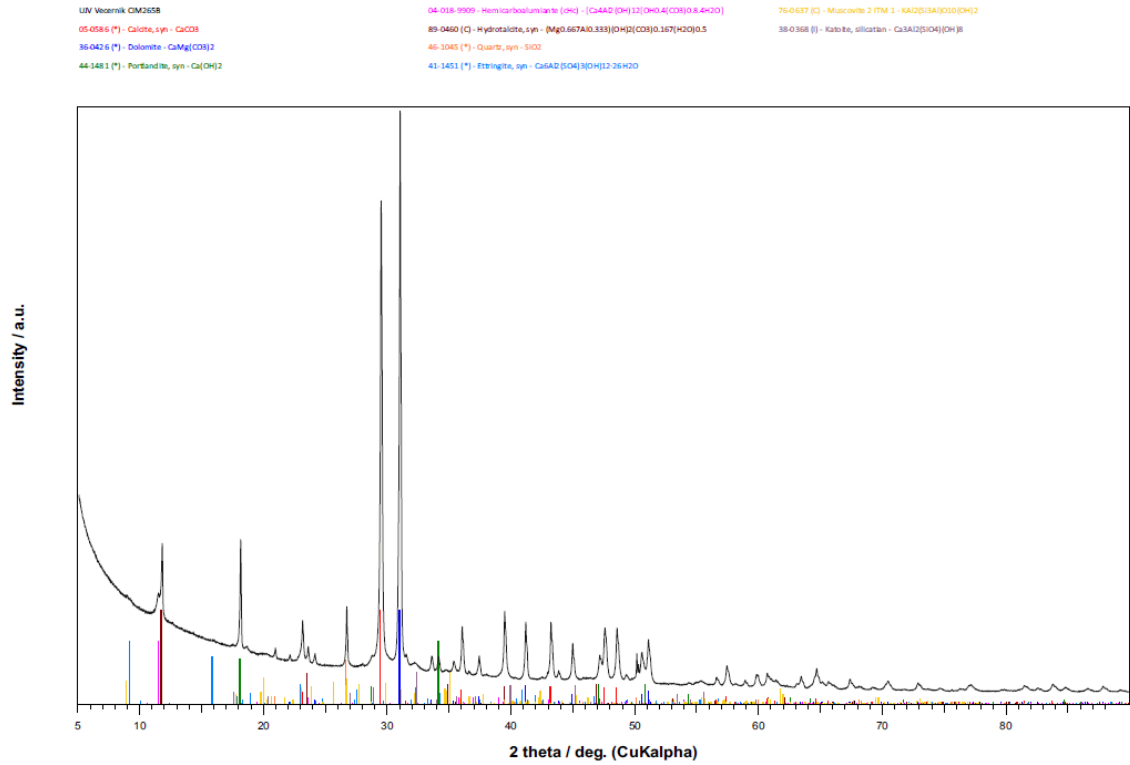


Fig. 58: XRD pattern of the 265B material

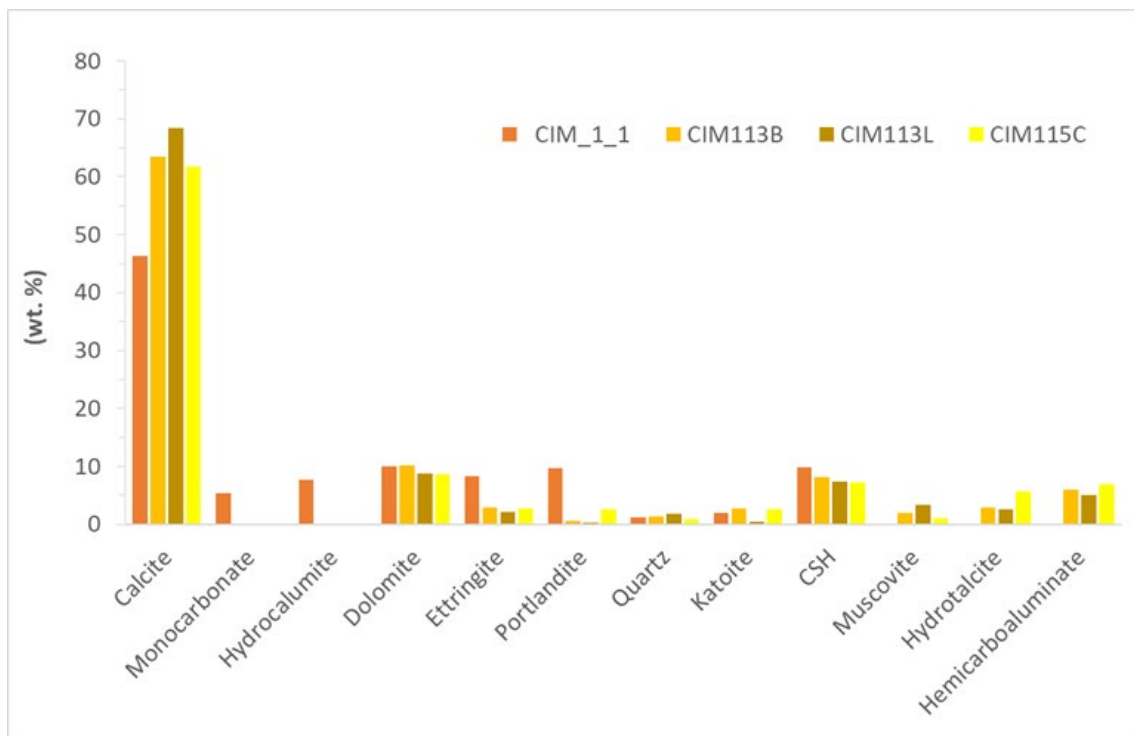


Fig. 59: Comparison of the dominant crystalline phases for the coupon leaching experiments; initial and leached CIM_1_1 materials

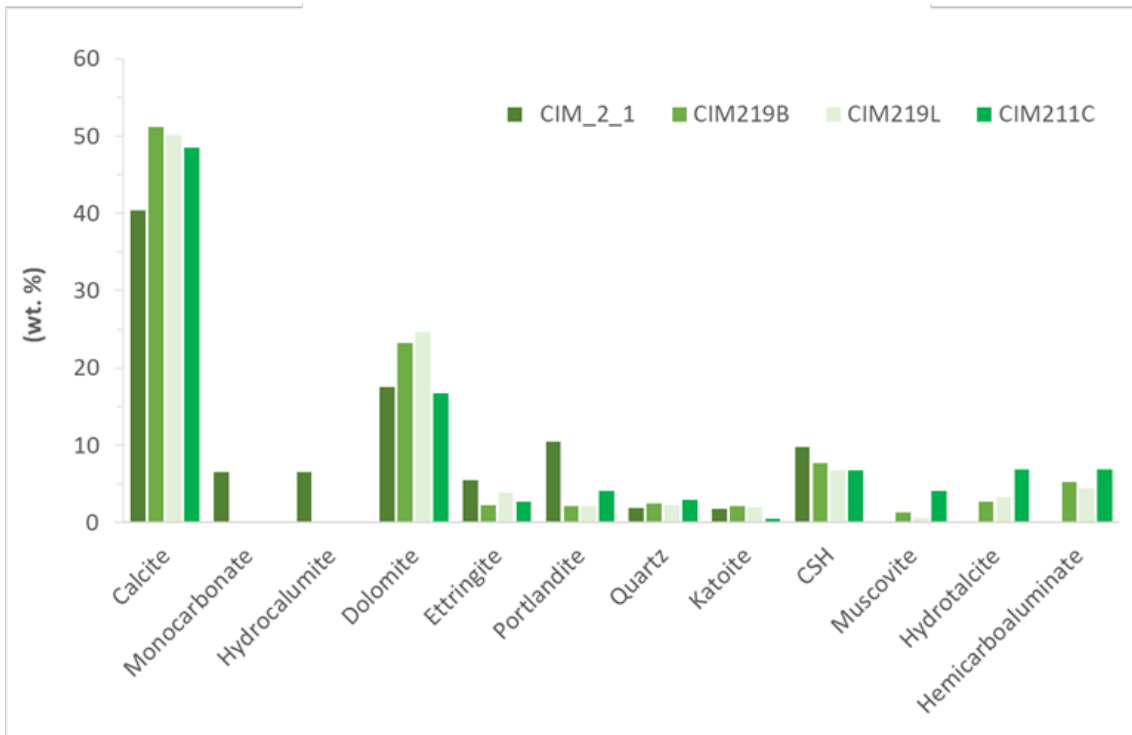


Fig. 60: Comparison of the dominant crystalline phases for the coupon leaching experiments; initial and leached CIM_{2_1} materials

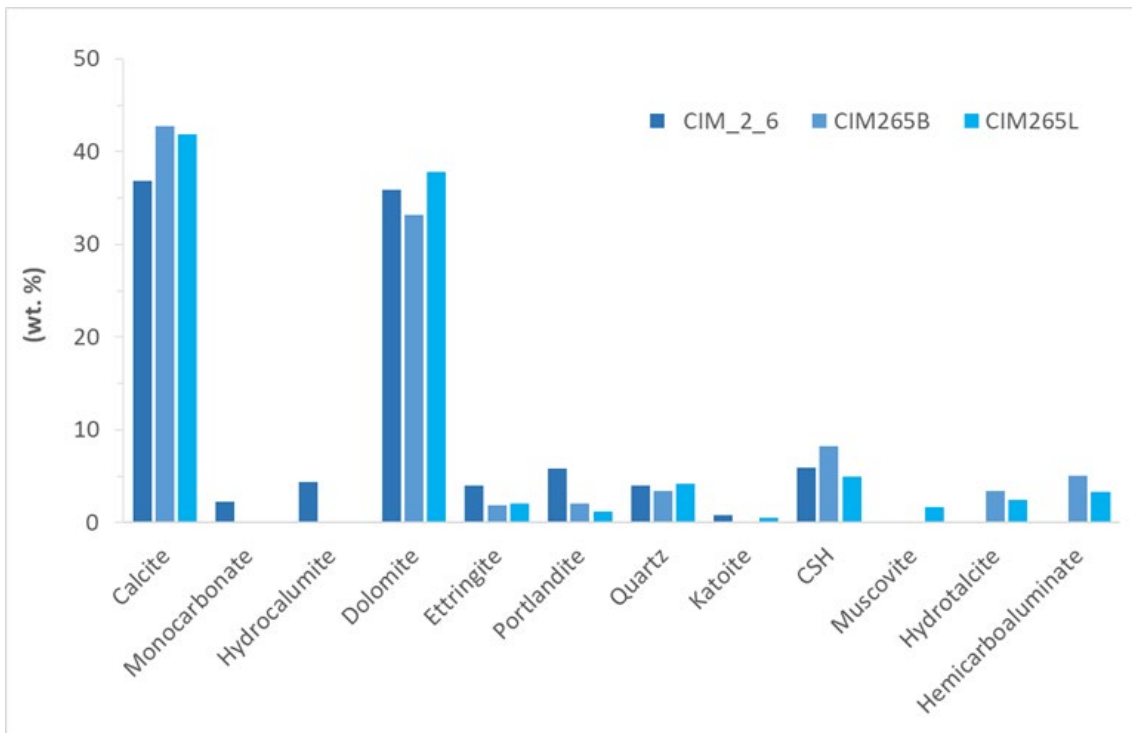


Fig. 61: Comparison of the dominant crystalline phases for the coupon leaching experiments; initial and leached CIM_{2_6} materials

Tab. 13: Dominant crystalline phase compositions of the leached coupon materials

Sample	Calcite	Dolomite	Ettringite	Portlandite	Quartz	Hemicarboaluminate	Katoite	Hydroxalite	C-S-H	Muscovite
CIM 113B	63.5 ± 0.3	10.1 ± 0.1	2.9 ± 0.2	0.5 ± 0.1	1.3 ± 0.1	5.9 ± 0.2	2.8 ± 0.1	2.9 ± 0.1	8.1 ± 0.2	2.0 ± 0.2
CIM 113L	68.5 ± 0.3	8.8 ± 0.1	2.1 ± 0.2	0.3 ± 0.1	1.8 ± 0.1	5.0 ± 0.2	0.4 ± 0.1	2.6 ± 0.1	7.3 ± 0.3	3.3 ± 0.2
CIM 115C	61.8 ± 0.3	8.6 ± 0.2	2.8 ± 0.2	2.6 ± 0.1	0.8 ± 0.1	6.9 ± 0.1	2.6 ± 0.1	5.7 ± 0.1	7.2 ± 0.3	1.0 ± 0.1
CIM 211C	48.5 ± 0.3	16.7 ± 0.2	2.7 ± 0.2	4.1 ± 0.1	2.9 ± 0.1	6.9 ± 0.2	0.5 ± 0.1	6.9 ± 0.1	6.8 ± 0.3	4.1 ± 0.4
CIM 219B	51.2 ± 0.2	23.2 ± 0.1	2.2 ± 0.2	2.1 ± 0.1	2.4 ± 0.1	5.2 ± 0.1	2.1 ± 0.1	2.7 ± 0.1	7.7 ± 0.2	1.3 ± 0.1
CIM 219L	50.1 ± 0.2	24.6 ± 0.2	3.9 ± 0.2	2.1 ± 0.1	2.2 ± 0.1	4.4 ± 0.1	2.0 ± 0.1	3.3 ± 0.1	6.8 ± 0.2	0.6 ± 0.3
CIM 265B	42.7 ± 0.2	33.2 ± 0.2	1.9 ± 0.2	2.1 ± 0.1	3.4 ± 0.1	5.1 ± 0.1	-	3.4 ± 0.1	8.2 ± 0.3	-
CIM 265L	41.9 ± 0.2	37.8 ± 0.2	2.1 ± 0.2	1.2 ± 0.1	4.2 ± 0.1	3.3 ± 0.1	0.5 ± 0.1	2.4 ± 0.1	5.0 ± 0.2	1.7 ± 0.2

 SÚRAO	Migration of Carbon and Iodine in Cementitious Matrix – Final Report	Registration number:
		538/2021

5.8.2 Solid phases following column interaction

The TGA graph and the XRD pattern of the CIM 24B-4 material are shown in Fig. 62 and Fig. 63. All the TGA graphs and XRD patterns of the interacted materials from the column experiments are presented in the Appendix (Fig. 96 - Fig. 111). The TGA graphs illustrate the decomposition of the mineral phases. The dominant crystalline mineral phase compositions are presented in Tab. 14 and a comparison of the initial and the interacted materials from the columns is shown in Fig. 64 and Fig. 65.

The results indicate the increased calcite weight ratios, reduced amounts of dolomite and the almost total dissolution of ettringite and portlandite in all the interacted materials. The CSH phase ratios decreased compared to those of the initial material in columns K14A and K14B, thus indicating the dissolution of these phases.

Differences in the composition of the materials from the input and output of the columns can be observed with respect to all the column (K14A, K14B, K24A, K24B) materials. Due to the small dimensions of the columns and the small amounts of infill materials, the differences are in mere single percentage units. Nevertheless, the action of various dissolution processes can be confirmed in the materials from the input and the output parts of the columns.

The results obtained also confirmed the differing behaviour of the CIM materials taken from the various depths due to the heterogeneity of the respective initial cementitious materials. This is evident primarily from the calcite and dolomite ratios.

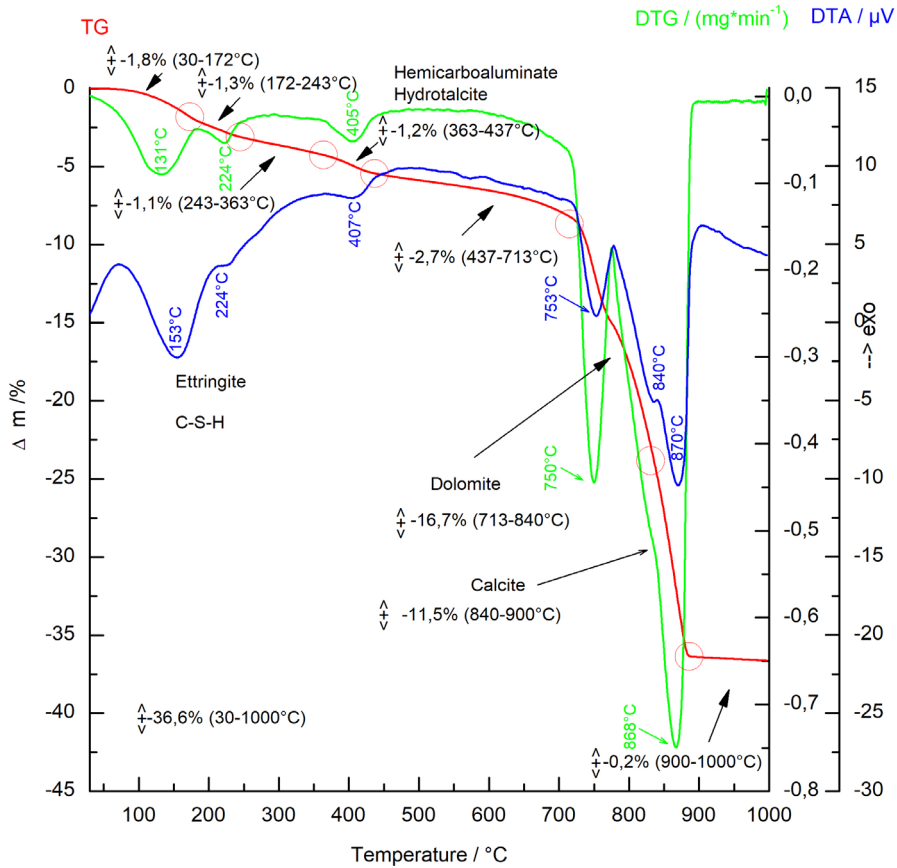


Fig. 62: TGA analysis of the CIM24B-A material

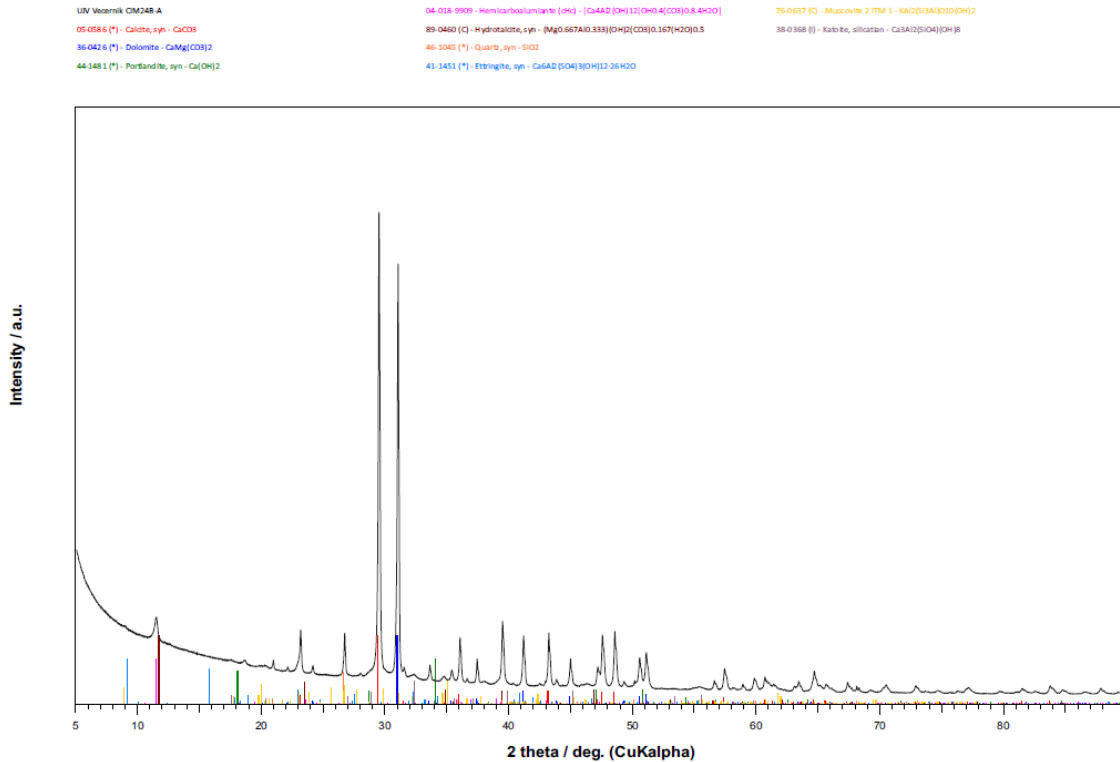


Fig. 63: XRD pattern of the CIM24B-A material

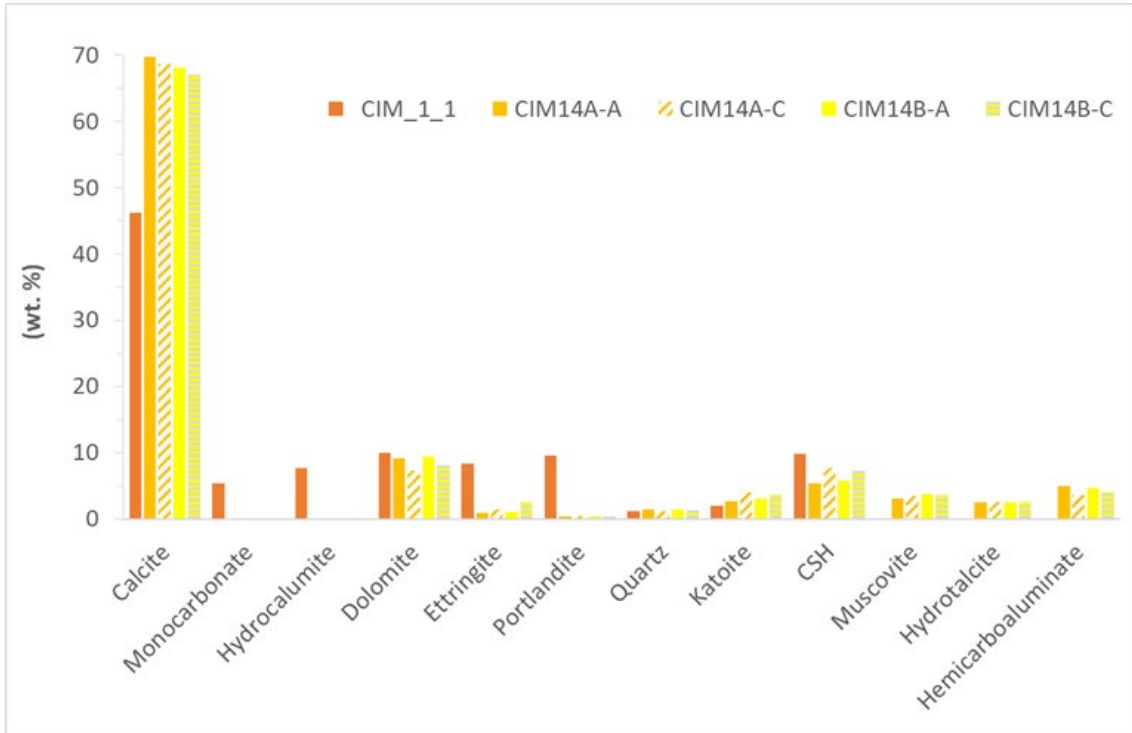


Fig. 64: Comparison of the dominant crystalline phases for the column interaction experiments; initial and leached CIM_1_1 materials

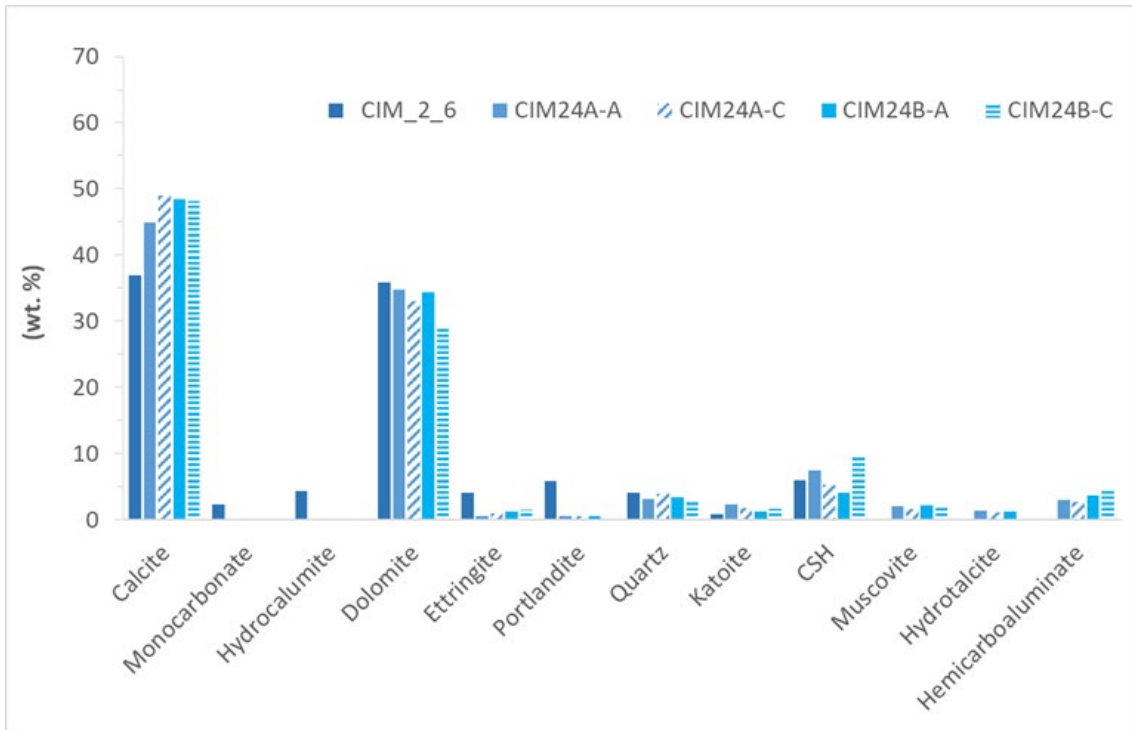


Fig. 65: Comparison of the dominant crystalline phases for the column interaction experiments; initial and leached CIM_2_6 materials

Tab. 14: Dominant crystalline phase compositions of the materials following the column interaction experiments

Sample	Calcite	Dolomite	Ettringite	Portlandite	Quartz	Hemicarboaluminate	Katoite	Hydrotalcite	C-S-H	Muscovite
CIM 14A-A	69.7 ± 0.3	9.2 ± 0.1	0.9 ± 0.2	0.3 ± 0.1	1.4 ± 0.1	5.0 ± 0.2	2.7 ± 0.1	2.5 ± 0.1	5.3 ± 0.3	3.1 ± 0.1
CIM 14A-C	68.6 ± 0.3	7.3 ± 0.1	1.4 ± 0.2	0.5 ± 0.1	1.2 ± 0.1	3.6 ± 0.2	4.0 ± 0.1	2.5 ± 0.1	7.6 ± 0.3	3.5 ± 0.2
CIM 14B-A	68.1 ± 0.3	9.4 ± 0.1	1.0 ± 0.2	0.3 ± 0.1	1.4 ± 0.1	4.7 ± 0.2	3.0 ± 0.1	2.5 ± 0.1	5.8 ± 0.4	3.8 ± 0.2
CIM 14B-C	67.0 ± 0.3	8.0 ± 0.1	2.5 ± 0.2	0.3 ± 0.1	1.3 ± 0.1	4.0 ± 0.1	3.6 ± 0.1	2.5 ± 0.1	7.2 ± 0.3	3.6 ± 0.2
CIM 24A-A	44.9 ± 0.2	34.8 ± 0.2	0.6 ± 0.1	0.5 ± 0.1	3.1 ± 0.1	3.0 ± 0.2	2.3 ± 0.1	1.3 ± 0.1	7.4 ± 0.4	2.1 ± 0.2
CIM 24A-C	49.0 ± 0.2	33.0 ± 0.2	1.0 ± 0.2	0.5 ± 0.1	3.9 ± 0.1	2.7 ± 0.2	1.8 ± 0.1	1.1 ± 0.1	5.3 ± 0.3	1.7 ± 0.1
CIM 24B-A	48.4 ± 0.2	34.4 ± 0.2	1.2 ± 0.2	0.5 ± 0.1	3.4 ± 0.1	3.6 ± 0.2	1.2 ± 0.1	1.2 ± 0.1	4.0 ± 0.3	2.2 ± 0.1
CIM 24B-C	48.1 ± 0.2	29.0 ± 0.2	1.5 ± 0.2	0.6 ± 0.1	2.8 ± 0.1	4.6 ± 0.1	1.7 ± 0.1	-	9.9 ± 0.3	1.8 ± 0.1

6 Data comparison

The cement material studied in the first phase of the CIM project appeared to be very heterogeneous even following a visual inspection. The heterogeneity of the physical/structural parameters was confirmed by the porosity measurements and the evaluation of permeability. A strong correlation was evident between these parameters and the sample depth.

The following parameters were used for the predictive simulations of the *in-situ* experiments performed by J. Soler for NAGRA (presentation at a CIM partner meeting in December 2020):

$$\begin{aligned} & \text{porosity} - 26.3\% \\ D_e (\text{HTO}) &= 1.43 \times 10^{-10} \text{ m}^2/\text{s} \\ D_e ({}^{36}\text{Cl}) &= 4.49 \times 10^{-11} \text{ m}^2/\text{s} \end{aligned}$$

It is evident that the porosity value differs from the values obtained for the materials taken from a depth of < 1.5 m (35-50%).

In addition, the mineralogical composition of the cement material (Tab. 15) differs from that determined for the materials from a depth of < 1.5 m studied in this report.

Tab. 15: Composition of the cement material from the deeper parts of the CIM drilled core

Mineral	Vol. fr. (1)	Vol. fr. (2)	Vol. fr. (3)
CSH	0.154	0.205	0.093
Portlandite	0.070	0.094	0.043
Ettringite	0.026	0.035	0.016
Hydrotalcite	0.005	0.007	0.003
Monocarb.	0.037	0.050	0.023
Calcite	0.445	0.462	0.425

Drilled borehole hydraulic testing performed by NAGRA in 2020 (presentation at a CIM partner meeting in December 2020) revealed a hydraulic coefficient K of $(0.65 - 3.6) \times 10^{-11}$ m/s. These values are up to one order of magnitude lower than those determined for the materials taken from a depth of < 1.5 m studied in this report.

Thus, it is evident that it is not possible to directly compare the data obtained from the CIM experiments without additional information on the materials. The heterogeneity of the material affected all the parameters considered: porosity, permeability, mineral and chemical composition, diffusion and sorption.

7 Conclusions

This report provides a summary of the results concerning the mineralogical, chemical and transport properties of the cement pastes studied in the CIM project. The tested materials originated from the cement infill of the upper part of an experimental borehole at the Grimsel Test Site, which was instrumented for the purposes of the *in-situ* CIM experiment. The principal aim of the main part of the CIM project is to study the *in-situ* migration and sorption of ^{14}C and ^{129}I through cementitious materials and the granitic host rock, including the consideration of the transport mechanism at the interface between these two materials.

Two core lengths were delivered to the ÚJV laboratory from which samples were prepared from three different sampling depths (on average 0.65, 1.15 and 1.45 m). The research consisted of the performance of a series of sorption and diffusion experiments, the taking of porosity and permeability measurements, degradation via leaching and interaction with various liquid phases followed by the chemical analysis of the liquid phases, and the description of the changes that occurred in the solid phase materials (XRD analysis of the mineral composition and thermogravimetry).

The studied carbon (^{14}C) and iodine (^{129}I) radionuclides comprise two of the main contaminants that could be released from radioactive waste repositories. Their importance lies in their significant contributions to dose rates over the long-term as indicated by the respective performance assessment calculations.

The experimental studies clearly showed that a strong correlation exists between the porosity of the sample and the sampling depth. It was confirmed that the saturation and gravimetric method for the determination of porosity produces results that are comparable to those of the mercury porosimetry method.

The determined k_{10} filtration coefficients for the material from the upper part (depth of approx. 70 cm) of the drilled core evinced almost one order of magnitude higher values than for the material taken from a depth of approx. 120cm. This corresponded to the decrease with depth of the porosity values.

The initial analysis of the CIM cement samples obtained from the drilled core indicated increasing amounts of dolomite and quartz with the increasing depth of the drilled core.

Predictive geochemical modelling was performed for the calculation of the composition of the products of the interaction of groundwater with the CIM cement materials. The modelled results principally revealed enhanced calcium, magnesium and sulphate ion concentrations and decreased concentrations of carbonate ions in the equilibrated solutions following interaction. The tracer speciation modelling confirmed that acetate, formate and iodide comprise stable chemical forms in the studied environment.

The results of the chemical analysis of the liquid phases following the degradation of the cementitious materials via interaction and leaching revealed the dissolution of the cement material compounds by increased concentrations of e.g. calcium and silicon. The degradation was confirmed by the TGA and XRD analysis that indicated decreasing amounts of portlandite, ettringite and CSH phases and changes in the calcite/dolomite ratios.

The laboratory experiments revealed evidence of the weak sorption of the ^{14}C tracers (in the form of acetate and formate) on the cementitious material, with retardation coefficient values of up to 2.5 ml/g. Higher retardation coefficient values were determined for the ^{125}I iodide tracer

 SÚRAO	Migration of Carbon and Iodine in Cementitious Matrix – Final Report	Registration number:
		538/2021

(up to 65 ml/g). The experiments confirmed that cementitious materials exhibit a non-zero sorption effect and that they have the potential to contribute to the retardation of these radionuclides in engineered barrier materials.

The diffusion experiments revealed that the tracers migrated through the samples at different velocities; the migration of tritium was, as expected, revealed to be a non-interacting process, the ^{14}C tracers were slightly retarded, and the highest level of interaction and migration retardation was observed with respect to the ^{125}I iodide tracer. A clear correlation was evident between the D_e values of the three tracers and the average depth at which the HCP core was drilled. The highest values were observed with respect to the non-sorbing HTO tracer, whereas around two times lower values were determined for the ^{14}C tracer and even lower D_e values were recorded in the case of the ^{125}I tracer.

The results obtained clearly indicate that all the studied parameters evinced a strong correlation with the sampling depth. Therefore, since the cementitious infill in the upper part of the borehole is very heterogenous, the results cannot be directly used for the prediction of the properties of the material in the deeper parts of the borehole.

The experiments performed and described in this report studied a unique material, a cement-based mixture that has been in long-term contact with the rock environment in an underground laboratory. To date, all the experiments that have been performed on cementitious materials concerned freshly prepared samples of cement pastes, mortars or concretes. It is known that cement-based samples evolve over time, especially when in contact with water. Interaction with groundwater is capable of affecting the chemical, mineralogical, structural and mechanical properties of such materials, which results in changes in the migration and retardation parameters. The material used in the research is the only material available for laboratory experimentation that has been affected by a natural underground environment.

The results obtained provide the first set of data on degraded cement-based materials which can be used in the repository safety assessment and radioactive waste safety calculations.

The subsequent phases of the CIM project will focus on the *in-situ* experiment and supporting laboratory experiments that will consider materials (cement, host rock) from depths of > 3 m and from the depth of the injection interval of the *in-situ* experiment. The experiments will significantly enhance the understanding of the behaviour of ^{14}C , ^{129}I and other selected radionuclides under real *in-situ* conditions in a cement-based barrier.

Despite the fact that the CIM project is being conducted *in-situ* at the Grimsel laboratory, the results obtained can be used in the Czech repository safety assessment and radioactive waste safety calculations, while bearing in mind the heterogeneity of the materials studied so far. It is expected that more homogeneous materials will be extracted from the deeper parts of the CIM drilled core. The heterogeneity of the material was most probably caused by the sedimentation of the fresh cement material infill prior to hardening. With respect to the use of cementitious materials in radioactive waste repositories, the homogeneity of the material will be ensured via the strict application of the respective technological and material acceptance criteria.

 SÚRAO	Migration of Carbon and Iodine in Cementitious Matrix – Final Report	Registration number:
		538/2021

8 References

- BRÁZDA L., KAŠPAR V., VEČERNÍK P. (2019): Migration of Carbon and Iodine in a Cementitious Matrix – Interim Report, Technical report 461/2020, SÚRAO / ÚJV Řež, a. s., Praha.
- COLLIER N. C., SHARP J. H., MILESTONE N. B., HILL J., GODFREY I. H. (2016): The influence of water removal techniques on the composition and microstructure of hardened cement pastes, *Cement and Concrete Research* 38, 737–744
- CRANK J. (1975): *The Mathematics of diffusion*. Second edition. Oxford university press. ISBN 0198533446.
- DIAMOND S. (2000): Mercury porosimetry: An inappropriate method for the measurement of pore size distributions in cement-based materials, *Cement and Concrete Research* 30, 1517-1525.
- DAY R.L., MARSH B.K. (1988): Measurement of Porosity in Blended Cement Pastes, *Cement and Concrete Research* 18, 63–73.
- GTS WEBPAGE (2021): <https://www.grimsel.com/gts-phase-vi/cim-carbon-14-and-iodine-129-migration-in-cement/cim-introduction-aims>
- JAKOB, A. (2004): Matrix diffusion for performance assessment – experimental evidence, modelling assumptions and open issues. PSI Report Nr. 04-08.
- KONTAR K., LANYON B., MARTIN A.J. (2019): Far field borehole instrumentation and conceptual model for CIM hydraulics, *Aktennotiz AN 19-320, NAGRA*, 27 p.
- MATSUMOTO J., BANBA T., MURAOKA S. (1994): Adsorption of Carbon-14 on Mortar, *MRS Online Proceedings Library* 353, 1029-1035
- MELNYK T.W., SKEET A. (1986) An improved technique for determination of rock porosity. *Canadian Journal of Earth Sciences*, 23, 1068–1074.
- SKAGIUS K., NERETNIEKS I. (1986). Porosities and diffusivities of some non-sorbing species in crystalline rocks. *Water Resour. Res.* 22, 389–397.
- VAN LOON L. R., SOLER J. M, JAKOB A., BRADBURY M. H. (2003): Effect of confining pressure on the diffusion of HTO, $^{36}\text{Cl}^-$ and $^{125}\text{I}^-$ in a layered argillaceous rock (Opalinus Clay): diffusion perpendicular to the fabric. *Applied Geogemistry* 18, 1653-1662.
- VEČERNÍK, P., DRTINOVÁ, B., BÁRTA, J., BRÁZDA, L., HAVLOVÁ, V., KITTNEROVÁ, J., KOLOMÁ, K., ROSENDORF, T., VOPÁLKA, D. (2017): Transportní vlastnosti cementových materiálů – průběžná výzkumná zpráva III. – MS SÚRAO, TZ 209/2017, Praha.
- VEČERNÍK, P., DRTINOVÁ, B., BRÁZDA, L., HAVLOVÁ, V., KAŠPAR, V., KITTNEROVÁ, J., ŠUSTKOVÁ, E., VOPÁLKA, D. (2019a): Transportní vlastnosti cementových materiálů – průběžná zpráva IV. – MS SÚRAO, TZ 365/2019, Praha.
- VEČERNÍK P., BRÁZDA L., HAVLOVÁ V., GALEKOVÁ E., HOFMANOVÁ E., KAŠPAR V. (2019b): Transportní vlastnosti cementových materiálů – průběžná zpráva V. – MS SÚRAO, TZ 428/2019, Praha.
- VEČERNÍK P., DRTINOVÁ B., BÁRTA, J., BRÁZDA L., GALEKOVÁ E., HAVLOVÁ V., HOFMANOVÁ E., KAŠPAR V., KITTNEROVÁ J., KOLOMÁ K., ROSENDORF, T., VOPÁLKA D. (2019c): Transport properties of cement materials – Final report. – MS SÚRAO, ZZ 430/2019/EN, Praha.

Appendix

Tab. 16: Description of the analysed materials

Material	Avg. depth	Process	Form in experiment
CIM_1_1	0.65	Initial material	-
CIM_2_1	1.15	Initial material	-
CIM_2_6	1.45	Initial material	-
BC12A1	0.65	Ca(OH) ₂ leaching (LAB)	crushed
BC12AN1	0.65	Ca(OH) ₂ leaching (BOX)	crushed
BC22A2	1.45	Ca(OH) ₂ leaching (LAB)	crushed
BC22AN2	1.45	Ca(OH) ₂ leaching (BOX)	coupon
CIM113B	0.65	Demi. w. leaching (BOX)	coupon
CIM113L	0.65	Demi. w. leaching (LAB)	coupon
CIM115C	0.65	Ca(OH) ₂ leaching (LAB)	coupon
CIM211C	1.15	Ca(OH) ₂ leaching (LAB)	coupon
CIM219B	1.15	Demi. w. leaching (BOX)	coupon
CIM219L	1.15	Demi. w. leaching (LAB)	coupon
CIM265B	1.45	Demi. w. leaching (BOX)	coupon
CIM265L	1.45	Demi. w. leaching (LAB)	coupon
CIM14A-A	0.65	Column interaction - input	crushed
CIM14A-C	0.65	Column interaction - output	crushed
CIM14B-A	0.65	Column interaction - input	crushed
CIM14B-C	0.65	Column interaction - output	crushed
CIM24A-A	1.45	Column interaction - input	crushed
CIM24A-C	1.45	Column interaction - output	crushed
CIM24B-A	1.45	Column interaction - input	crushed
CIM24B-C	1.45	Column interaction - output	crushed

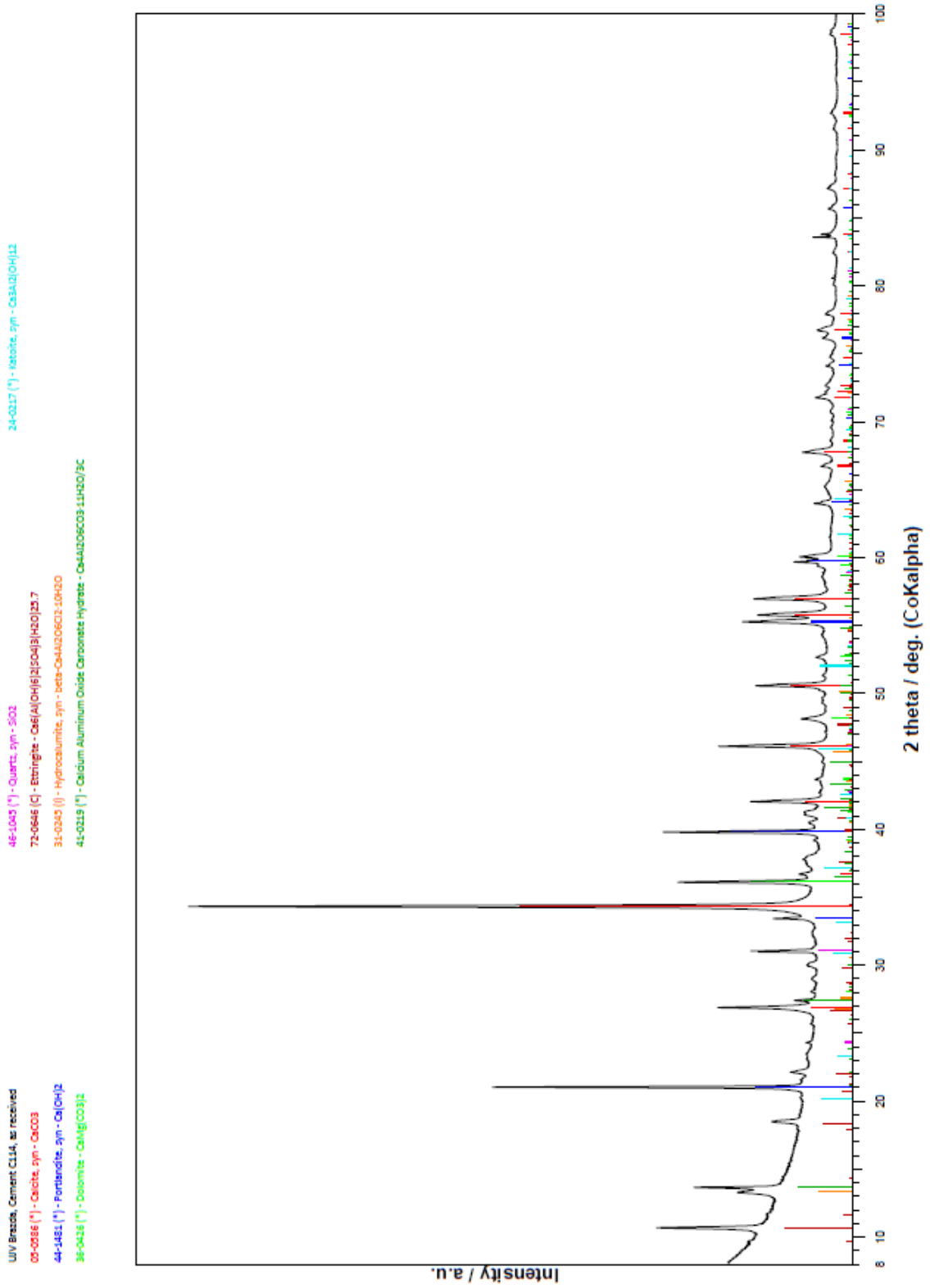


Fig. 66: XRD pattern of the CIM_1_1 material

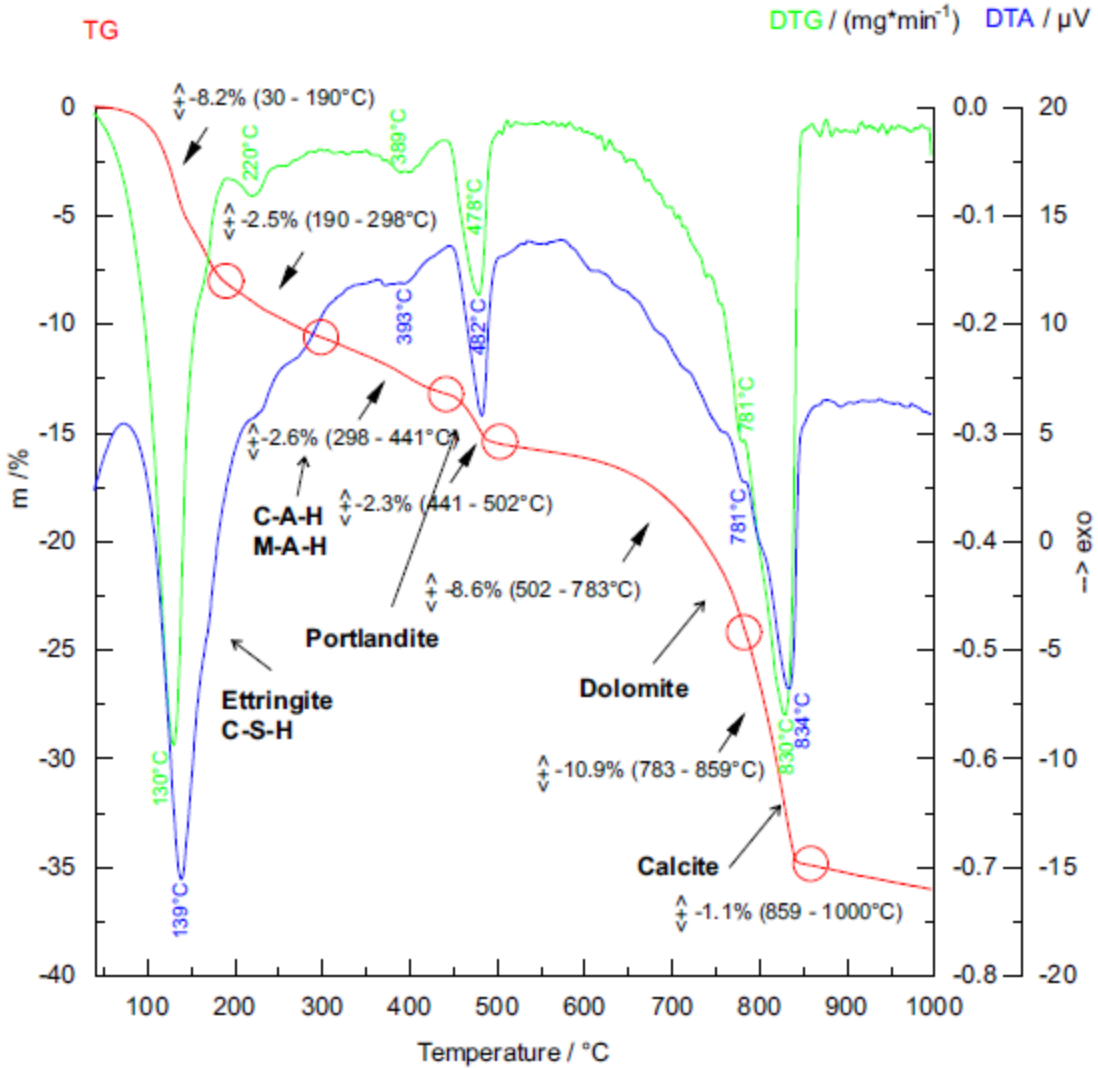


Fig. 67: TGA analysis of the CIM_1_1 material

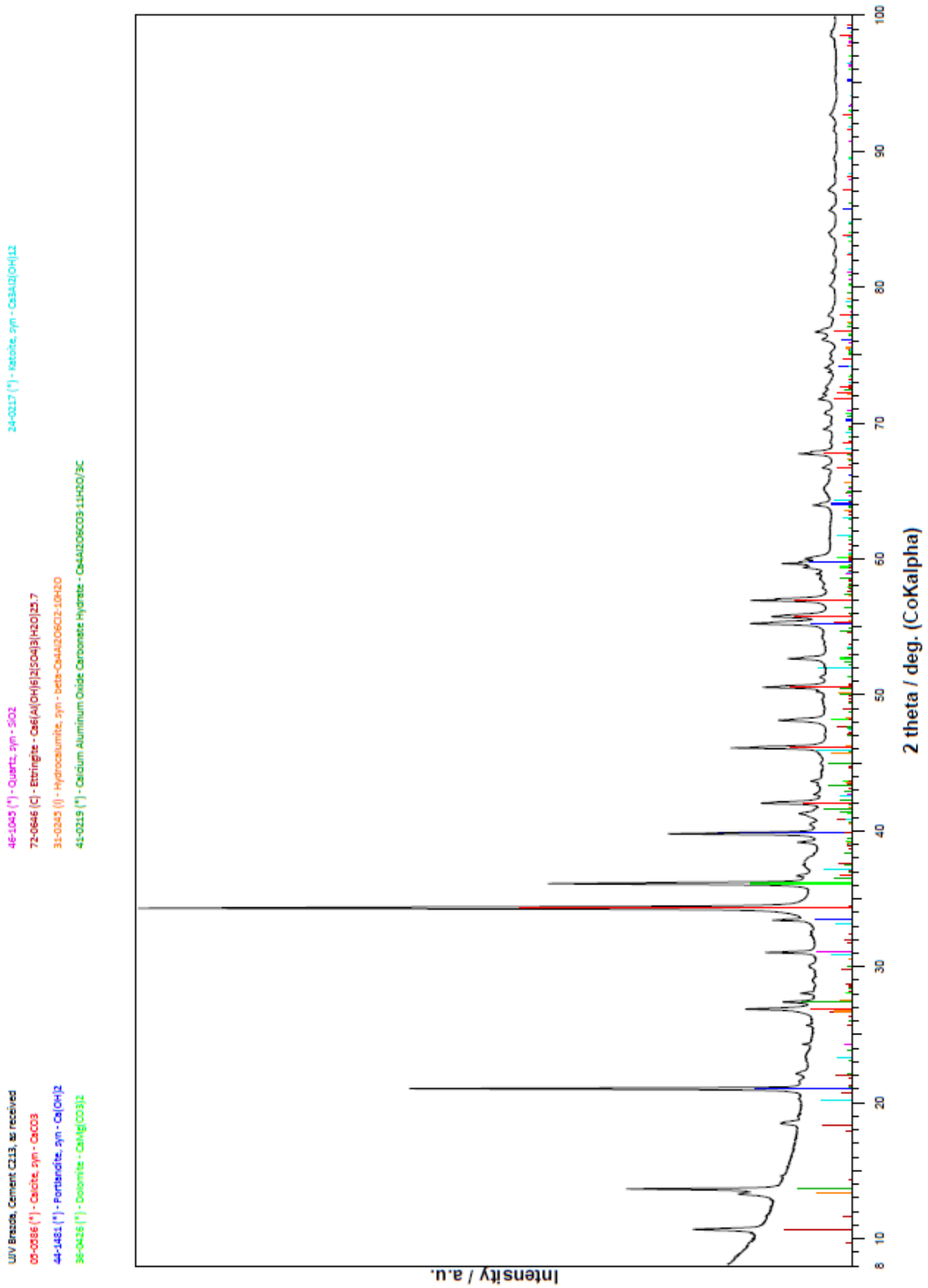


Fig. 68: XRD pattern of the CIM_2_1 material

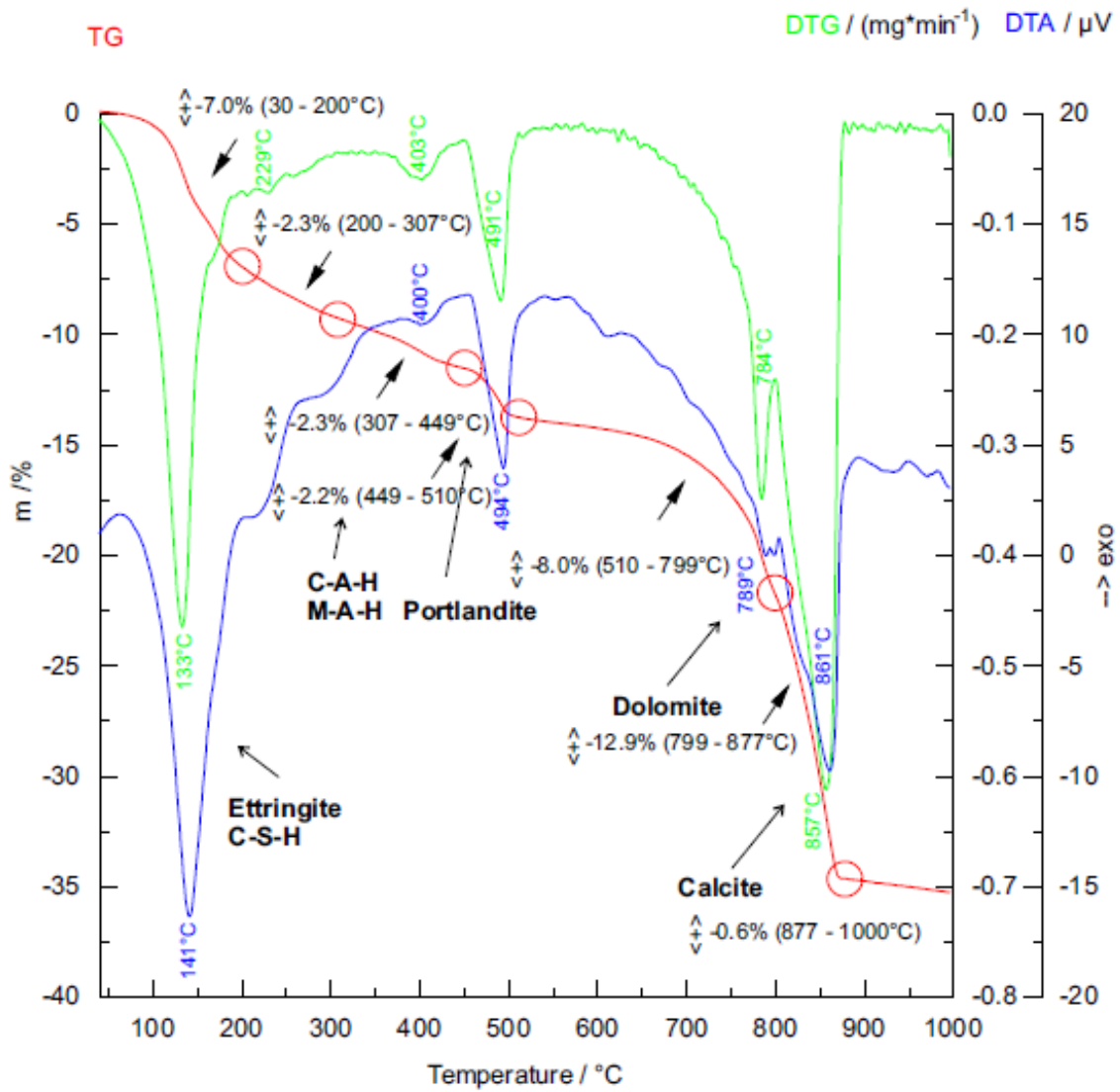


Fig. 69: TGA analysis of the CIM_2_1 material

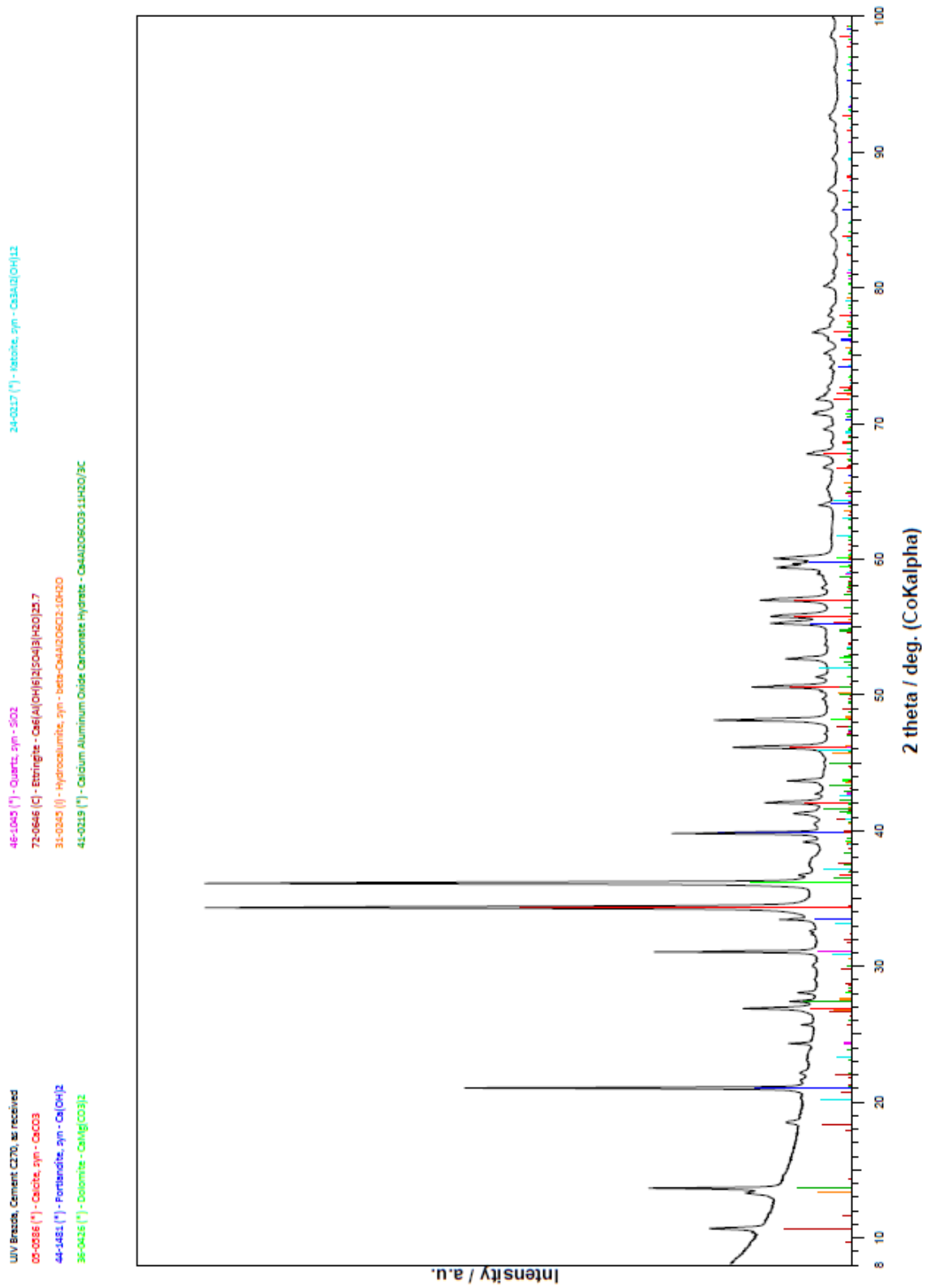


Fig. 70: XRD pattern of the CIM_2_6 material

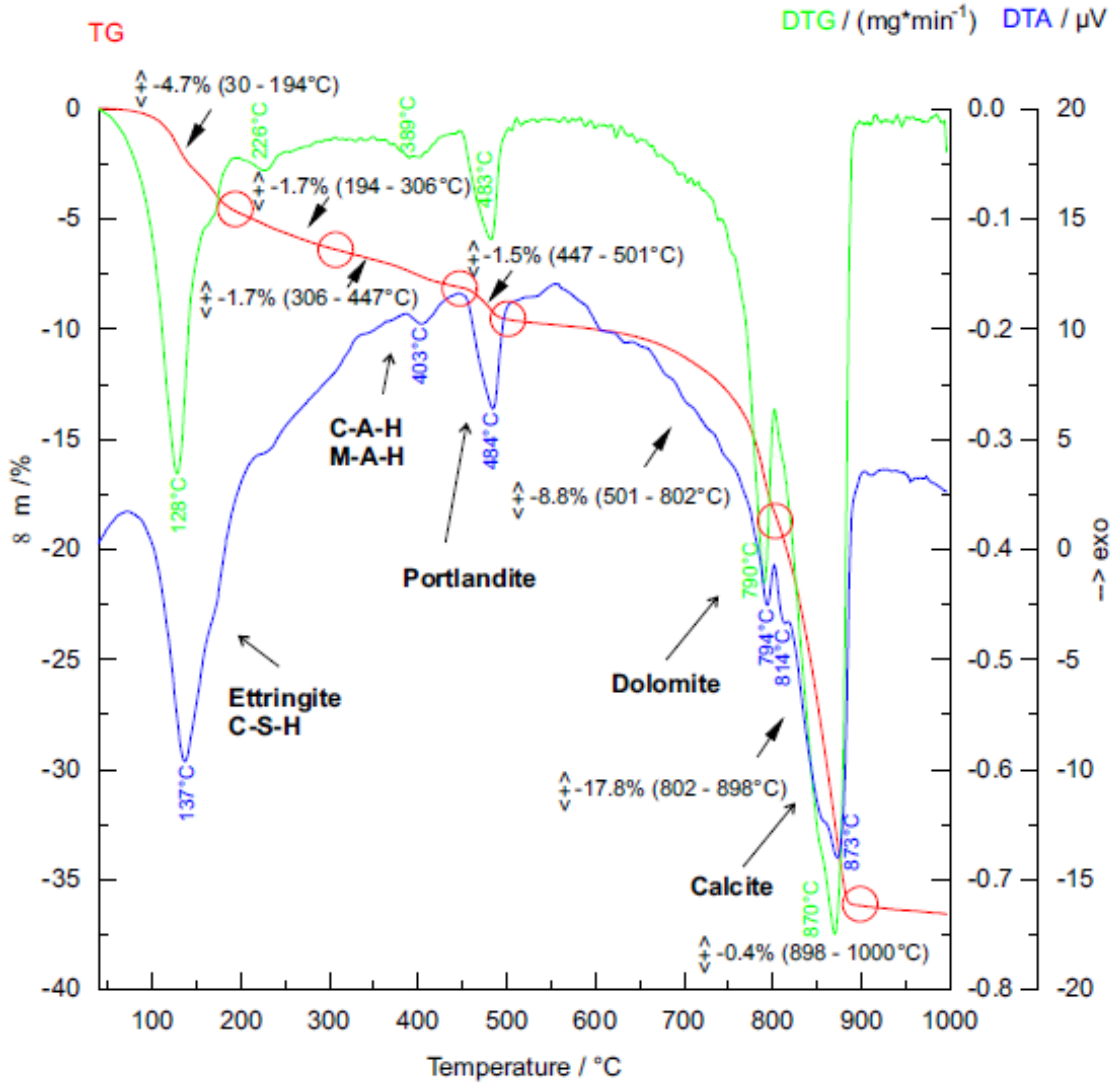


Fig. 71: TGA analysis of the CIM_2_6 material

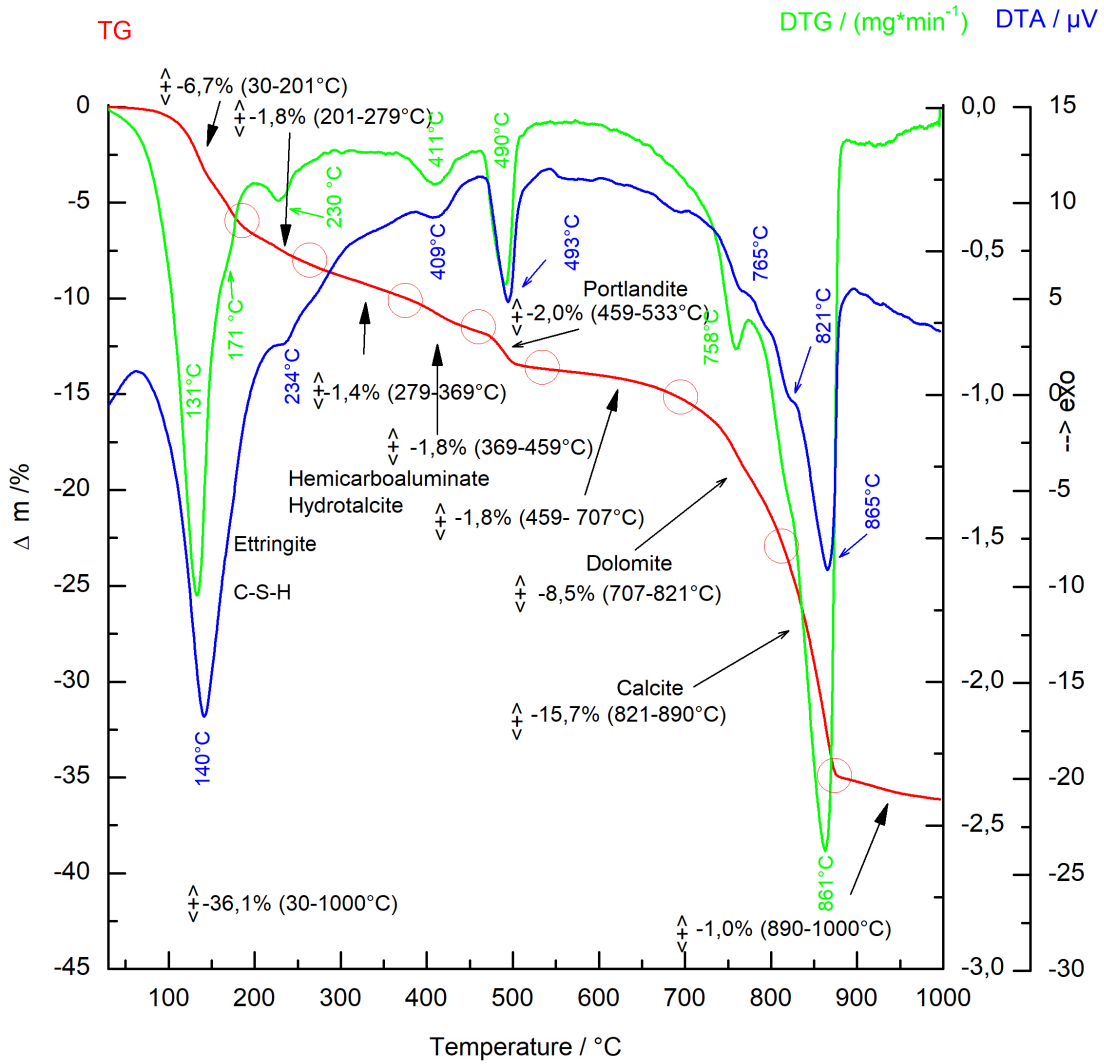


Fig. 72: TGA analysis of the BC12A1 material

UV Vecernik BC12A1
 05-0586 (*) - Calcite, syn - CaCO3
 36-0426 (*) - Dolomite - CaMg(CO3)2
 44-1481 (*) - Portlandite, syn - Ca(OH)2
 04-018-9909 - Hemihydroaluminat (hhc) - [Ca4Al2(OH)12(OH)0.4(CO3)0.8.4H2O]
 89-0460 (C) - Hydrocalcite, syn - (Mg0.667Al0.333)(OH)2(CO3)0.167(H2O)0.5
 46-1045 (*) - Quartz, syn - SiO2
 41-1451 (*) - Ettringite, syn - Ca6Al2(SO4)3(OH)12.6H2O
 76-0637 (C) - Muscovite 2 ITM 1 - KAl2(Si3Al)O10(OH)2
 38-0568 (I) - Kaolite, silification - Ca3Al2(SiO4)(OH)8

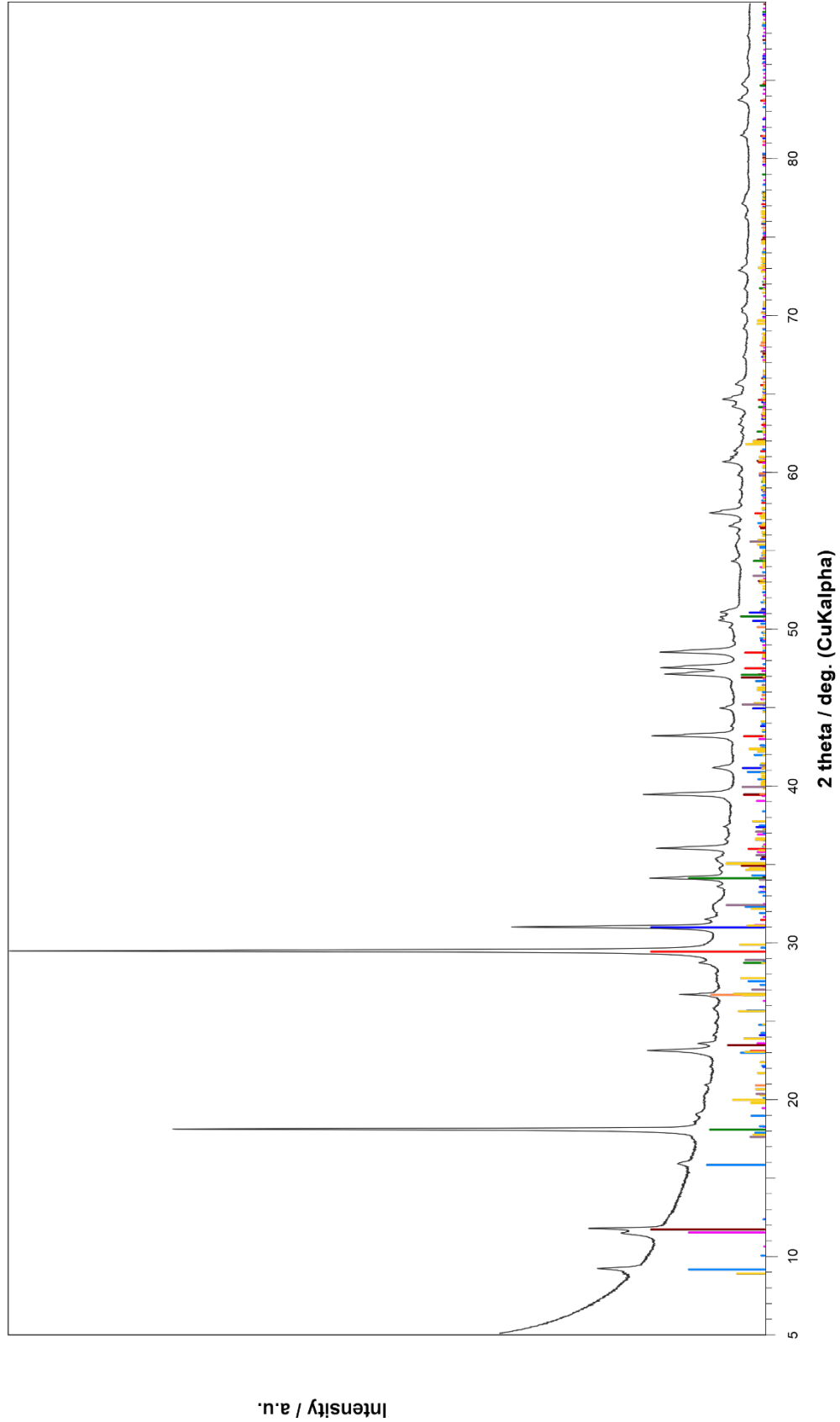


Fig. 73: XRD pattern of the BC12A1 material

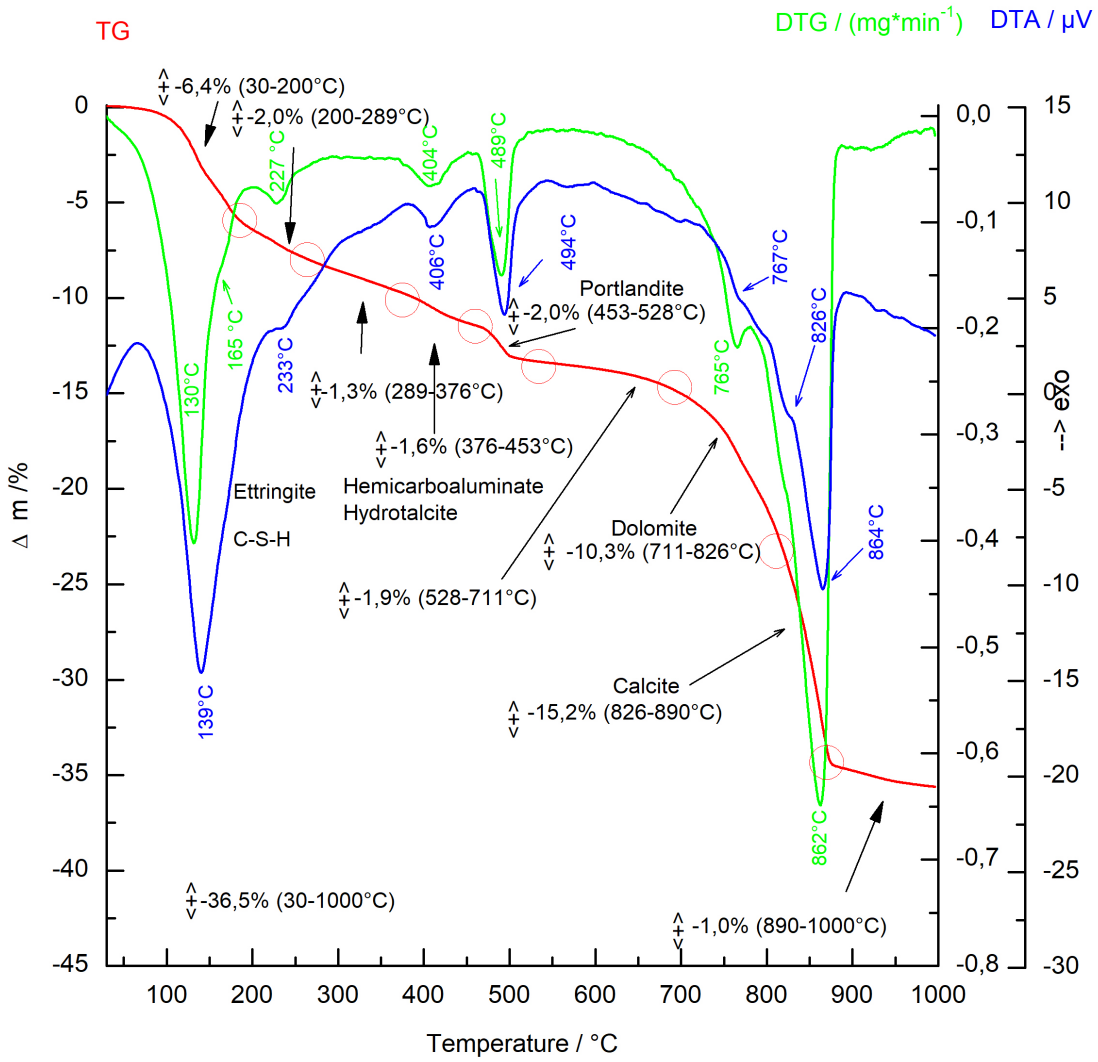


Fig. 74: TGA analysis of the BC12AN1 material

UV Vecernik BC12AN1
 05-0586 (*) - Calcite, syn - CaCO3
 36-0426 (*) - Dolomite - CaMg(CO3)2
 44-1481 (*) - Portlandite, syn - Ca(OH)2
 04-018-9909 - Hemihydroaluminat (CH) - [Ca4Al2(OH)12(OH)0.4(CO3)0.8.4H2O]
 89-0460 (C) - Hydrocalcite, syn - (Mg0.667Al0.333)(OH)2(CO3)0.167(H2O)0.5
 46-1045 (*) - Quartz, syn - SiO2
 41-1451 (*) - Ettringite, syn - Ca6Al2(SO4)3(OH)12.6H2O
 76-0637 (C) - Muscovite 2 ITM 1 - KAl2(Si3Al)O10(OH)2
 38-0568 (I) - Kaolite, silification - Ca3Al2(SiO4)(OH)8

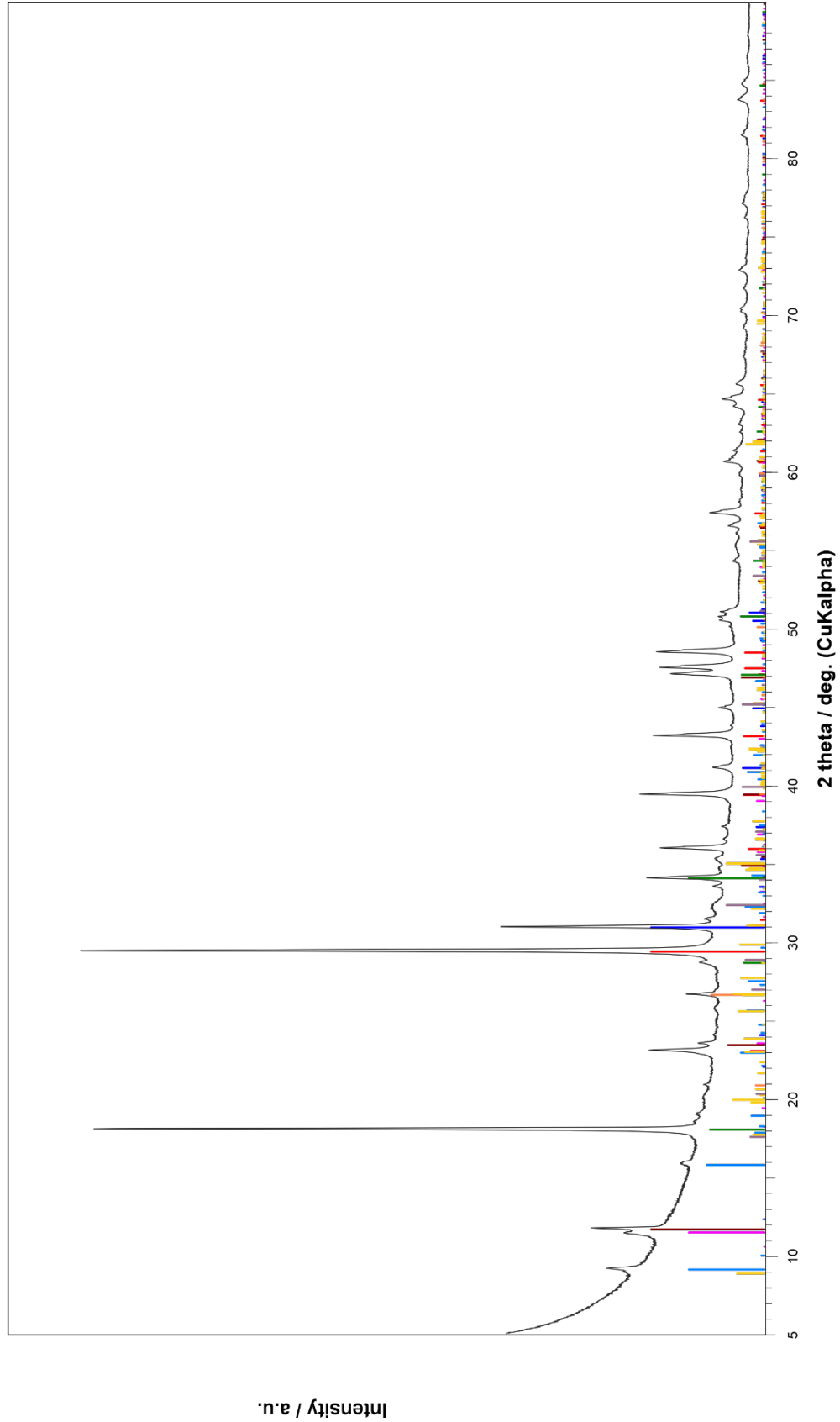


Fig. 75: XRD pattern of the BC12AN1 material

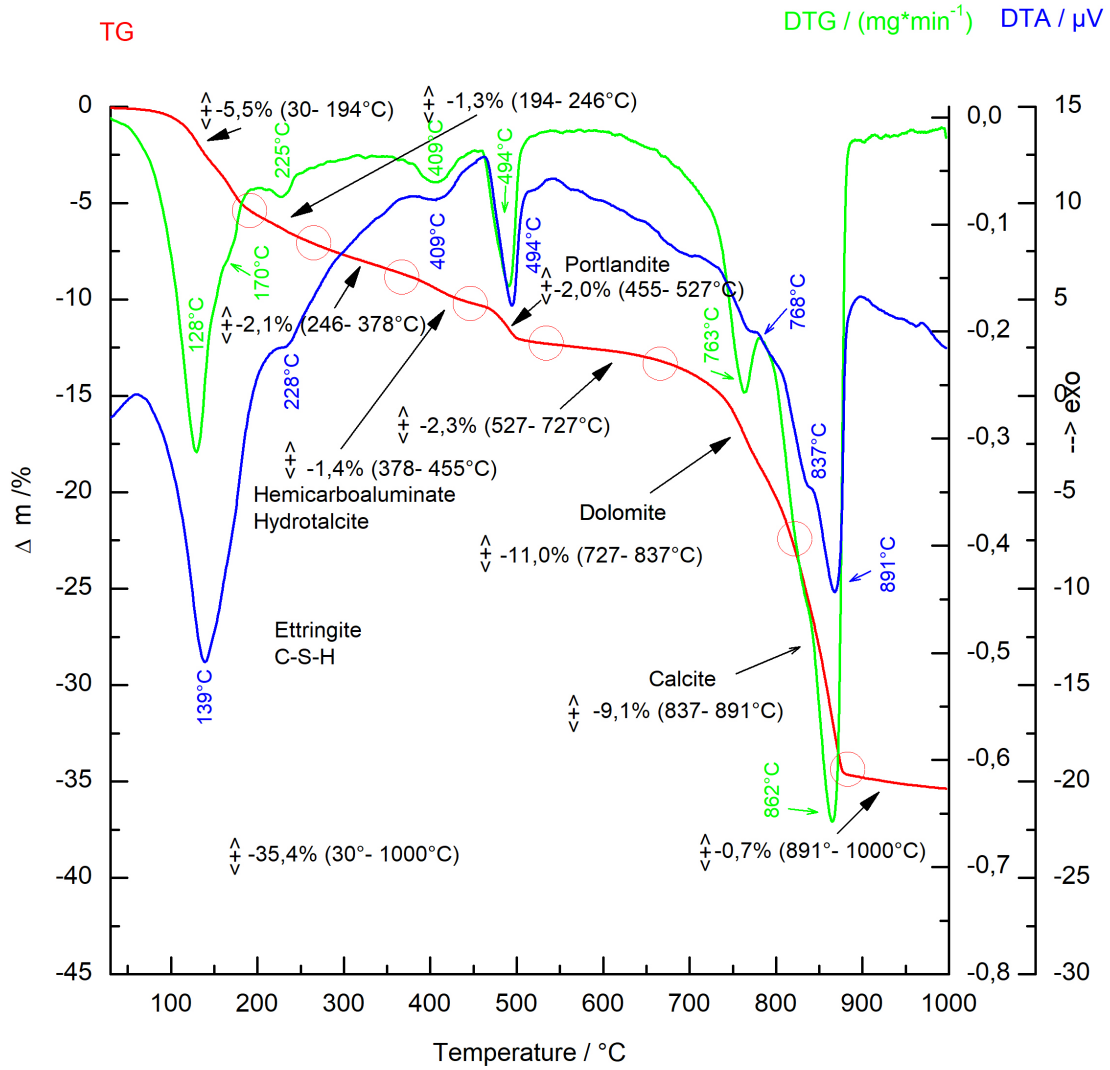


Fig. 76: TGA analysis of the BC22A2 material

UV Vecernik BC22A2
 05-0586 (*) - Calcite, syn - CaCO3
 36-0426 (*) - Dolomite - CaMg(CO3)2
 44-1481 (*) - Portlandite, syn - Ca(OH)2
 76-0637 (C) - Muscovite 2 ITM 1 - KAl2(Si3Al)O10(OH)2
 38-0968 (I) - Kaolite, silification - Ca3Al2(SiO4)(OH)8
 04-018-9909 - Hemihydroxaluminat (CH) - [Ca4Al2(OH)12(OH)0.4(CO3)0.8.4H2O]
 89-0460 (C) - Hydrocalcite, syn - (Mg0.667Al0.333)(OH)2(CO3)0.167(H2O)0.5
 46-1045 (*) - Quartz, syn - SiO2
 41-1451 (*) - Ettringite, syn - Ca6Al2(SO4)3(OH)12.26H2O

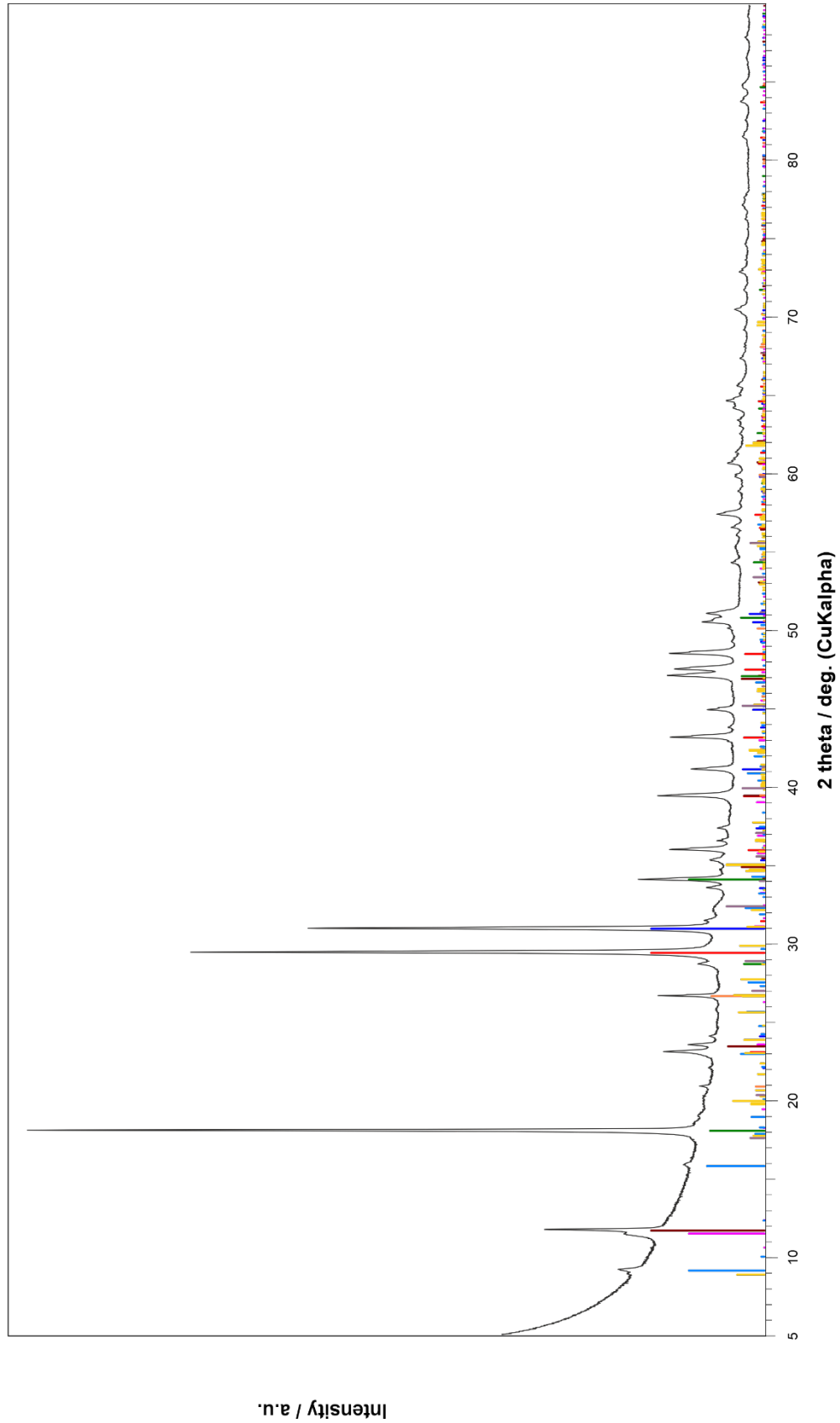


Fig. 77: XRD pattern of the BC22A2 material

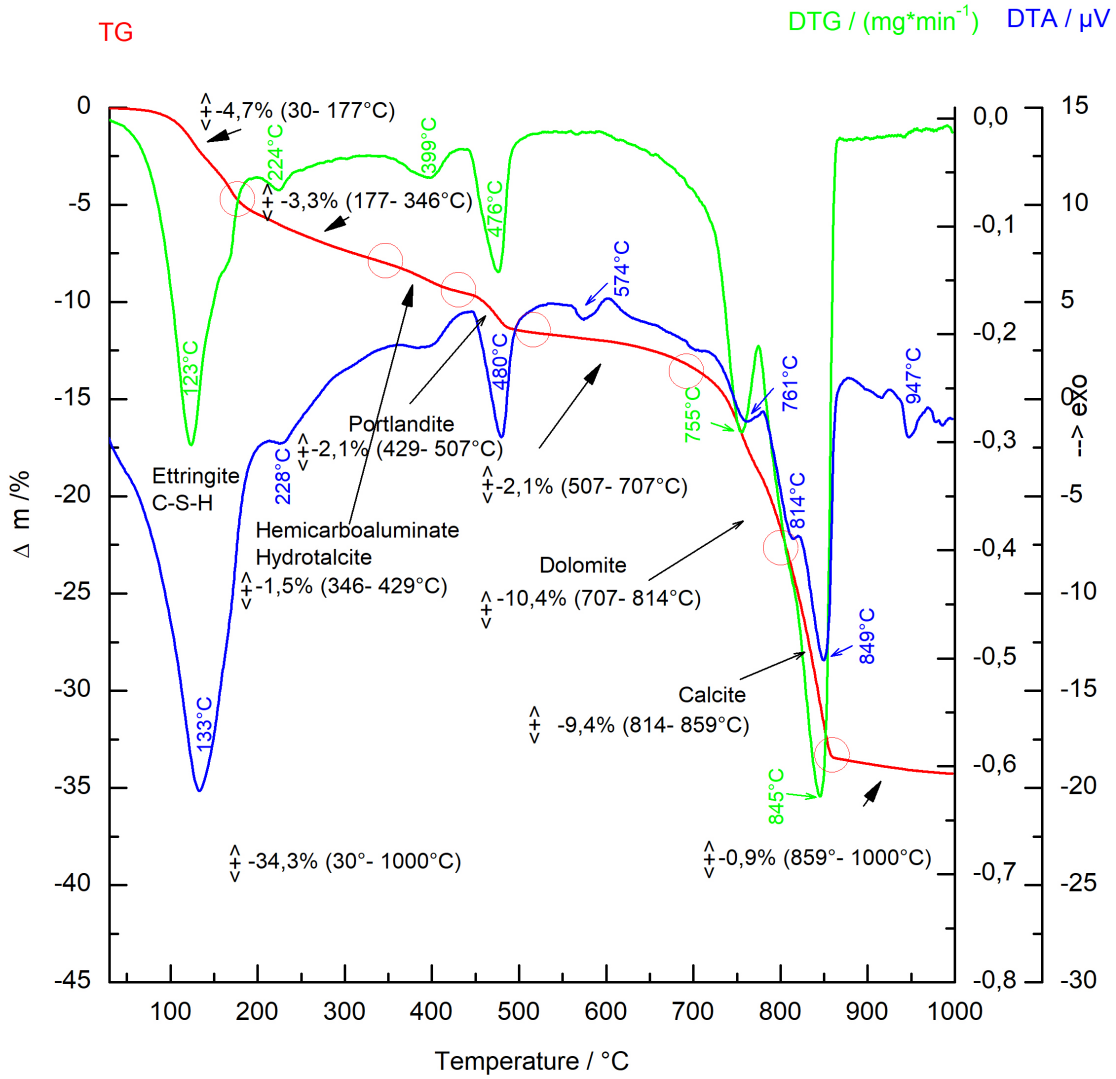


Fig. 78: TGA analysis of the BC22AN2 material

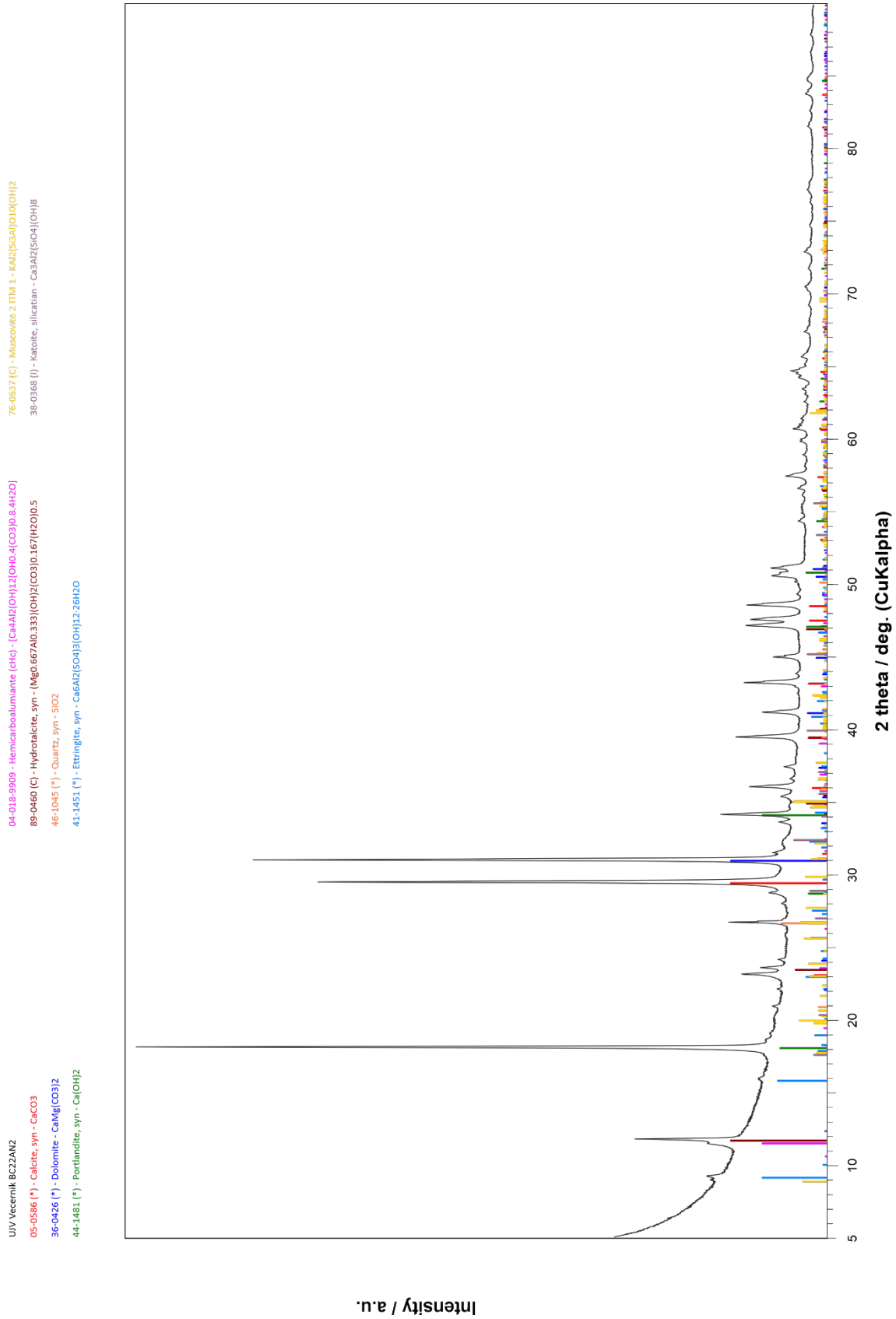


Fig. 79: XRD pattern of the BC22AN2 material

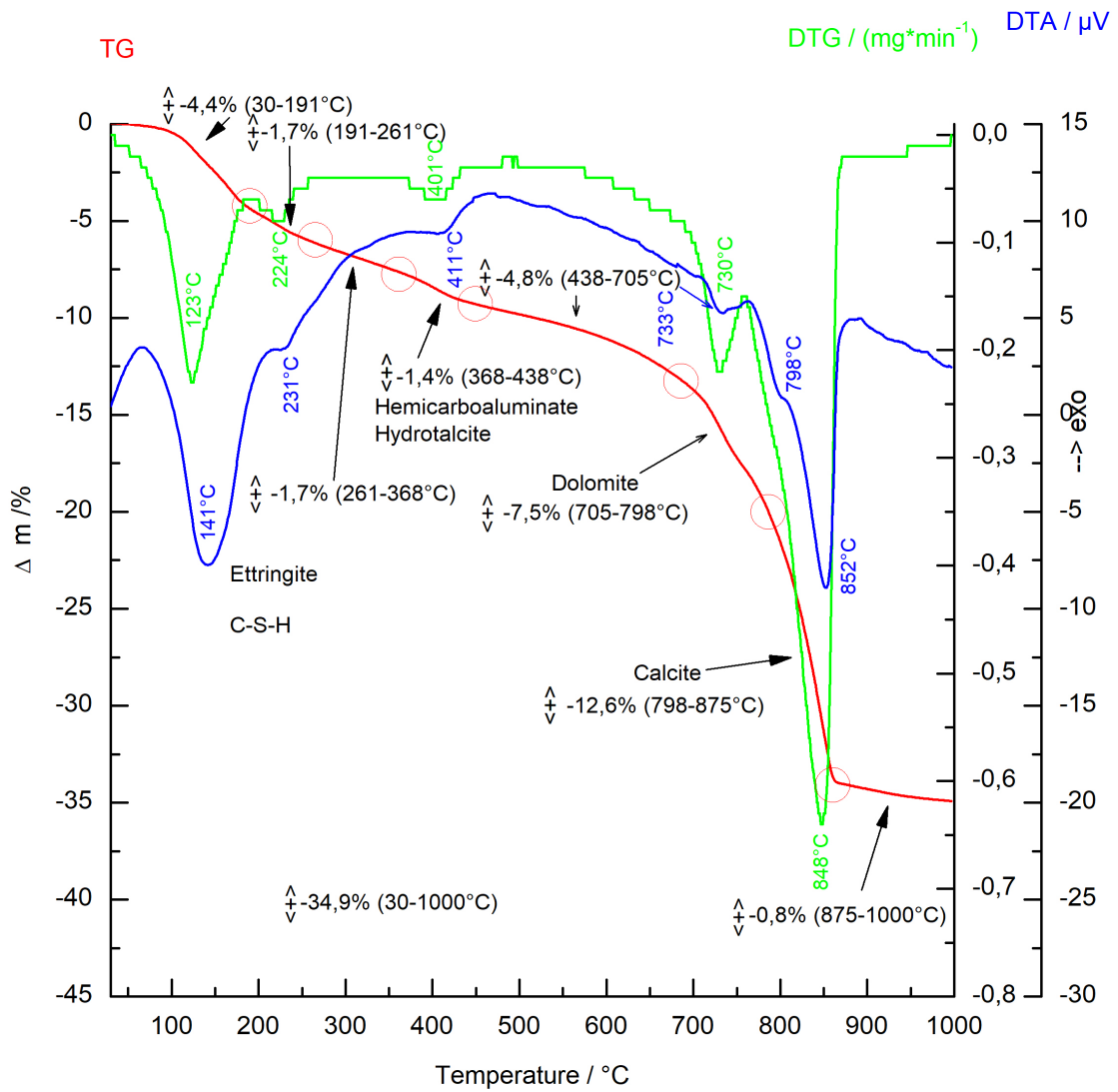


Fig. 80: TGA analysis of the 113B material

UV Vecernik CIM113B
 05-0586 (*) - Calcite, syn - CaCO3
 36-0426 (*) - Dolomite - CaMg(CO3)2
 44-1481 (*) - Portlandite, syn - Ca(OH)2
 04-018-9909 - Hemihydroaluminat (CH) - [Ca4Al2(OH)12(OH)0.4(CO3)0.8.4H2O]
 89-0460 (C) - Hydrocalcite, syn - (Mg0.667Al0.333)(OH)2(CO3)0.167(H2O)0.5
 46-1045 (*) - Quartz, syn - SiO2
 41-1451 (*) - Ettringite, syn - Ca6Al2(SO4)3(OH)12.26H2O
 76-0637 (C) - Muscovite 2 ITM 1 - KAl2(Si3Al)O10(OH)2
 38-0568 (I) - Kaolite, silification - Ca3Al2(SiO4)(OH)8

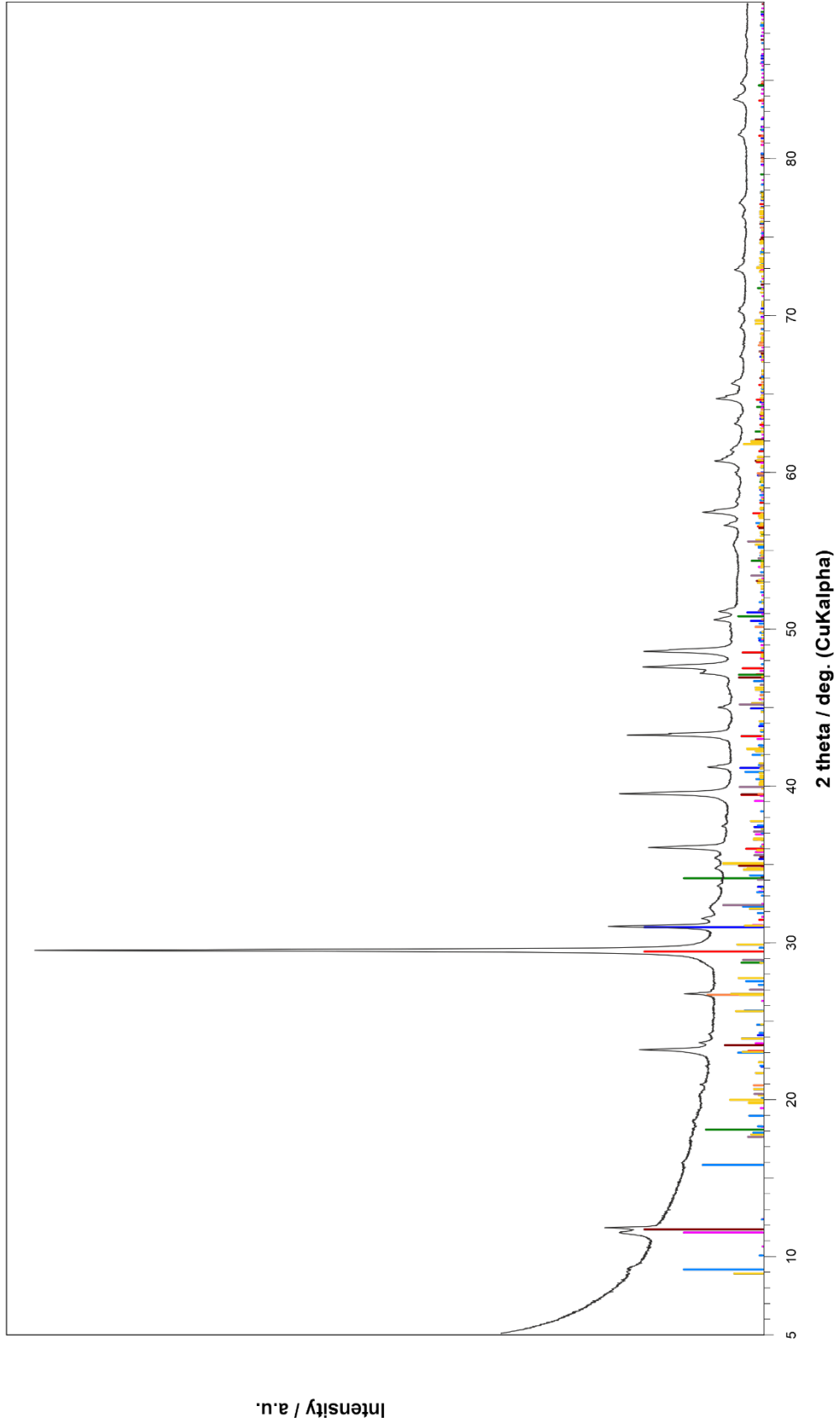


Fig. 81: XRD pattern of the 113B material

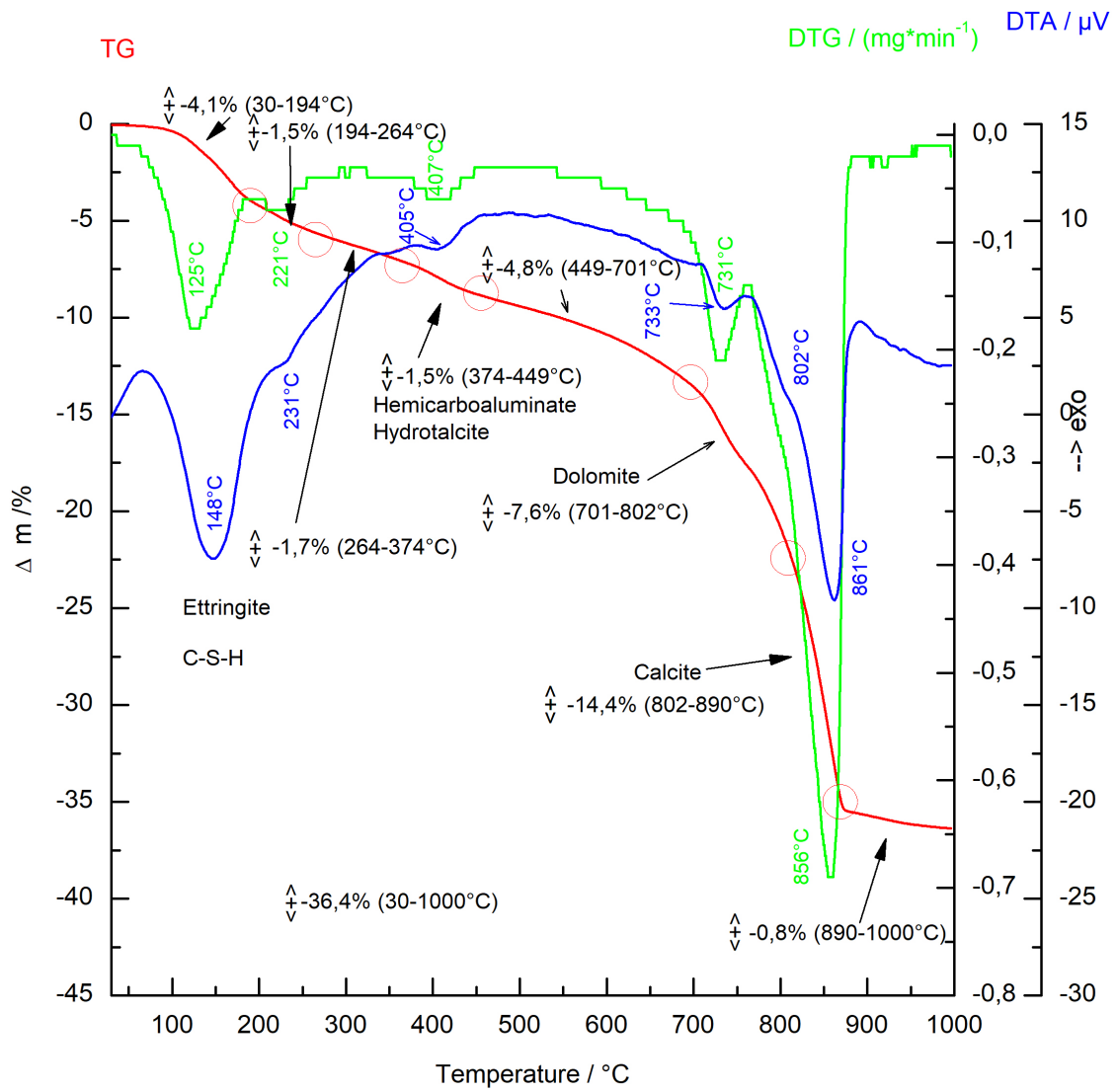


Fig. 82: TGA analysis of the 113L material

UV Vecernik CIM113L
 05-0586 (*) - Calcite, syn - CaCO3
 36-0426 (*) - Dolomite - CaMg(CO3)2
 44-1481 (*) - Portlandite, syn - Ca(OH)2
 04-018-9909 - Hemihydroaluminat (CH) - [Ca4Al2(OH)12(OH)0.4(CO3)0.8.4H2O]
 89-0460 (C) - Hydrocalcite, syn - (Mg0.667Al0.333)(OH)2(CO3)0.167(H2O)0.5
 46-1045 (*) - Quartz, syn - SiO2
 41-1451 (*) - Ettringite, syn - Ca6Al2(SO4)3(OH)12.26H2O
 76-0637 (C) - Muscovite 2 ITM 1 - KAl2(Si3Al)O10(OH)2
 38-0568 (I) - Kaolite, silification - Ca3Al2(SiO4)(OH)8

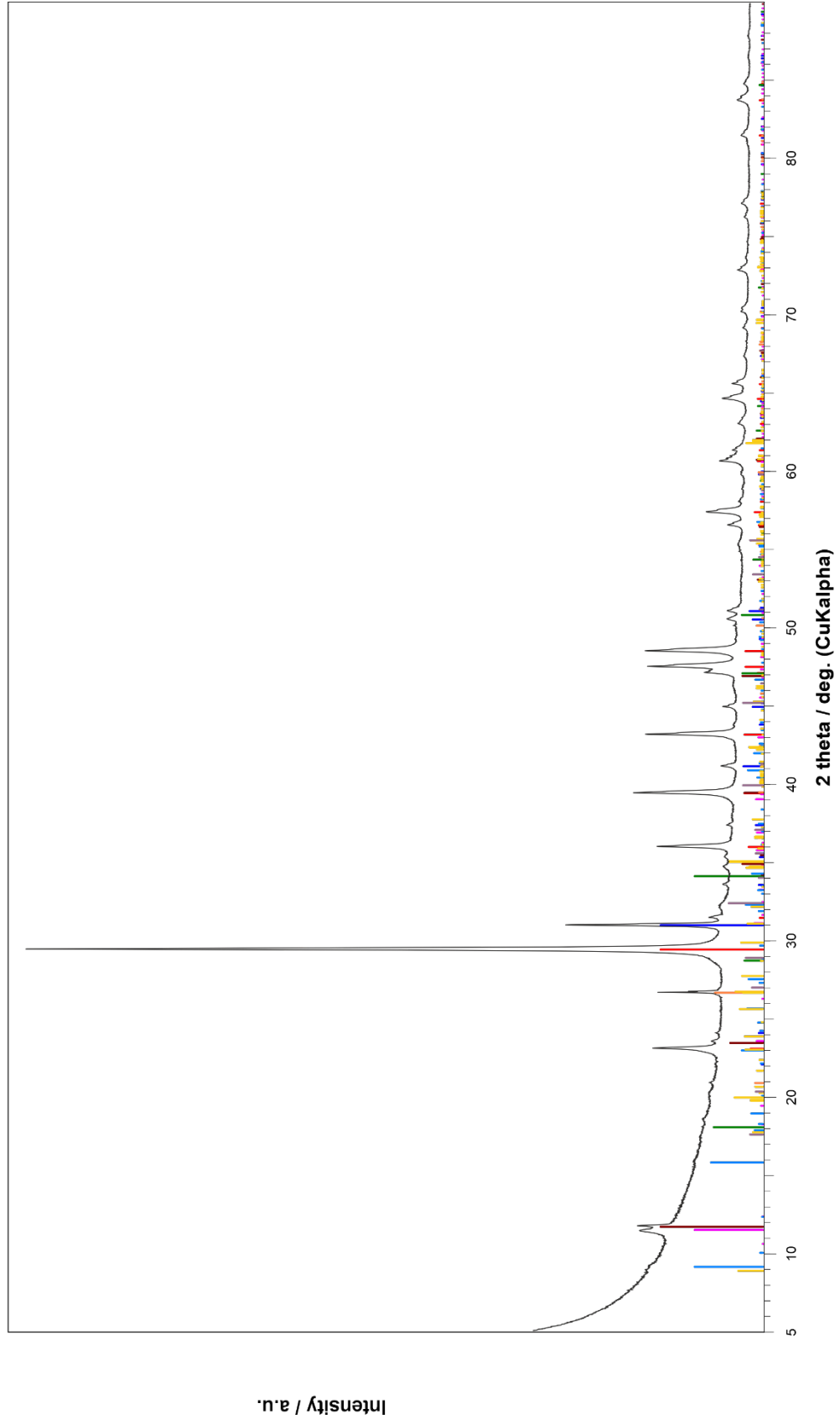


Fig. 83: XRD pattern of the 113L material

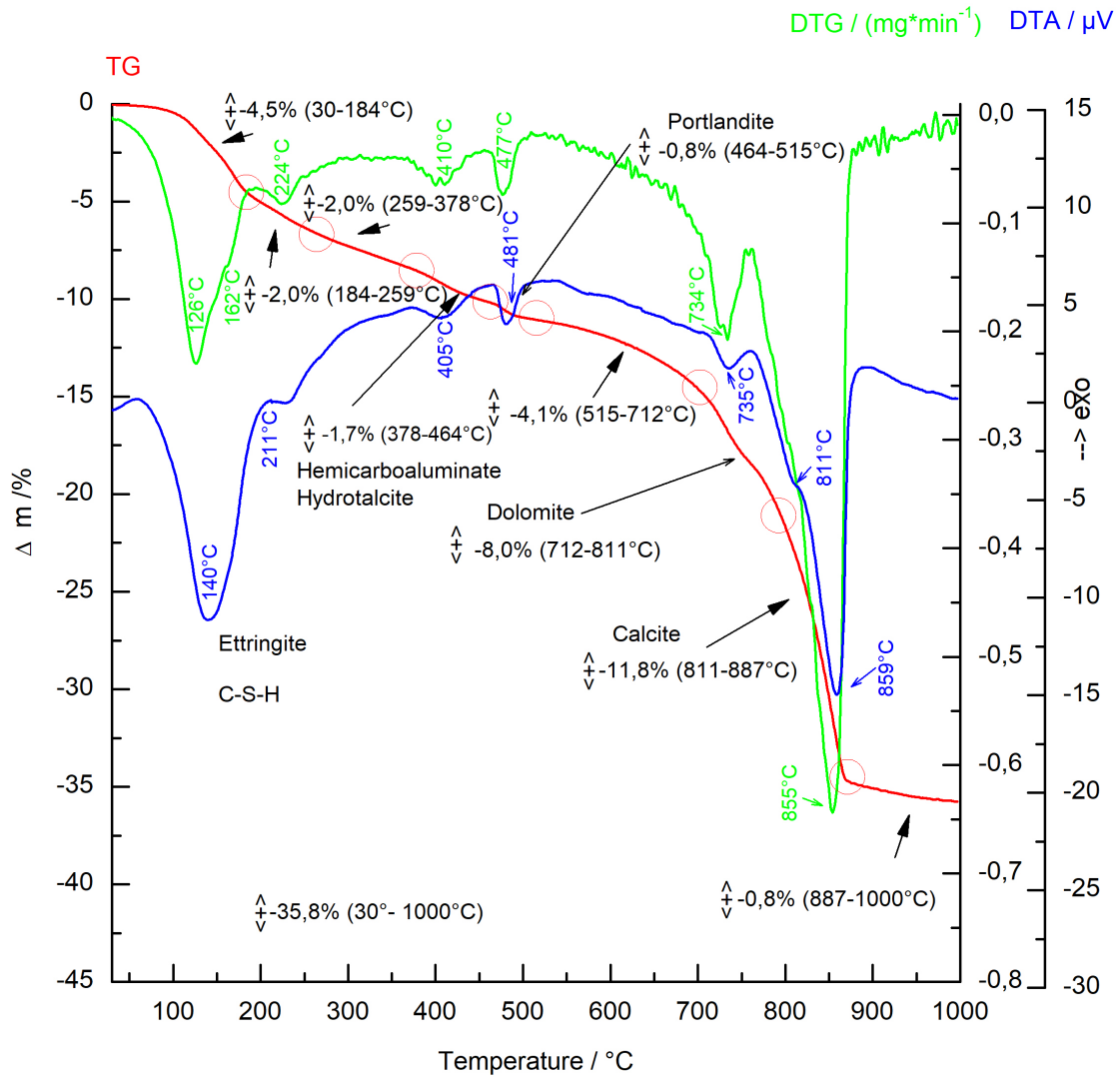


Fig. 84: TGA analysis of the 115C material

- UIV Vecernik CIM115C
- 05-0586 (*) - Calcite, syn - CaCO3
- 36-0426 (*) - Dolomite - CaMg(CO3)2
- 44-1481 (*) - Portlandite, syn - Ca(OH)2
- 04-018-9909 - Hemihydroaluminat (CH) - [Ca4Al2(OH)12(OH)0.4(CO3)0.8.4H2O]
- 89-0460 (C) - Hydrocalcite, syn - (Mg0.667Al0.333)(OH)2(CO3)0.167(H2O)0.5
- 46-1045 (*) - Quartz, syn - SiO2
- 41-1451 (*) - Ettringite, syn - Ca6Al2(SO4)3(OH)12.26H2O
- 76-0637 (C) - Muscovite 2 ITM 1 - KAl2(SiEA)10(OH)2
- 38-0568 (I) - Kaolite, silification - Ca3Al2(SiO4)(OH)8

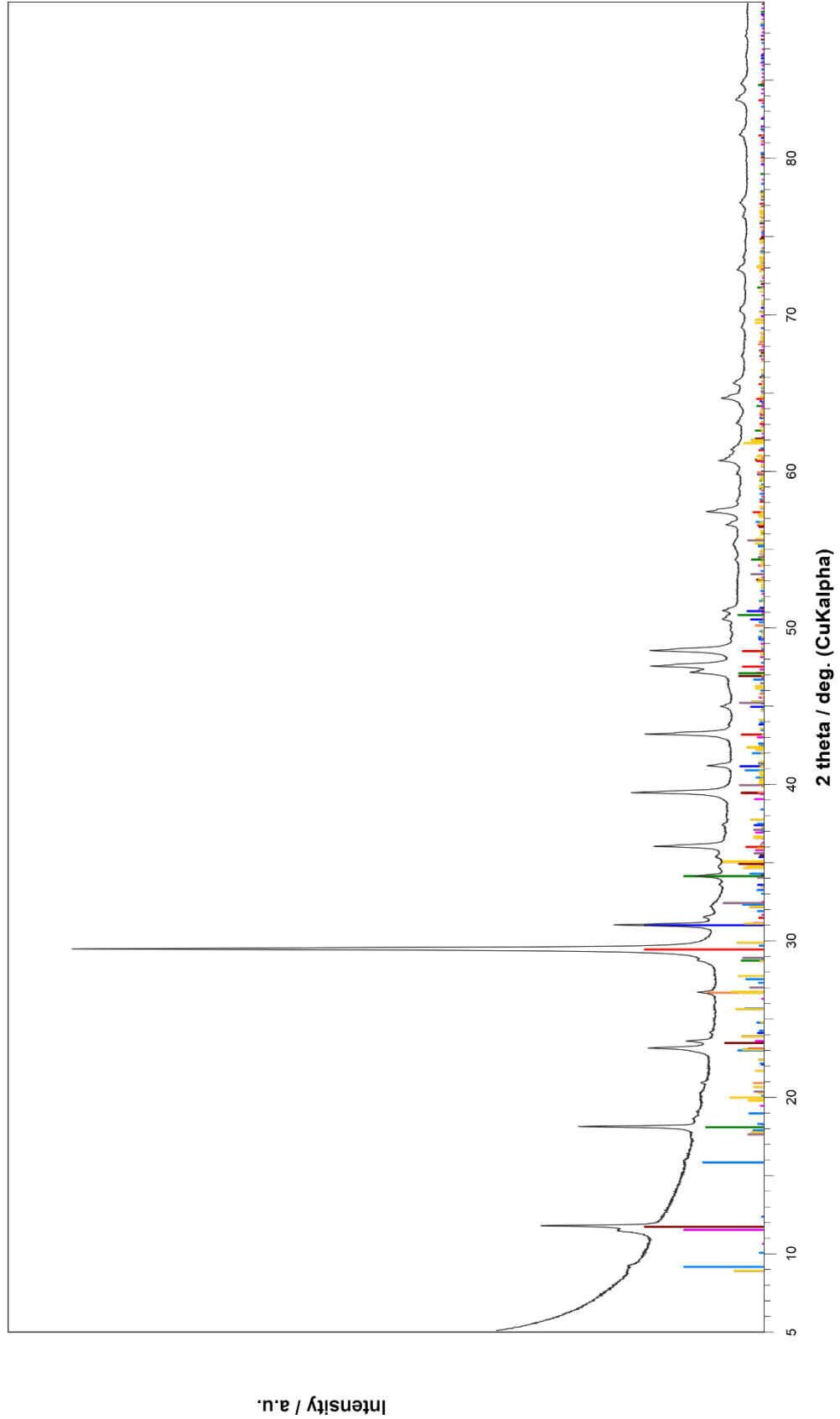


Fig. 85: XRD pattern of the 115C material

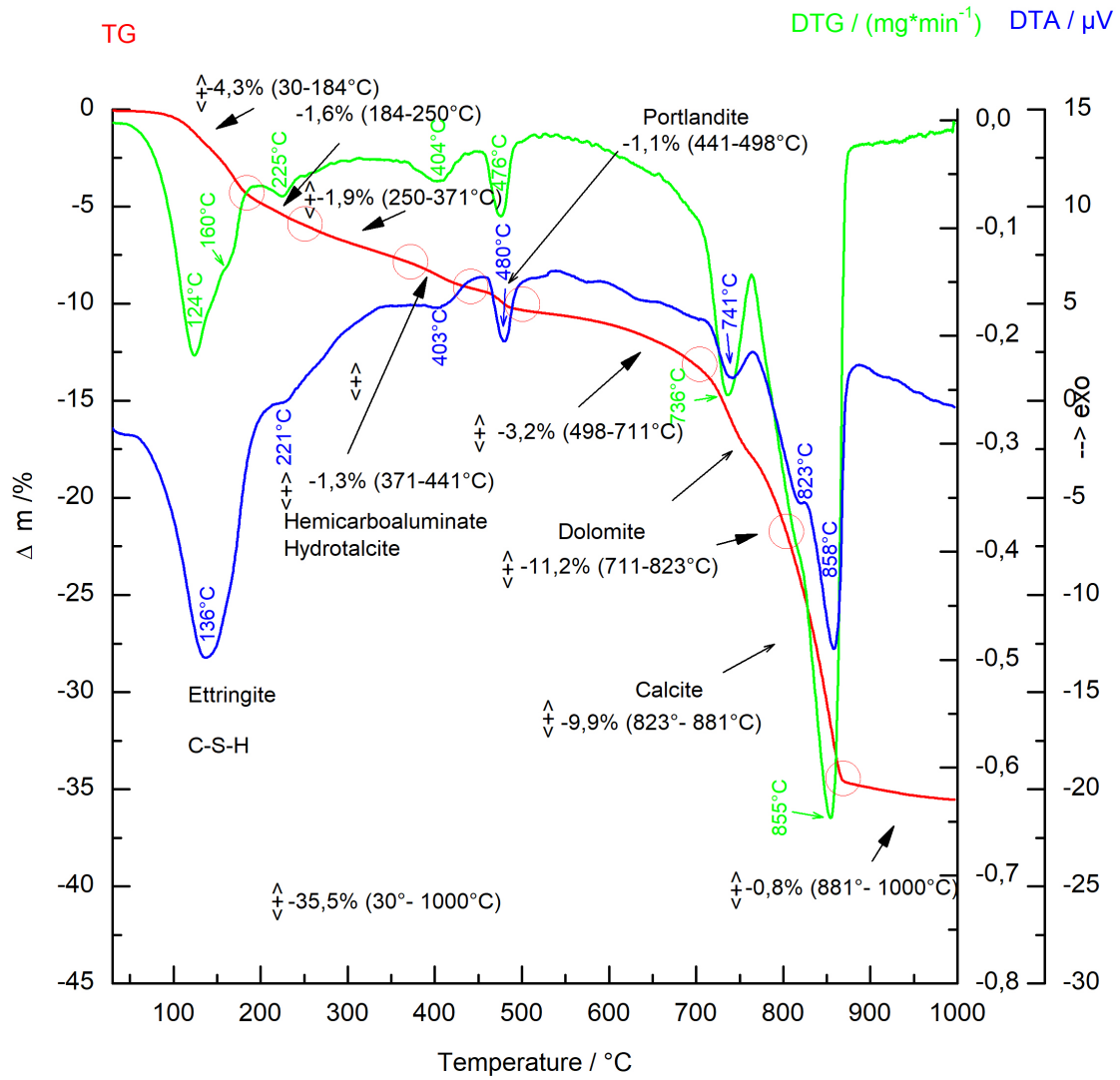


Fig. 86: TGA analysis of the 211C material

UV Vecernik CIM211C
 05-0586 (*) - Calcite, syn - CaCO₃
 36-0426 (*) - Dolomite - CaMg(CO₃)₂
 44-1481 (*) - Portlandite, syn - Ca(OH)₂
 04-018-9909 - Hemicarboaluminate (chc) - [Ca₄Al₂(OH)₁₂(OH)_{0.4}(CO₃)_{0.8}.4H₂O]
 89-0460 (C) - Hydrocalcite, syn - (Mg_{0.667}Al_{0.333})(OH)₂(CO₃)_{0.167}(H₂O)_{0.5}
 46-1045 (*) - Quartz, syn - SiO₂
 41-1451 (*) - Ettringite, syn - Ca₆A₂(SO₄)₃(OH)₁₂.26H₂O
 76-0637 (C) - Muscovite 2 ITM 1 - KAl₂(Si₃Al)O₁₀(OH)₂
 38-0568 (I) - Kaolite, silification - Ca₃A₂(SiO₄)(OH)₈

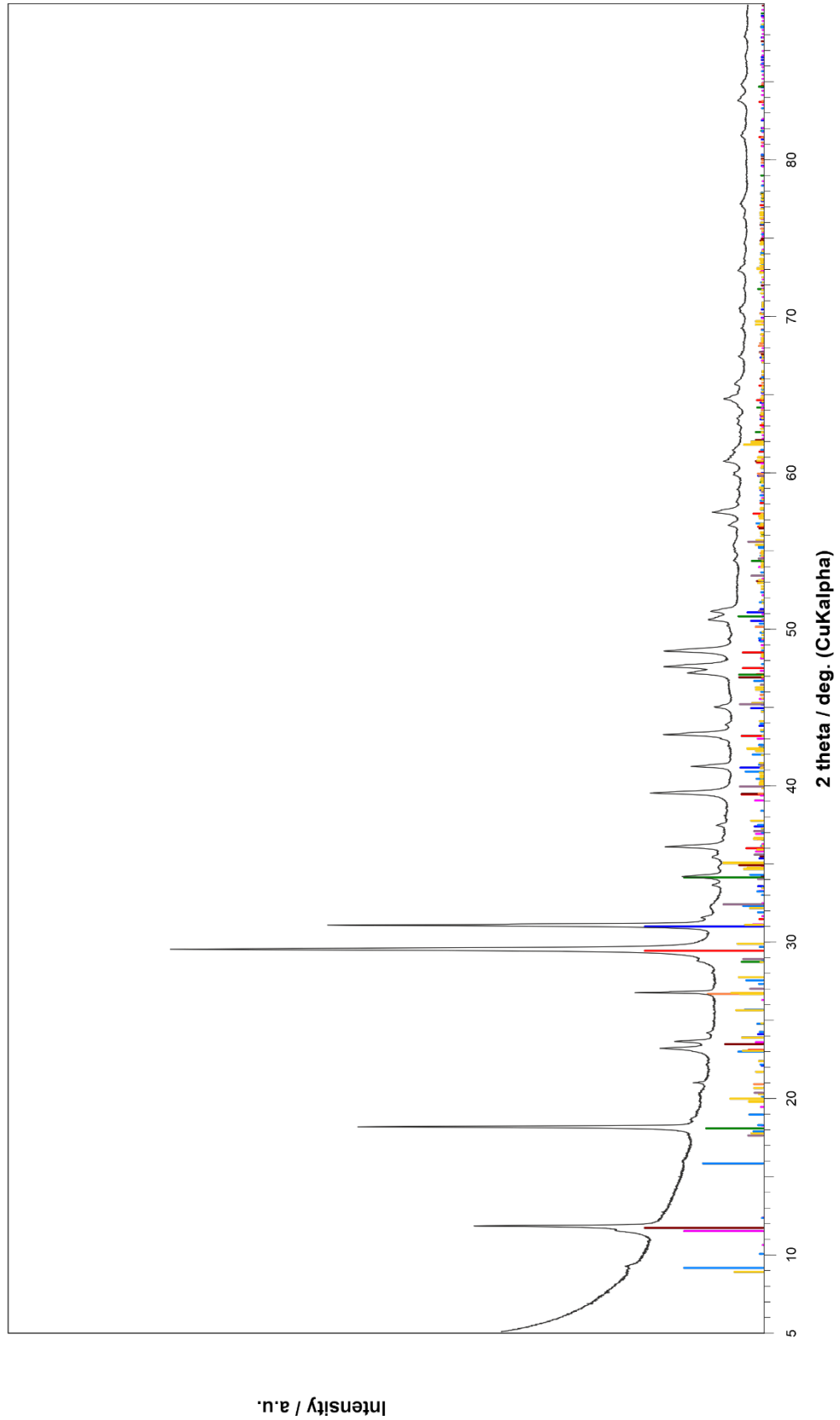


Fig. 87: XRD pattern of the 211C material

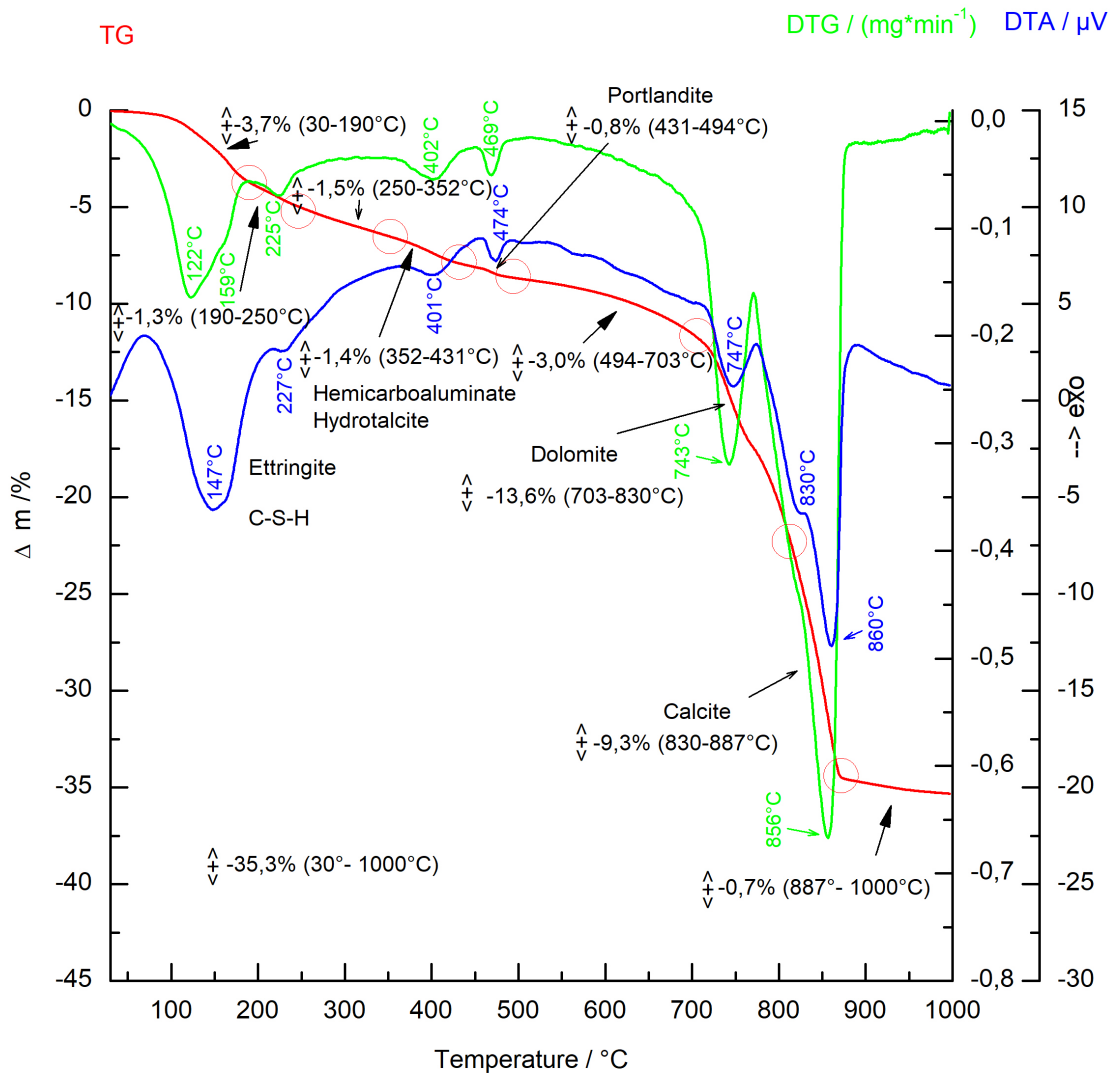


Fig. 88: TGA analysis of the 219B material

UV Vecernik CIM219B
 05-0586 (*) - Calcite, syn - CaCO3
 36-0426 (*) - Dolomite - CaMg(CO3)2
 44-1481 (*) - Portlandite, syn - Ca(OH)2
 04-018-9909 - Hemicarboaluminate (chc) - [Ca4Al2(OH)12(OH)0.4(CO3)0.8.4H2O]
 89-0460 (C) - Hydrocalcite, syn - (Mg0.667Al0.333)(OH)2(CO3)0.167(H2O)0.5
 46-1045 (*) - Quartz, syn - SiO2
 41-1451 (*) - Ettringite, syn - Ca6Al2(SO4)3(OH)12.26H2O
 76-0637 (C) - Muscovite 2 ITM 1 - KAl2(Si3Al)O10(OH)2
 38-0568 (I) - Kaolite, silification - Ca3Al2(SiO4)(OH)8

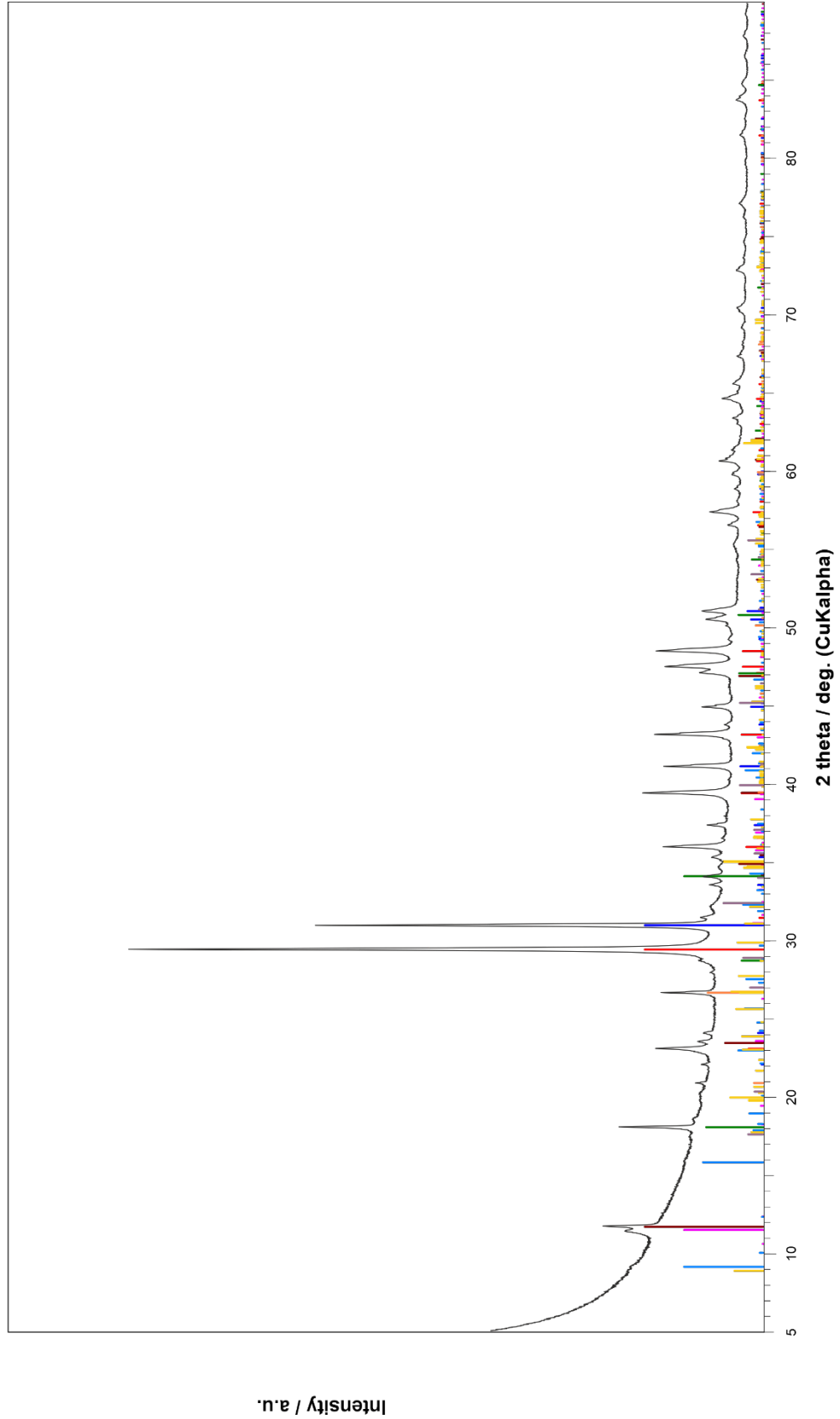


Fig. 89: XRD pattern of the 219B material

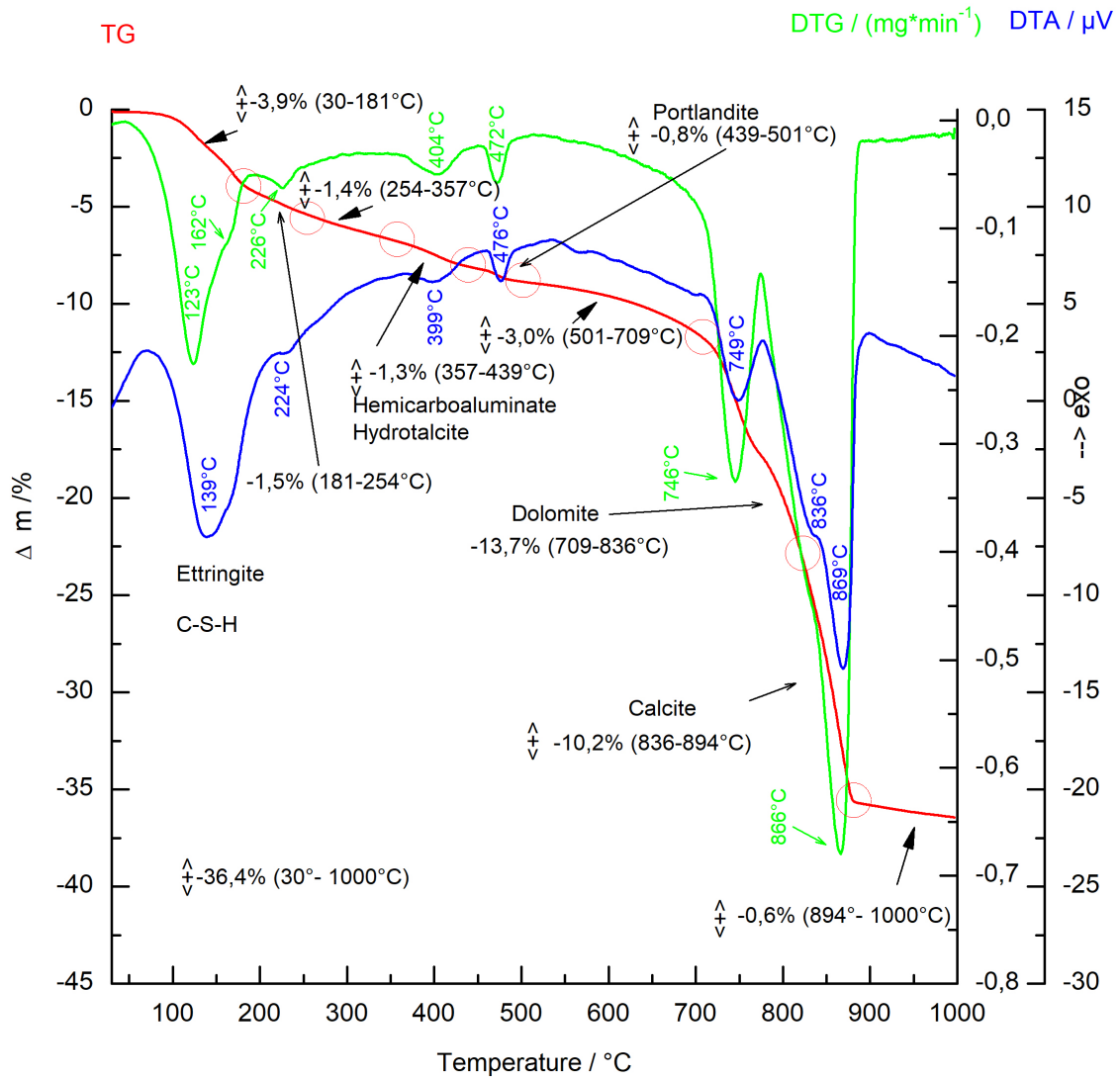


Fig. 90: TGA analysis of the 219L material

UV Vecernik CIM219L
 05-0586 (*) - Calcite, syn - CaCO3
 36-0426 (*) - Dolomite - CaMg(CO3)2
 44-1481 (*) - Portlandite, syn - Ca(OH)2
 04-018-9909 - Hemihydroaluminat (CH) - [Ca4Al2(OH)12(OH)0.4(CO3)0.8.4H2O]
 89-0460 (C) - Hydrocalcite, syn - (Mg0.667Al0.333)(OH)2(CO3)0.167(H2O)0.5
 46-1045 (*) - Quartz, syn - SiO2
 41-1451 (*) - Ettringite, syn - Ca6Al2(SO4)3(OH)12.26H2O
 76-0637 (C) - Muscovite 2 ITM 1 - KAl2(Si3Al)O10(OH)2
 38-0568 (I) - Kaolite, silification - Ca3Al2(SiO4)(OH)8

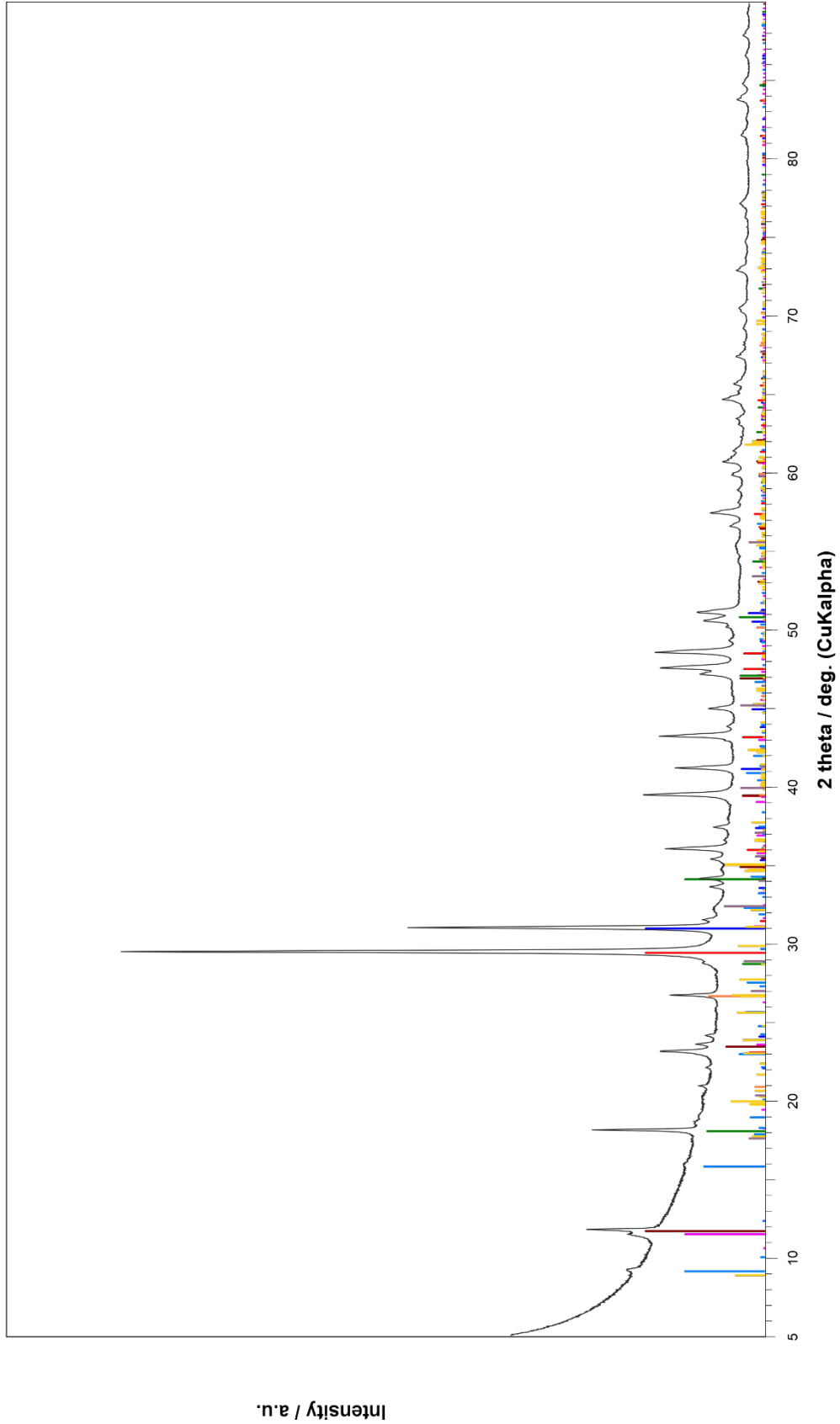


Fig. 91: XRD pattern of the 219L material

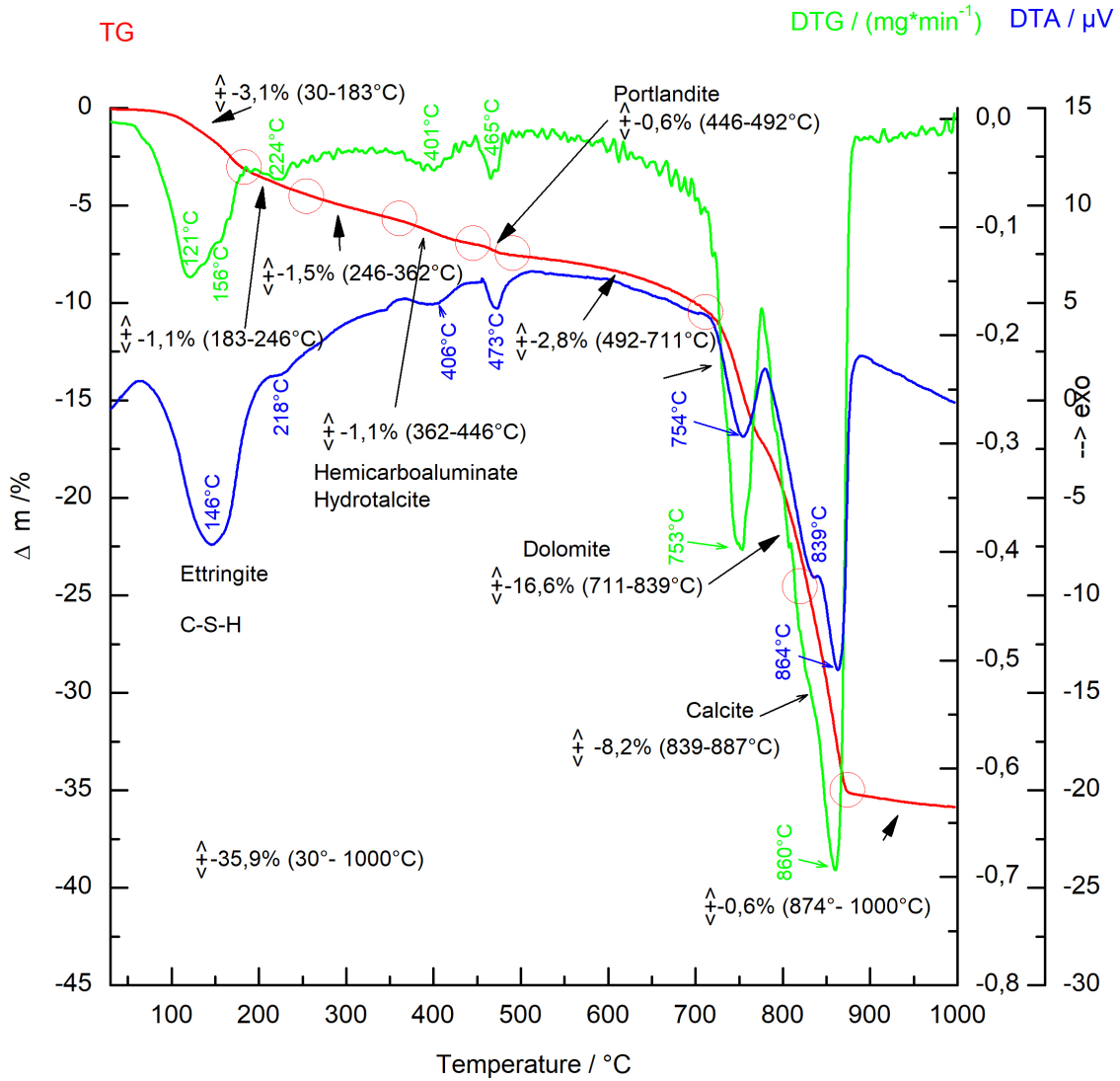


Fig. 92: TGA analysis of the 265B material

UV Vecernik CIM265B
 05-0586 (*) - Calcite, syn - CaCO3
 36-0426 (*) - Dolomite - CaMg(CO3)2
 44-1481 (*) - Portlandite, syn - Ca(OH)2
 04-018-9909 - Hemihydroaluminat (CH) - [Ca4Al2(OH)12(OH)0.4(CO3)0.8.4H2O]
 89-0460 (C) - Hydrocalcite, syn - (Mg0.667Al0.333)(OH)2(CO3)0.167(H2O)0.5
 46-1045 (*) - Quartz, syn - SiO2
 41-1451 (*) - Ettringite, syn - Ca6Al2(SO4)3(OH)12.26H2O
 76-0637 (C) - Muscovite 2 ITM 1 - KAl2(Si3Al)O10(OH)2
 38-0568 (I) - Kaolite, silification - Ca3Al2(SiO4)(OH)8

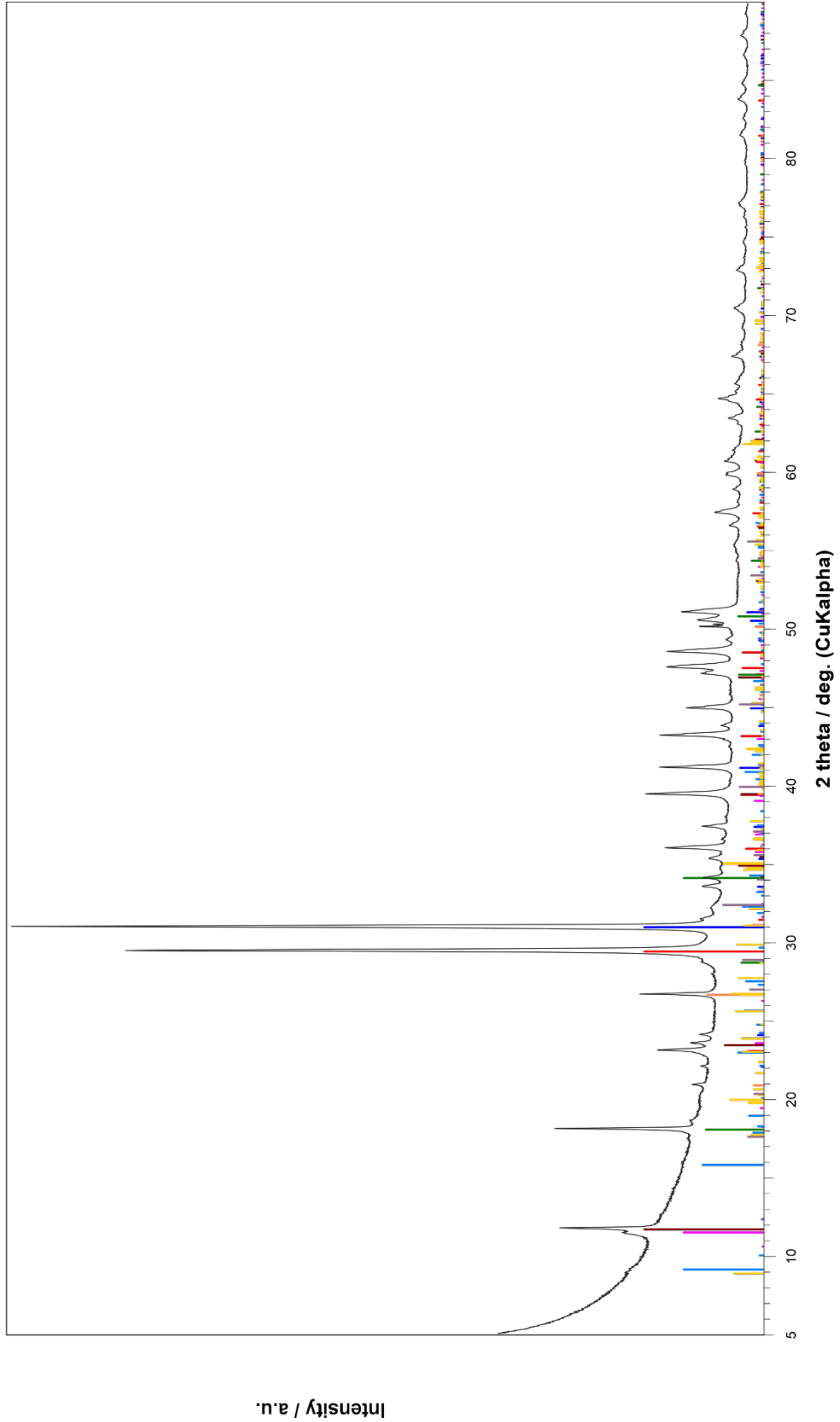


Fig. 93: XRD pattern of the 265B material

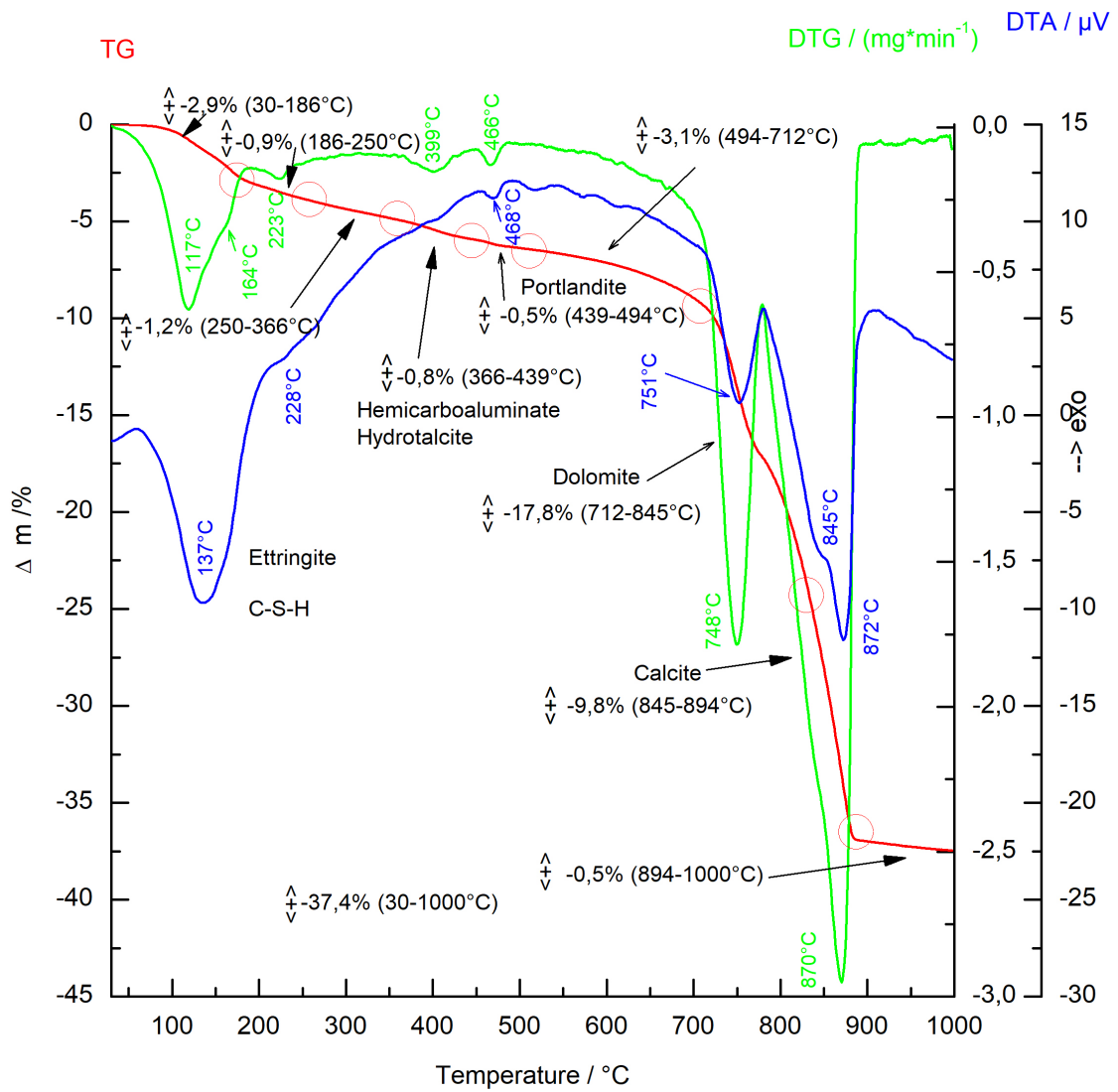


Fig. 94: TGA analysis of the 265L material

UV Vecernik CIM265L
 05-0586 (*) - Calcite, syn - CaCO3
 36-0426 (*) - Dolomite - CaMg(CO3)2
 44-1481 (*) - Portlandite, syn - Ca(OH)2
 04-018-9909 - Hemihydroaluminat (hhc) - [Ca4Al2(OH)12(OH)0.4(CO3)0.8.4H2O]
 89-0460 (C) - Hydrocalcite, syn - (Mg0.667Al0.333)(OH)2(CO3)0.167(H2O)0.5
 46-1045 (*) - Quartz, syn - SiO2
 41-1451 (*) - Ettringite, syn - Ca6Al2(SO4)3(OH)12.26H2O
 76-0637 (C) - Muscovite 2 ITM 1 - KAl2(Si3Al)O10(OH)2
 38-0568 (I) - Kaolite, silification - Ca3Al2(SiO4)(OH)8

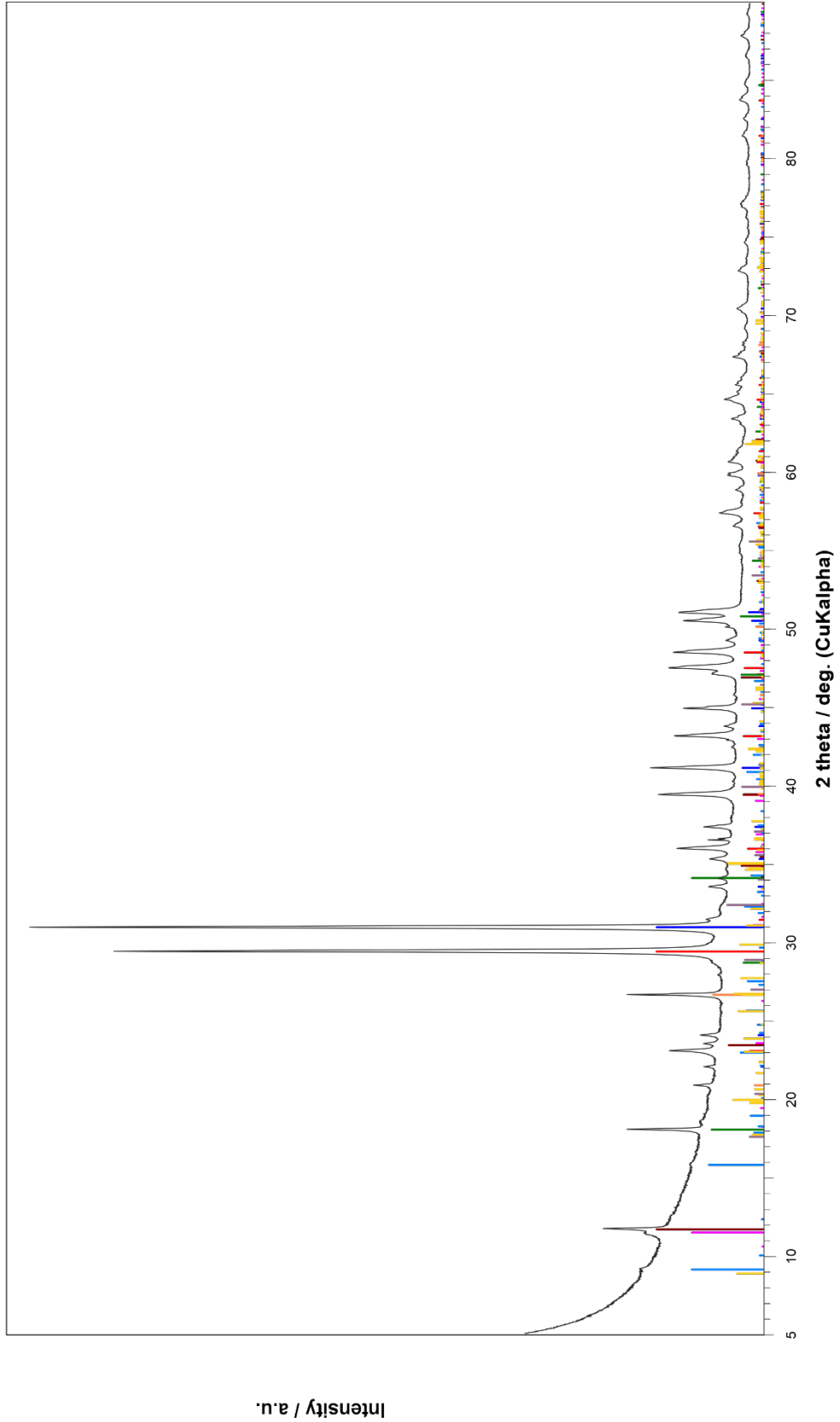


Fig. 95: XRD pattern of the 265L material

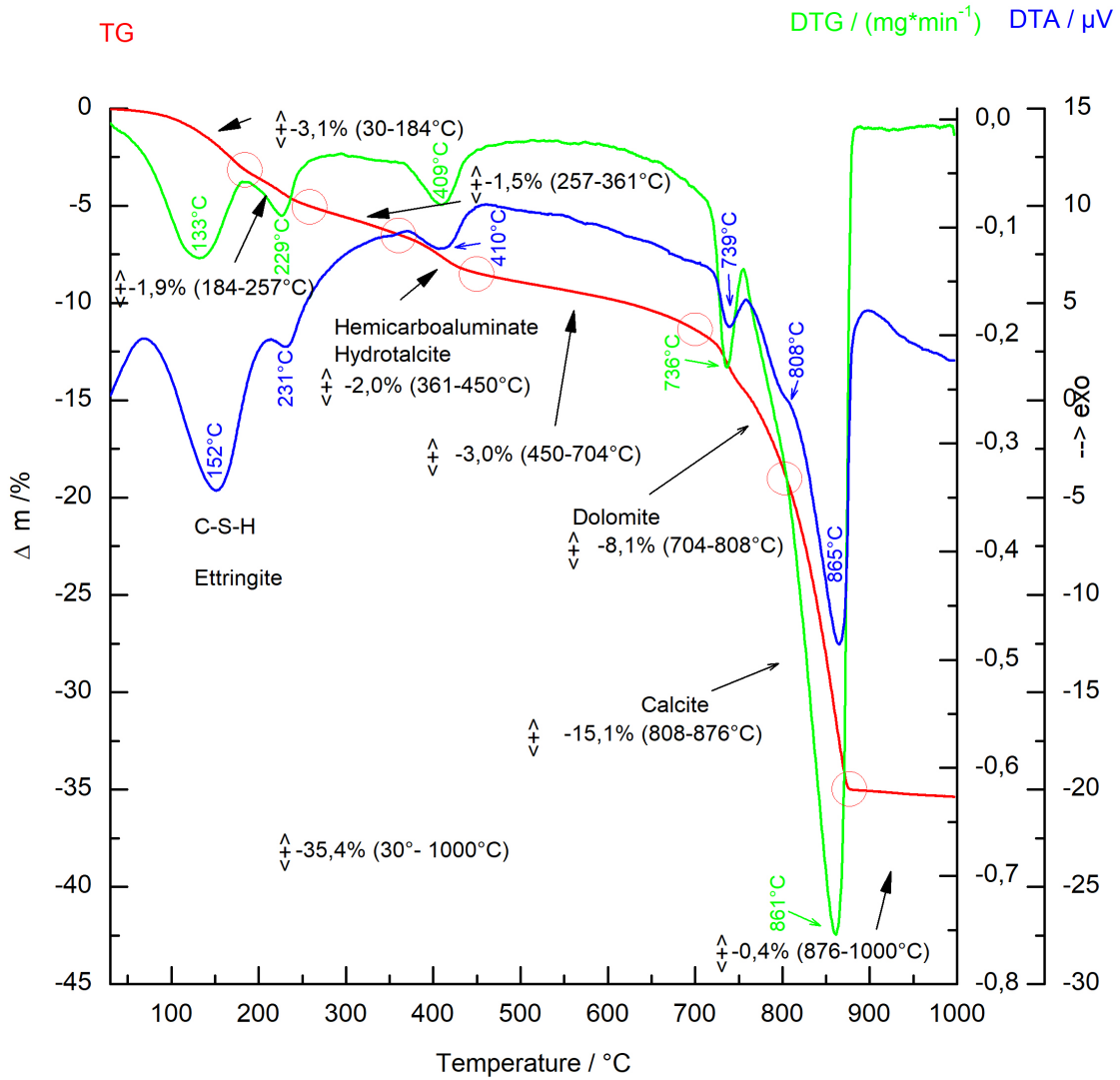


Fig. 96: TGA analysis of the 14A-A material

UV Vecernik CIM14A-A
 05-0586 (*) - Calcite, syn - CaCO3
 36-0426 (*) - Dolomite - CaMg(CO3)2
 44-1481 (*) - Portlandite, syn - Ca(OH)2
 04-018-9909 - Hemihydroaluminat (hhc) - [Ca4Al2(OH)12(OH)0.4(CO3)0.8.4H2O]
 89-0460 (C) - Hydrocalcite, syn - (Mg0.667Al0.333)(OH)2(CO3)0.167(H2O)0.5
 46-1045 (*) - Quartz, syn - SiO2
 41-1451 (*) - Ettringite, syn - Ca6Al2(SO4)3(OH)12.26H2O
 76-0637 (C) - Muscovite 2 ITM 1 - KAl2(Si3Al)O10(OH)2
 38-0568 (I) - Kaolite, silification - Ca3Al2(SiO4)(OH)8

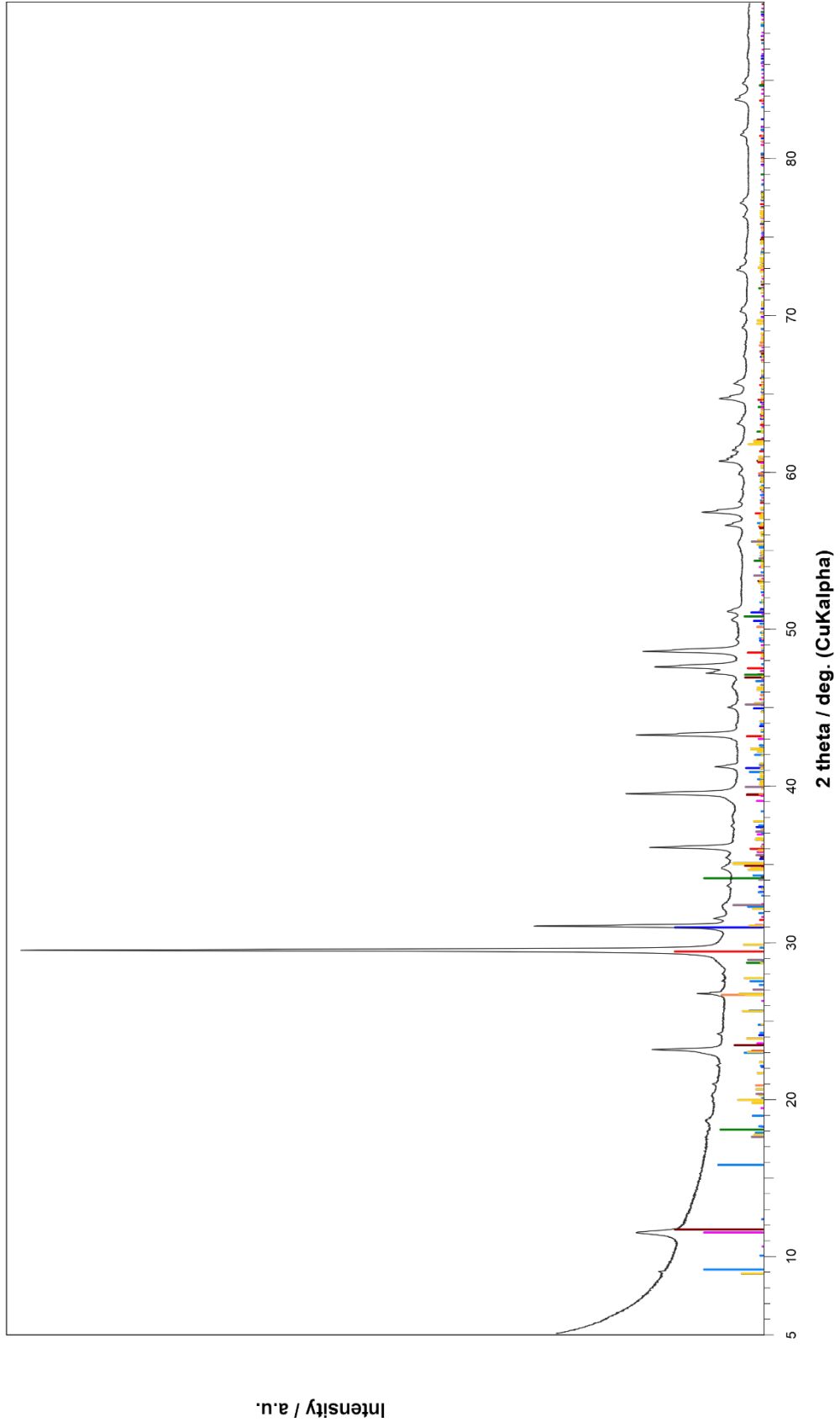


Fig. 97: XRD pattern of the 14A-A material

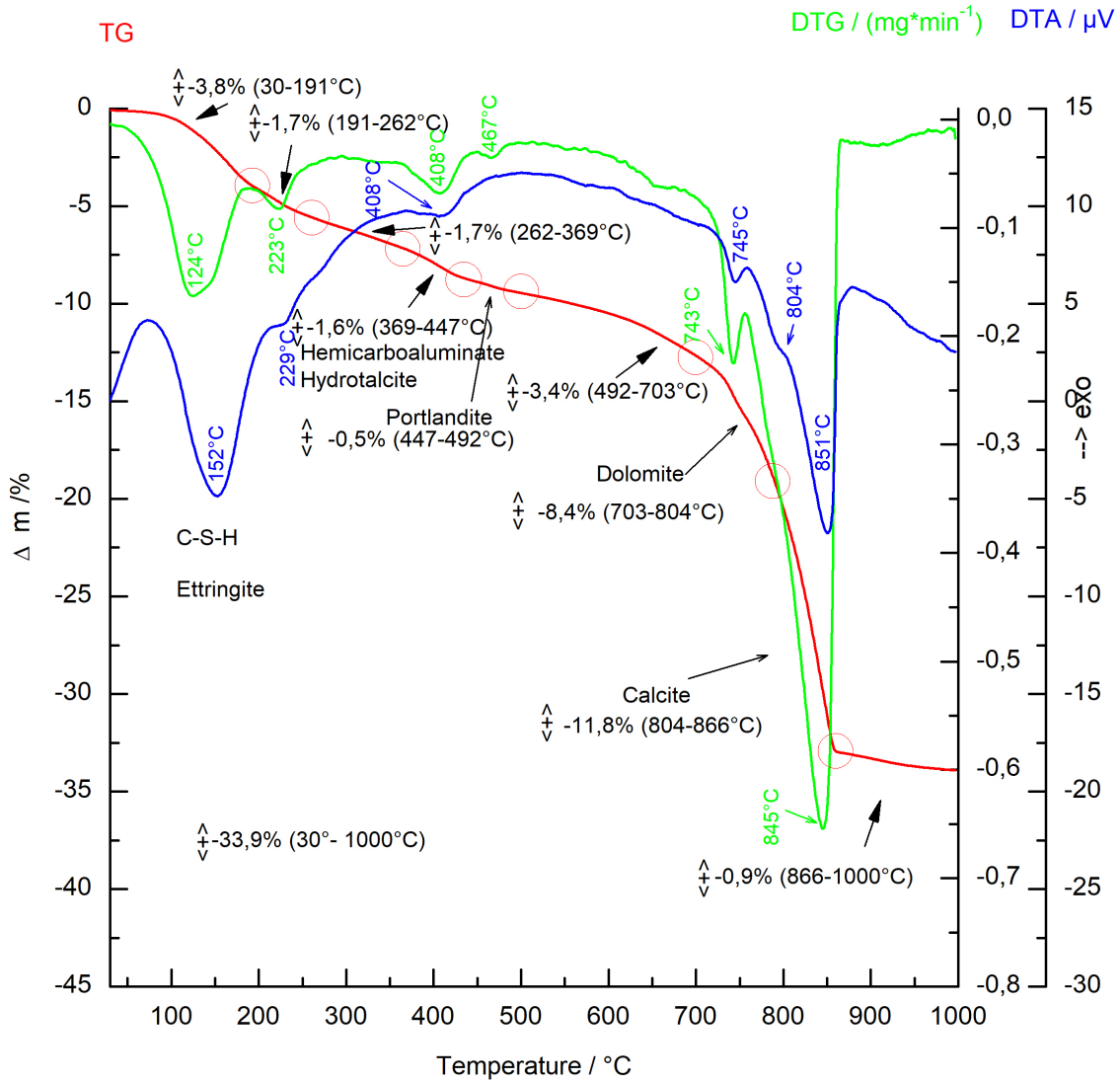


Fig. 98: TGA analysis of the 14A-C material

UV Vecernik CIM14A-C
 05-0586 (*) - Calcite, syn - CaCO₃
 36-0426 (*) - Dolomite - CaMg(CO₃)₂
 44-1481 (*) - Portlandite, syn - Ca(OH)₂
 04-018-9909 - Hemihydroaluminat (CH) - [Ca₄Al₂(OH)₁₂(OH)_{0.4}(CO₃)_{0.8}.4H₂O]
 89-0460 (C) - Hydrocalcite, syn - (Mg_{0.667}Al_{0.333})(OH)₂(CO₃)_{0.167}(H₂O)_{0.5}
 46-1045 (*) - Quartz, syn - SiO₂
 41-1451 (*) - Ettringite, syn - Ca₆A₂(SO₄)₃(OH)₁₂.26H₂O
 76-0637 (C) - Muscovite 2 ITM 1 - KAl₂(Si₃Al)O₁₀(OH)₂
 38-0568 (I) - Kaolite, silification - Ca₃A₂(SiO₄)(OH)₈

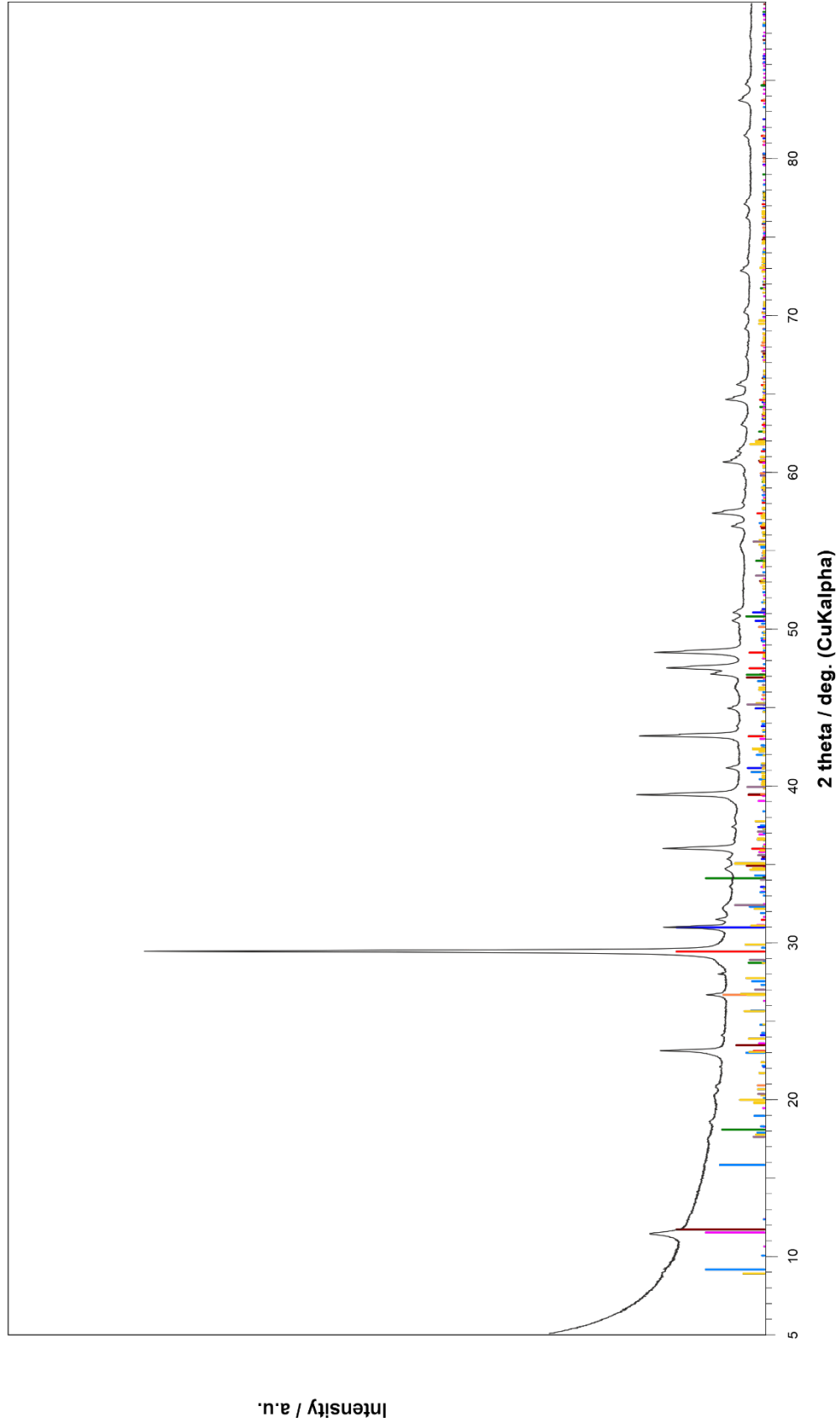


Fig. 99: XRD pattern of the 14A-C material

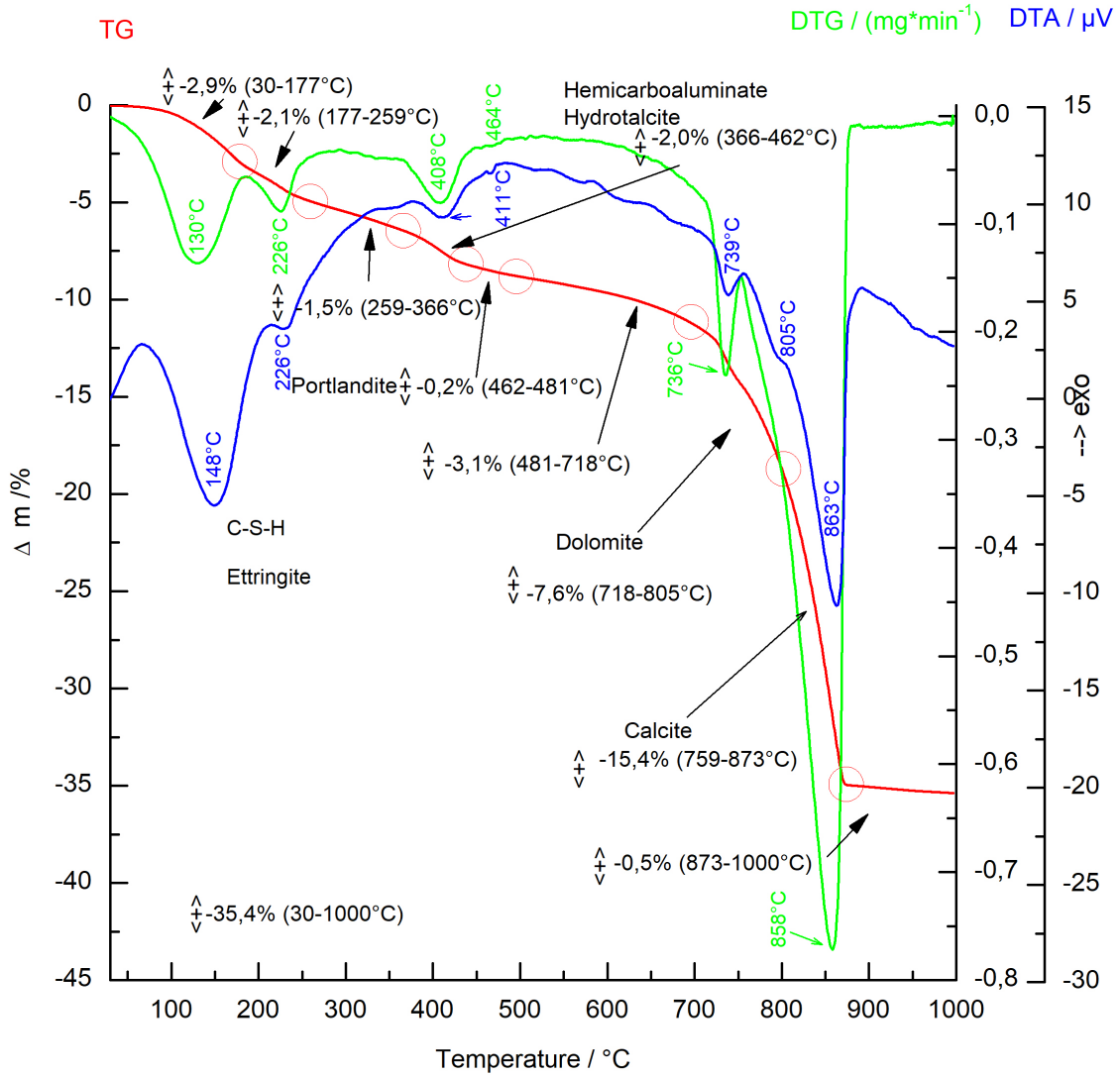


Fig. 100: TGA analysis of the 14B-A material

UV Vecernik CIM14B-A
 05-0586 (*) - Calcite, syn - CaCO3
 36-0426 (*) - Dolomite - CaMg(CO3)2
 44-1481 (*) - Portlandite, syn - Ca(OH)2
 04-018-9909 - Hemihydroaluminat (CH) - [Ca4Al2(OH)12(OH)0.4(CO3)0.8.4H2O]
 89-0460 (C) - Hydrocalcite, syn - (Mg0.667Al0.333)(OH)2(CO3)0.167(H2O)0.5
 46-1045 (*) - Quartz, syn - SiO2
 41-1451 (*) - Ettringite, syn - Ca6Al2(SO4)3(OH)12.26H2O
 76-0637 (C) - Muscovite 2 ITM 1 - KAl2(Si3Al)O10(OH)2
 38-0568 (I) - Kaolite, silification - Ca3Al2(SiO4)(OH)8

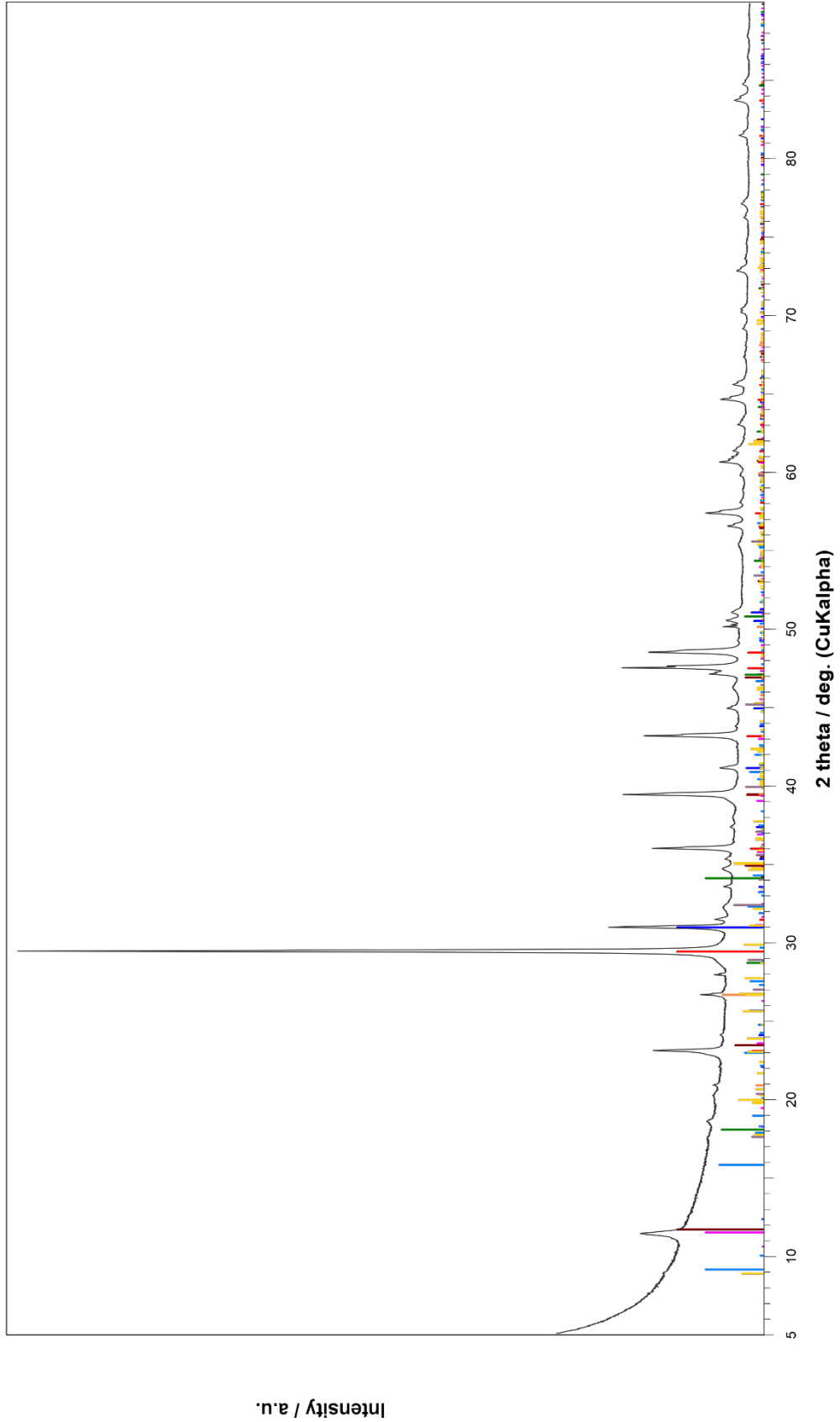


Fig. 101: XRD pattern of the 14B-A material

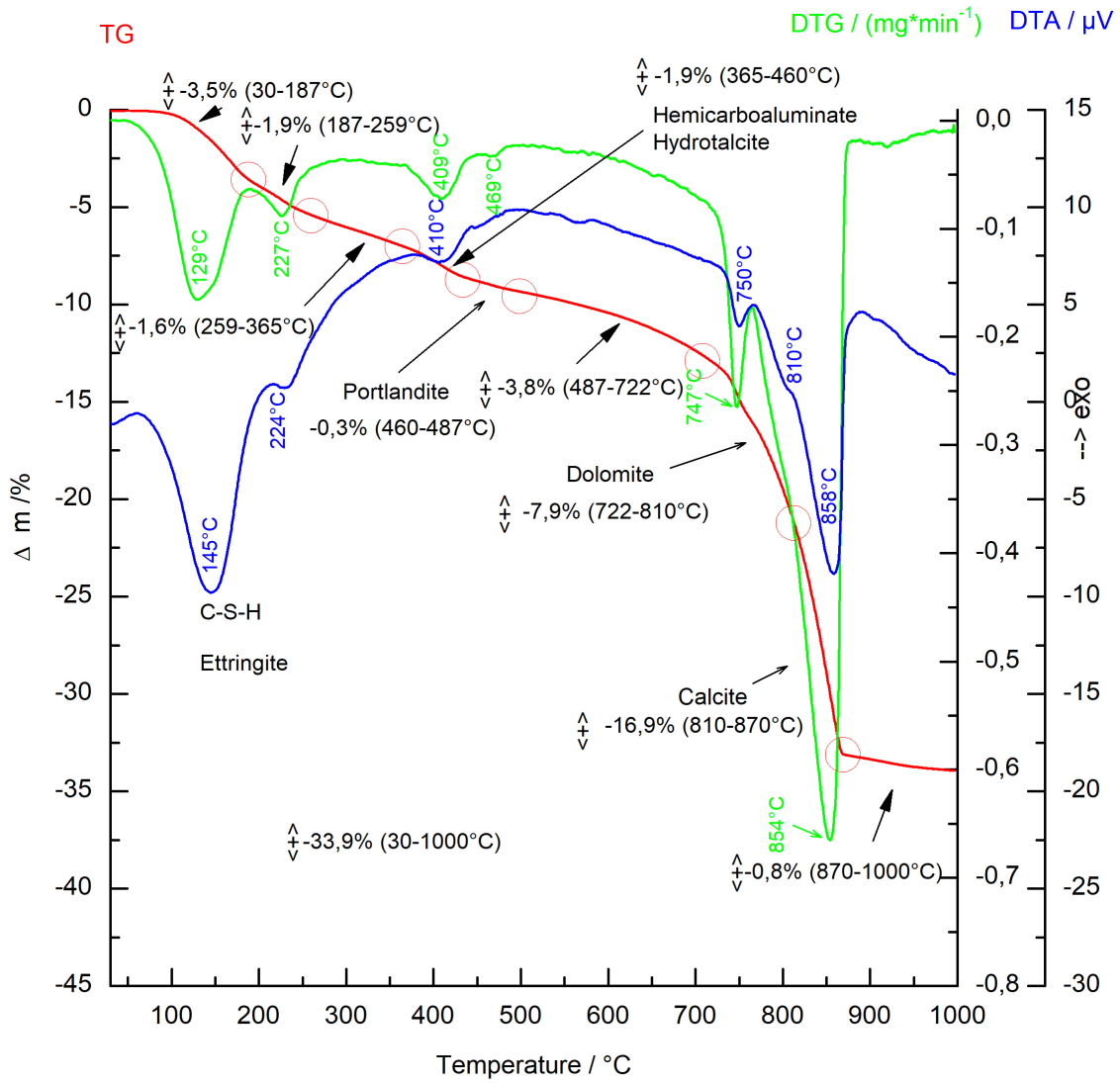


Fig. 102: TGA analysis of the 14B-C material

UV Vecernik CIM14B-C
 05-0586 (*) - Calcite, syn - CaCO3
 36-0426 (*) - Dolomite - CaMg(CO3)2
 44-1481 (*) - Portlandite, syn - Ca(OH)2
 04-018-9909 - Hemihydroaluminat (hhc) - [Ca4Al2(OH)12(OH)0.4(CO3)0.8.4H2O]
 89-0460 (C) - Hydrocalcite, syn - (Mg0.667Al0.333)(OH)2(CO3)0.167(H2O)0.5
 46-1045 (*) - Quartz, syn - SiO2
 41-1451 (*) - Ettringite, syn - Ca6Al2(SO4)3(OH)12.26H2O
 76-0637 (C) - Muscovite 2 ITM 1 - KAl2(Si3Al)O10(OH)2
 38-0568 (I) - Kaolite, silification - Ca3Al2(SiO4)(OH)8

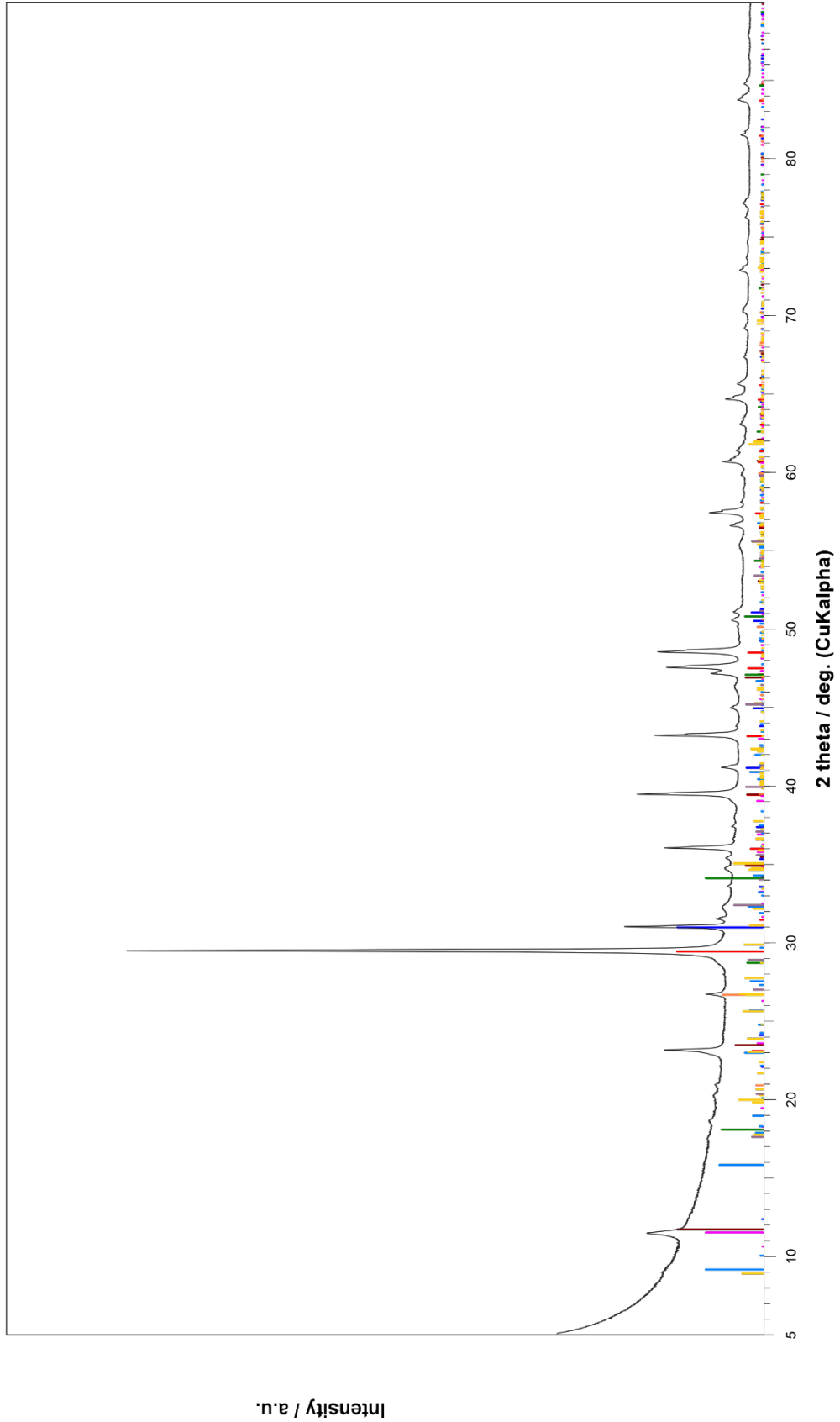


Fig. 103: XRD pattern of the 14B-C material

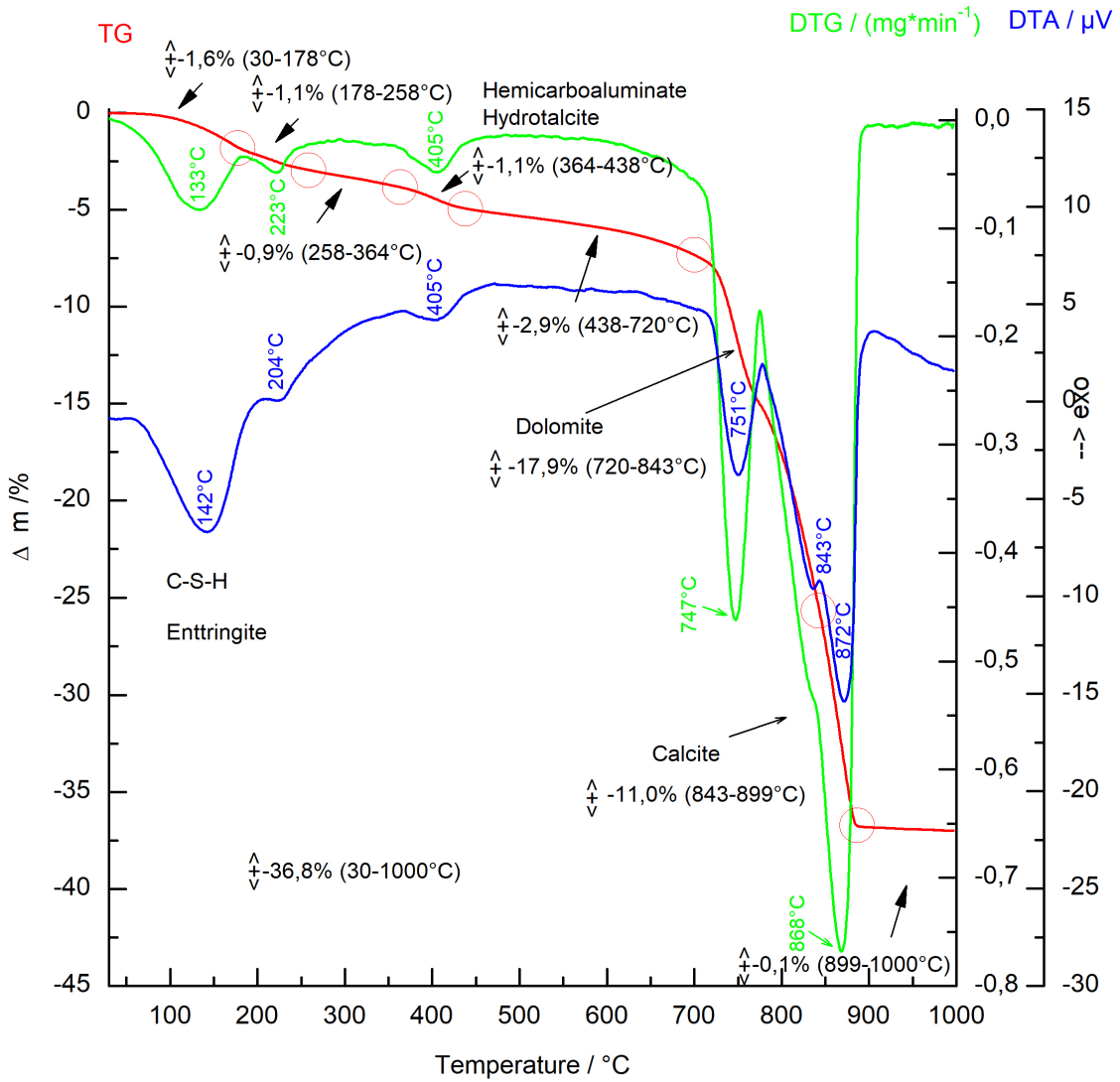


Fig. 104: TGA analysis of the 24A-A material

UV Vecernik CIM24A-A
 05-0586 (*) - Calcite, syn - CaCO3
 36-0426 (*) - Dolomite - CaMg(CO3)2
 44-1481 (*) - Portlandite, syn - Ca(OH)2
 04-018-9909 - Hemicarboaluminate (chc) - [Ca4Al2(OH)12(OH)0.4(CO3)0.8.4H2O]
 89-0460 (C) - Hydrocalcite, syn - (Mg0.667Al0.333)(OH)2(CO3)0.167(H2O)0.5
 46-1045 (*) - Quartz, syn - SiO2
 41-1451 (*) - Ettringite, syn - Ca6Al2(SO4)3(OH)12.26H2O
 76-0637 (C) - Muscovite 2 ITM 1 - KAl2(Si3Al)O10(OH)2
 38-0568 (I) - Kaolite, silification - Ca3Al2(SiO4)(OH)8

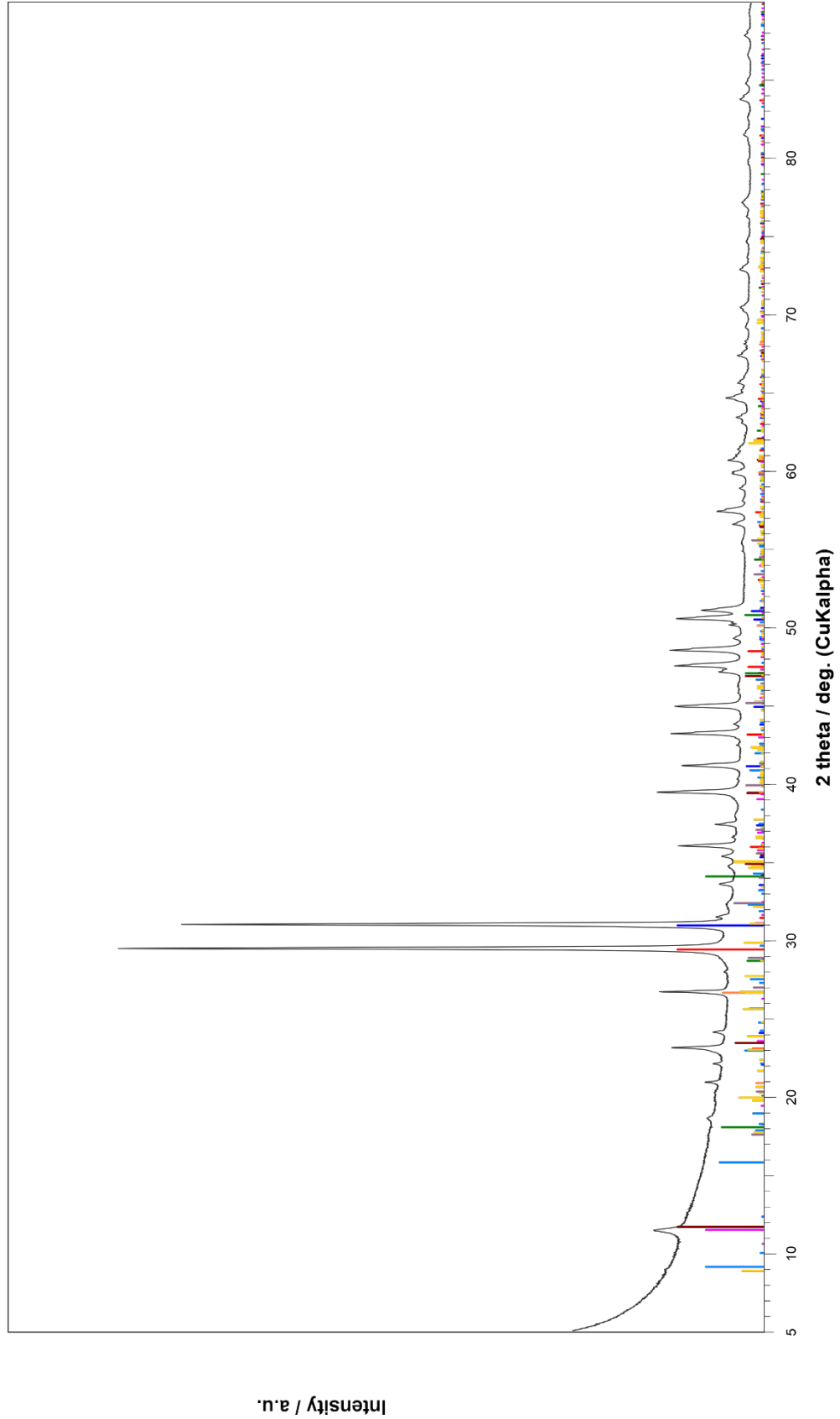


Fig. 105: XRD pattern of the 24A-A material

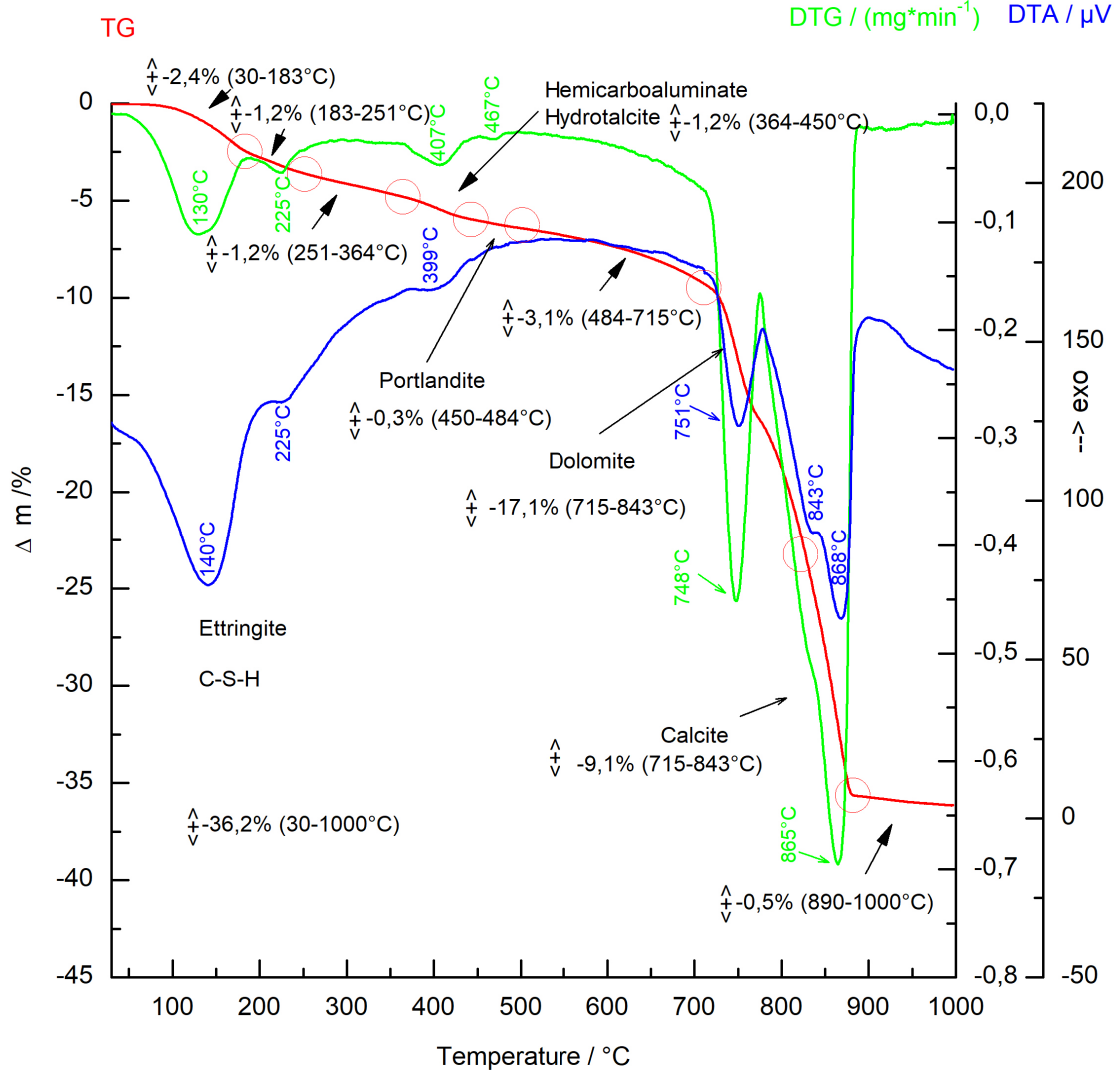


Fig. 106: TGA analysis of the 24A-C material

UV Vecernik CIM24A-C
 05-0586 (*) - Calcite, syn - CaCO₃
 36-0426 (*) - Dolomite - CaMg(CO₃)₂
 44-1481 (*) - Portlandite, syn - Ca(OH)₂
 04-018-9909 - Hemihydroaluminat (CH) - [Ca₄Al₂(OH)₁₂(OH)_{0.4}(CO₃)_{0.8}.4H₂O]
 89-0460 (C) - Hydrocalcite, syn - (Mg_{0.667}Al_{0.333})(OH)₂(CO₃)_{0.167}(H₂O)_{0.5}
 46-1045 (*) - Quartz, syn - SiO₂
 41-1451 (*) - Ettringite, syn - Ca₆A₂(SO₄)₃(OH)₁₂.26H₂O
 76-0637 (C) - Muscovite 2 ITM 1 - KAl₂(Si₃Al)O₁₀(OH)₂
 38-0568 (I) - Kaolite, silification - Ca₃A₂(SiO₄)(OH)₈

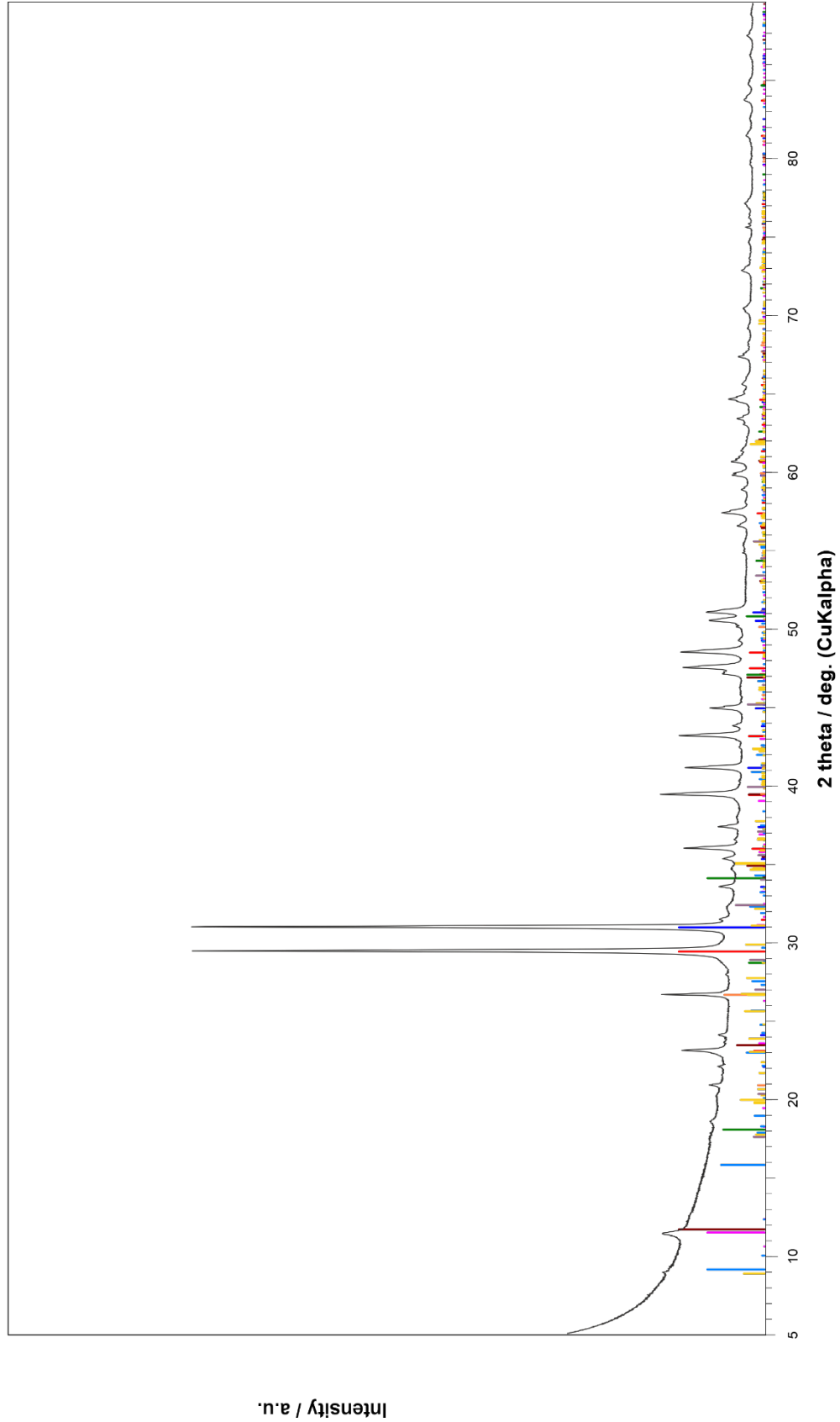


Fig. 107: XRD pattern of the 24A-C material

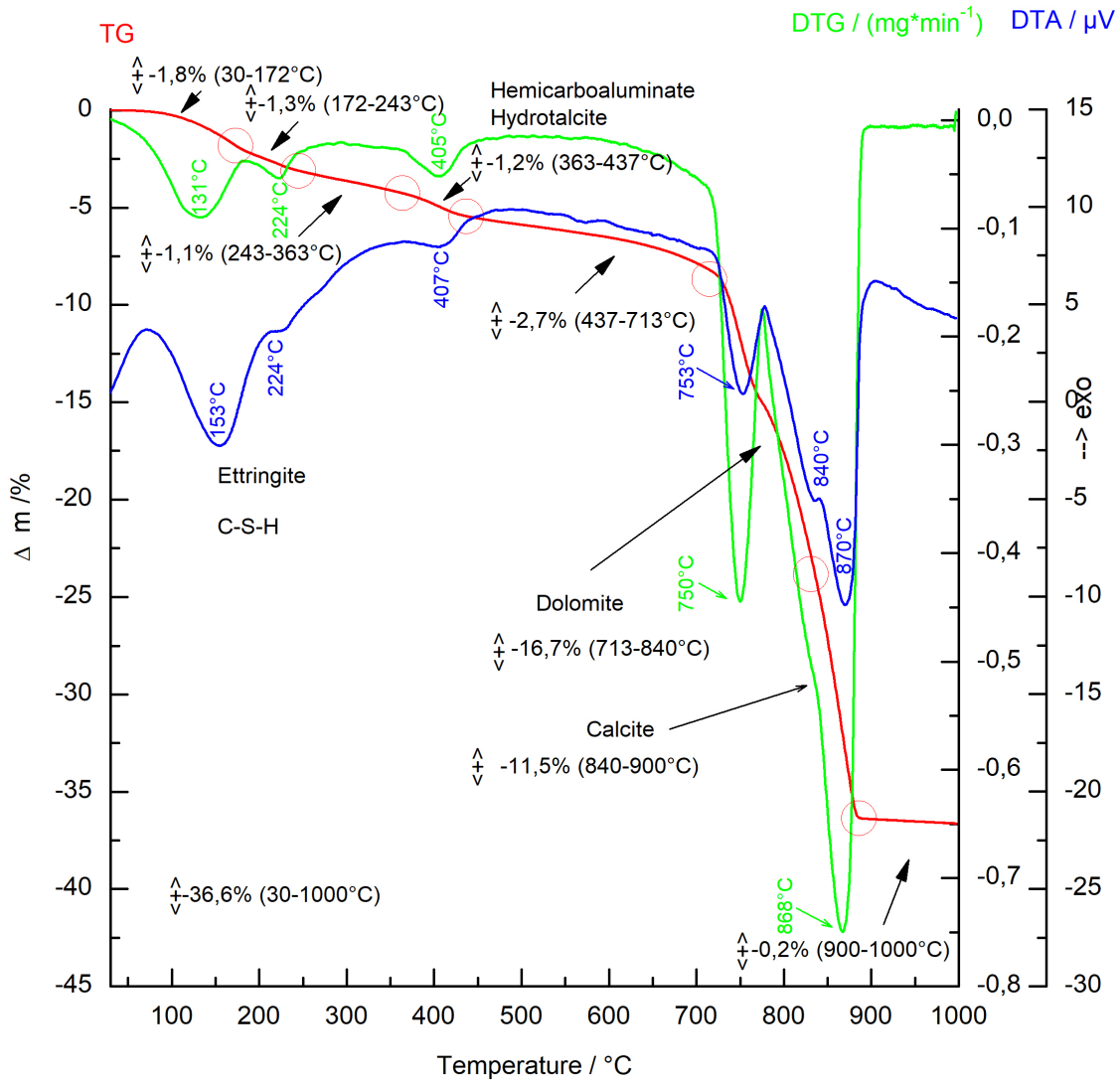


Fig. 108: TGA analysis of the 24B-A material

UV Vecernik CIM24B-A
 05-0586 (*) - Calcite, syn - CaCO3
 36-0426 (*) - Dolomite - CaMg(CO3)2
 44-1481 (*) - Portlandite, syn - Ca(OH)2
 04-018-9909 - Hemihydroaluminat (hhc) - [Ca4Al2(OH)12(OH)0.4(CO3)0.8.4H2O]
 89-0460 (C) - Hydrocalcite, syn - (Mg0.667Al0.333)(OH)2(CO3)0.167(H2O)0.5
 46-1045 (*) - Quartz, syn - SiO2
 41-1451 (*) - Ettringite, syn - Ca6Al2(SO4)3(OH)12.26H2O
 76-0637 (C) - Muscovite 2 ITM 1 - KAl2(Si3Al)O10(OH)2
 38-0568 (I) - Kaolite, silification - Ca3Al2(SiO4)(OH)8

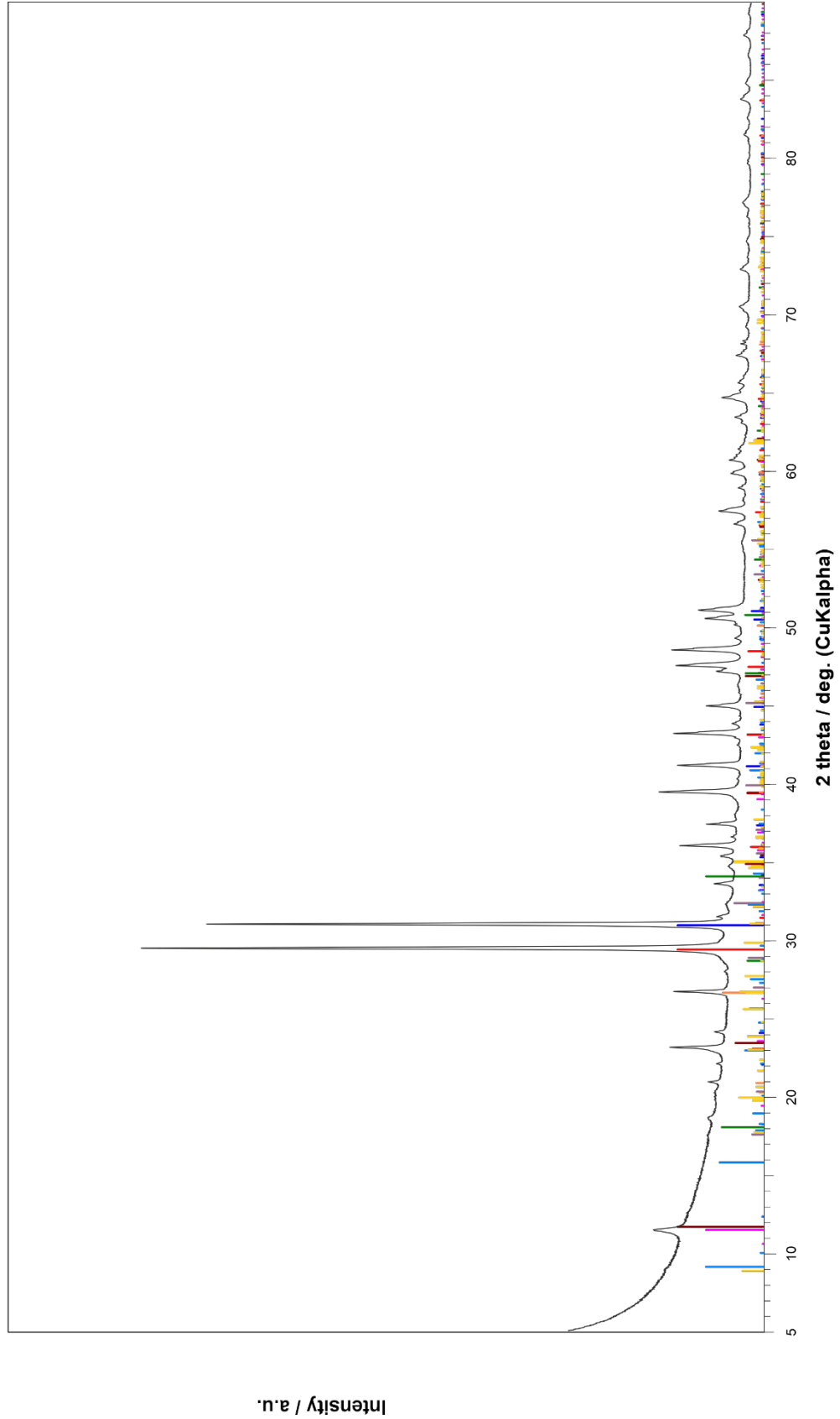


Fig. 109: XRD pattern of the 24A-A material

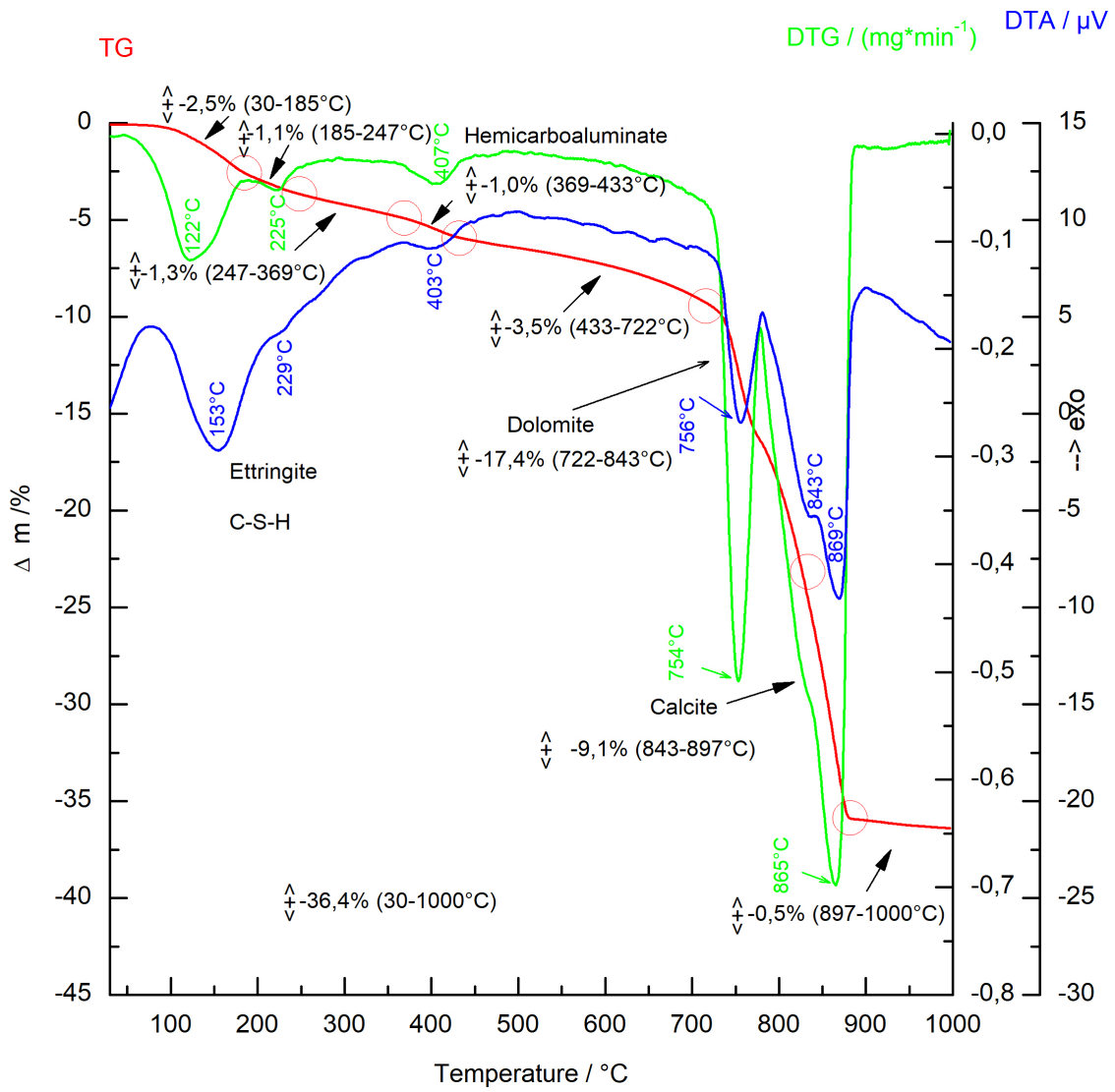


Fig. 110: TGA analysis of the 24B-C material

UV Vecernik CIM24B-C
 05-0586 (*) - Calcite, syn - CaCO3
 36-0426 (*) - Dolomite - CaMg(CO3)2
 44-1481 (*) - Portlandite, syn - Ca(OH)2
 04-018-9909 - Hemicarboaluminate (chc) - [Ca4Al2(OH)12(OH)0.4(CO3)0.8.4H2O]
 89-0460 (C) - Hydrocalcite, syn - (Mg0.667Al0.333)(OH)2(CO3)0.167(H2O)0.5
 46-1045 (*) - Quartz, syn - SiO2
 41-1451 (*) - Ettringite, syn - Ca6Al2(SO4)3(OH)12.26H2O
 76-0637 (C) - Muscovite 2 ITM 1 - KAl2(Si3Al)O10(OH)2
 38-0568 (I) - Kaolite, silification - Ca3Al2(SiO4)(OH)8

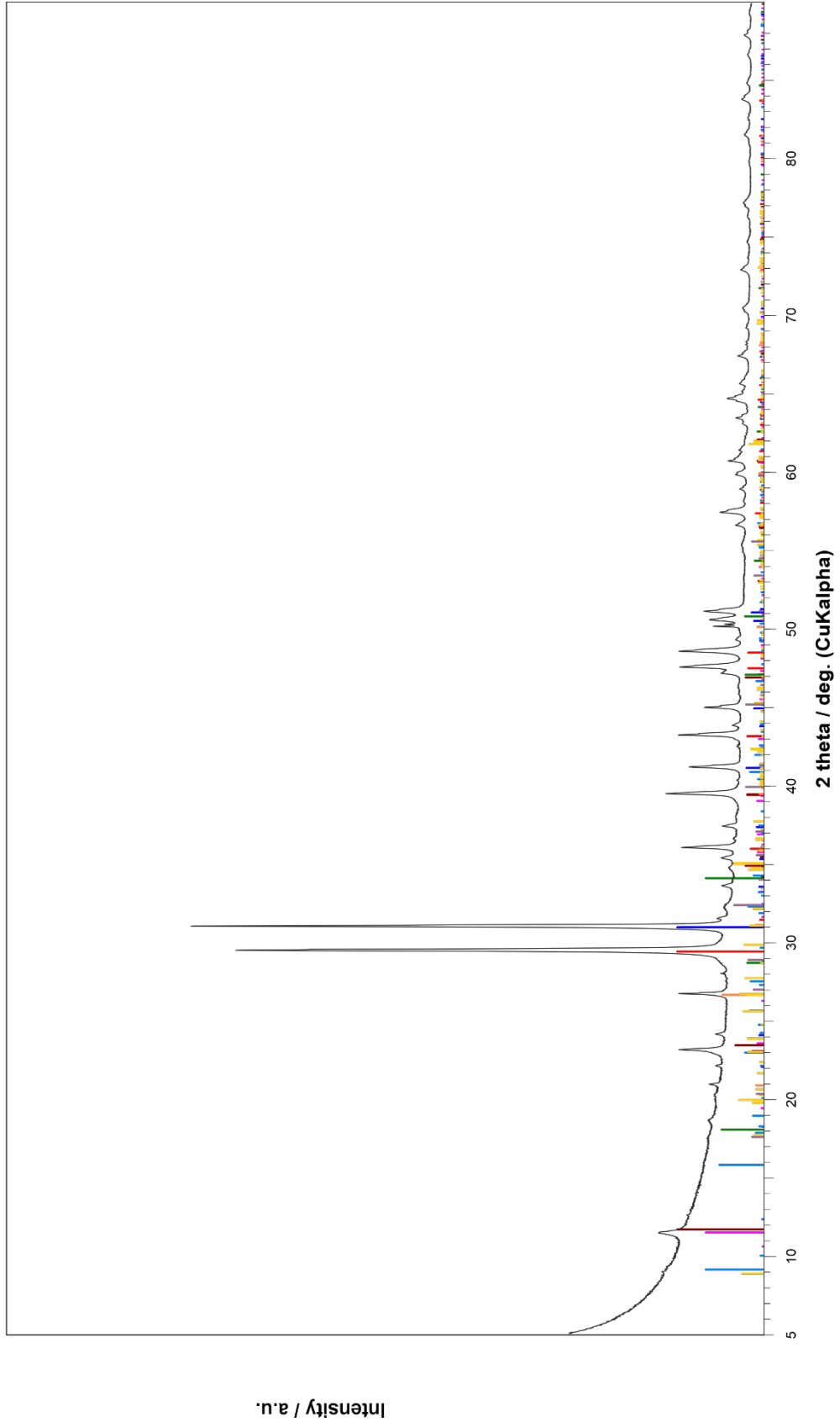


Fig. 111: XRD pattern of the 24B-C material

OUR SAFE FUTURE



SÚRAO

Radioactive Waste Repository Authority
Dlážděná 6, 110 00 Prague 1, Czech Republic
Tel.: +420 221 421 511, E-mail: info@surao.cz
www.surao.cz